Nonlinear Optical Characterisation for Chiral Nanophotonics

Joel T. Collins

A thesis submitted for the degree of Doctor of Philosophy

University of Bath
Department of Physics,
Centre for Photonics and Photonic Materials, and
Centre for Nanoscience and Nanotechnology

January 4, 2019

Abstract

Nonlinear optical processes provide a valuable technique for probing properties of chiral structures, i.e. those lacking mirror symmetry. Such structures are encountered frequently throughout organic chemistry, pharmacology, and biology, with a recent growing emphasis on sensitive characterisation of small quantities of chiral molecules.

It has been previously shown that chiroptical effects such as circular dichroism and optical rotation are significantly enhanced in second-harmonic generation. Additionally, plasmonic nanostructures can create local regions of high intensity chiral electromagnetic fields that can further enhance chiral-optical (chiroptical) interactions with molecules attached to the material surface.

In this thesis, chiroptical and nonlinear optical properties of effective dielectric media are reviewed in the context of both natural materials and plasmonic metamaterials. Using these principles, three novel chiral analysis schemes are demonstrated experimentally. Each experiment is designed for the characterisation of a unique plasmonic nanomaterial, all making use of enhanced nonlinear chiroptical effects.

First, plasmonic structures with dimensions comparable to the wavelength of incident light are studied. In these structures, electric field hotspots form, leading to small regions of enhanced chiral and nonlinear optical interactions. A theoretical description making use of a modal analysis and group theory is found to be a very good match to experimental results. Following this, the effects of anisotropy on nonlinear chiroptical measurements of a planar nanomaterial are examined. The structures are of sub-wavelength dimensions, however exhibit strong anisotropy that can contribute to chiroptical effects. It is found that specific experimental configurations can be exploited to separate the contributions from structural chirality and anisotropy, allowing pure chiral information to be obtained from highly anisotropic materials. Finally, anisotropic nanostructures are dispersed in liquid, allowing the study of orientationally-isotropic samples. In this case, nonlinear scattering is measured, and found to exhibit strong chiroptical effects. This is the first experimental report of circular intensity difference in second-harmonic scattering, and demonstrates significantly enhanced sensitivity when compared to widely used, linear characterisation techniques.

By designing new experimental schemes considering the unique challenges associated with each nanomaterial geometry, previously unobserved optical properties of the materials are revealed. Such tailored experimental methods pave the way for the further optimisation of chiral nanomaterials designed for applications in nanorobotics, photonic devices, and chemical sensing.

Contents

Acknowledgements

I would first like to thank Ventsislav Valev for his supervision, guidance, and motivation during the last three years. When I started this project our research group was just a few months old, and I am immensely proud of what we achieved in the following years. I have no doubt this is only the beginning. Of course, this would not have been possible without the work, support, and friendship of Christian Kuppe, David Hooper, and Kristina Rusimova; who made this group the best it could be, both professionally and personally. Additionally, I would like to thank all of those with whom I have had the privilege of collaborating during this time. In particular, I would like to thank Dimitar Slavov and Dave Carbery for their long-term academic support, interesting ideas, and invaluable friendship. I would also like to thank Peter Mosley and the rest of the CPPM for creating the best possible environment for new researchers from the day we all started.

Besides those involved directly in our work, I would of course like to thank my family. For both emotional support over the last 26 years, and for helping immensely during the authoring of this thesis. I cannot thank you enough. I'd like to specifically single out my Grandma Sandra for the inspirational advice: "If you feel yourself worrying, don't", my brother Dan for somehow knowing exactly how I was feeling, and what I needed, at all times, and of course my parents for their relentless support and tolerance over the years. Likewise, I would like to thank Charlotte Parry for her immense support since we met. You have stuck by me through my best laid plans and my worst of ideas, and never once stopped supporting me. For reminding me in hard times that "It doesn't really matter, does it?", "Just let it go, it's not worth it", and that we "Gotta go fast". You have made this time infinitely more fantastic than it would have otherwise been.

I would like to thank Philip Madgwick for making my time in Bath both immensely interesting, and fun, and reminding me that there's a big wide world outside of just physics. Finally, I would like to thank Sam Bell for standing by me as my permanent temporary secretary. You came along and stayed a spell, and I will be forever grateful.

Publications

J. T. Collins, K. R. Rusimova, D. C. Hooper, H.-H. Jeong, L. Ohnoutek, F. Pradaux-Caggiano, T. Verbiest, D. Carbery, P. Fischer, and V. K. Valev, "First observation of optical activity in hyper-Rayleigh scattering," *Phys. Rev. X*, 2019. Accepted

S. W. Lovesey, J. T. Collins, and S. P. Collins, "Superchiral photons unveil magnetic circular dichroism," *Phys. Rev. B*, 2018. Submitted

K. R. Rusimova, D. Slavov, F. Pradaux-Caggiano, D. Carbery, J. T. Collins, S. Gordeev, W. J. Wadsworth, P. J. Mosley, and V. K. Valev, "Atomic dispensers: thermoplasmonic control of alkali vapor pressure for quantum optical applications," *Nature Communications*, 2018. Submitted

J. T. Collins, D. C. Hooper, A. G. Mark, C. Kuppe, and V. K. Valev, "Second-Harmonic Generation Optical Rotation Solely Attributable to Chirality in Plasmonic Metasurfaces," *ACS Nano*, p. 8b00601, June 2018

C. Kuppe, C. Williams, J. You, J. T. Collins, S. N. Gordeev, T. D. Wilkinson, N.-C. Panoiu, and V. K. Valev, "Circular Dichroism in Higher-Order Diffraction Beams from Chiral Quasiplanar Nanostructures," *Advanced Optical Materials*, vol. 6, p. 1800098, June 2018

J. T. Collins, X. Zheng, N. V. S. Braz, E. Slenders, S. Zu, G. A. E. Vandenbosch, V. V. Moshchalkov, Z. Fang, M. Ameloot, P. A. Warburton, and V. K. Valev, "Enantiomorphing Chiral Plasmonic Nanostructures: A Counterintuitive Sign Reversal of the Nonlinear Circular Dichroism," *Advanced Optical Materials*, vol. 1800153, p. 1800153, May 2018

J. T. Collins, C. Kuppe, D. C. Hooper, C. Sibilia, M. Centini, and V. K. Valev, "Chirality and Chiroptical Effects in Metal Nanostructures: Fundamentals and Current Trends," *Advanced Optical Materials*, vol. 5, p. 1700182, Aug. 2017

D. C. Hooper, A. G. Mark, C. Kuppe, J. T. Collins, P. Fischer, and V. K. Valev, "Strong Rotational Anisotropies Affect Nonlinear Chiral Metamaterials," *Advanced Materials*, vol. 29, p. 1605110, Apr. 2017

Chapter 1

Structure and Overview

This thesis reports three new experimental schemes developed to provide nonlinear chiral-optical characterisation of plasmonic nanomaterial samples fabricated by our collaborators. The diversity of available nanostructure geometries has allowed us to develop new, tailored characterisation and analysis schemes. Previously unobserved novel optical behaviour is reported in each case.

Chapter 5 examines nanostructures with dimensions comparable to the wavelength of light, as the structure is "enantiomorphed" from one handedness to the other. Far-field nonlinear microscopy is used to probe the chiral properties of the nanostructures' local electromagnetic fields. Making use of group theory reveals the modal origin of strong experimentally observed near-field circular intensity difference.

A dramatically different nonlinear characterisation technique is presented in chapter 6. Second-harmonic generation optical rotation is used to probe a metamaterial consisting of sub-wavelength gold nanohelices. The individual structures are highly anisotropic, as well as chiral, and separating the effects of anisotropy and chirality is challenging. This chapter details the use of specific experimental configurations, and sample geometries, to disentangle the effects of anisotropy and true chirality.

Finally, chapter 7 discusses the first ever experimental observation of circular intensity difference in hyper-Rayleigh scattering, from an isotropic suspension of silver nanohelices. Measuring this effect is found to provide pure chiral information, free of significant contributions from structural anisotropy. In simple models of hyper-Rayleigh scattering from point-like scatterers, this chiroptical effect is symmetry-forbidden, and a physical origin is proposed by considering higher-order contributions based on existing models of molecular chirality.

Across all of these experiments, significant time has been spent developing Python libraries to simplify data acquisition and analysis within our research group. Chiral diffraction experiments undertaken by C. Kuppe (reference [5]) made use of an experiment-automation library I developed during this project, and eventually merged into a larger library, detailed in appendix E.1. Data analysis shown in chapters 6 and 7 made use of another Python library I developed to automate the filtering, processing, and plotting of data from our SHG optical activity setup. The library, detailed in appendix E.2, has since been used in submitted work by D. C. Hooper, and is expected to be used in similar

experiments going forward.

We will first begin in chapter 2 by discussing the general prevalence of chirality in nature, and the use of photonics as a platform for sensitive chiral characterisation techniques. Nonlinear optical effects in particular provide symmetry sensitivity that can be used to enhance chiral optical measurements, and are discussed in chapter 3. Specific to this work is the use of plasmonic nanomaterials to provide flexible, enhanced chiroptical *and* nonlinear optical interaction, and will be discussed in chapter 4.

Chapter 2

Chirality

Chirality has historically been defined as any shape whose mirror-image cannot be superimposed onto itself by only rotation, based on the 1894 definition by Lord Kelvin [9]. A more comprehensive definition accounting for both temporal and spatial symmetry was proposed in 1986 by Barron [10], stating that "true chirality is exhibited by systems that exist in two distinct enantiomeric states that are interconverted by space inversion, but not by time reversal combined with any proper spatial rotation." The word chiral derives from a Greek word for "the hand", an archetypal example of a chiral structure. A chiral pair of structures, "enantiomorphs", are often referred to as "left-handed" and "right-handed" because of this historical relationship to the hand. While chirality is very much present in nature on a macroscopic scale, from the structure of cyclones to the helicity of most gastropod shells, it is crucially exhibited by almost all biochemically and many pharmaceutically important molecules: the helical structure of DNA being a famous example of the importance of chirality in biology. Further, amino acids on earth are almost all exclusively "left-handed" chiral, while sugars are almost exclusively "right-handed" chiral. Importantly, while chiral molecules are energetically identical unless considering the weak interaction, their opposite enantiomorphs ("enantiomers" for molecules) can exhibit dramatically different effects on living organisms. A tragically famous example is the pharmaceutical drug Thalidomide. One enantiomer functions as an effective relief medication for morning-sickness, while the other can cause severe birth defects [11]. Any contamination of the wrong enantiomer can dramatically change the medical properties of the drug. Another example is methamphetamine (methylamphetamine). One enantiomer (*l*-methamphetamine) has been used as the, relatively benign, active ingredient in nasal decongestants in the United States [12]. Conversely, the other enantiomer (*d*-methamphetamine, commonly "crystal meth") "exerts potent physiological and psychostimulant effects and has high abuse liability" [13]. Similarly, ketamine is a racemic mixture of the enantiomers *d*-ketamine and *l*-ketamine, used for anaesthesia and pain relief, but commonly exhibiting hallucinogenic side effects [14]. Studies have established, however, that the analgesic effects are significantly more potent in one enantiomer, whereas the hallucinogenic side-effects are predominantly the result of the other enantiomer [14, 15, 16]. Obtaining either enantiomer over the other has clear advantages over the production and use of racemic mixtures. Typically enantioseparation is performed in-situ, and involves

the selective removal of one enantiomer from the racemic mixture until an acceptable ratio is achieved [17]. There is thus a prevailing need for robust characterisation techniques of chiral systems within the pharmaceutical industry and biochemical research. Beyond biomolecular systems, man-made chiral structures (discussed further in section 4) can be fabricated for applications in photonic devices [18, 19, 20], nanorobotics [21, 22], and in particular chemical sensing platforms. Common between these applications, biochemical research, and pharmaceutical manufacturing, is the need for comprehensive experimental characterisation of chiral systems. Generally, chiral information can be obtained from any interaction between the chiral structure with unknown properties, and a well understood chiral system responsible for sensing. Enantioselective processes can occur, for example, from interactions between two chiral molecules, or more relevant to this work, interactions between chiral structures and light. We can describe the interaction between light and a general chiral material by considering the polarisation properties of a propagating monochromatic plane wave through a chiral medium.

The general mathematical form of a coherent monochromatic plane wave at a distance z and time t, oscillating at a frequency ω, is given by equation 2.1 [23, §8.1.1]. The wave is polarised in the $x-y$ plane, and propagates along the z axis with a wavevector k_z. ϕ describes the relative phase shift between the orthogonal components of polarisation, oscillating in the $\hat{\mathbf{x}}$ and $\hat{\mathbf{y}}$ directions with amplitudes E_x and E_y respectively.

$$\mathbf{E} = E_x\hat{\mathbf{x}}\cos(k_z z - \omega t) - E_y\hat{\mathbf{y}}\cos(k_z z - \omega t + \phi) \tag{2.1}$$

Linear combinations of E_x and E_y, as in equation 2.1, with no phase shift ($\phi = 0$) result in linearly polarised light, with a polarisation axis depending on the relative amplitudes of E_x and E_y. Crucially, linear combinations of E_x and E_y with non-zero amplitudes and a non-zero phase shift ϕ will result in a chiral polarisation state: the polarisation vector rotates about the axis of propagation, tracing a helical profile. The ellipticity of this wave depends on both the phase and amplitude of the orthogonal linear components E_x and E_y. Circular polarisation is the special case of a $\pm\pi/2$ phase shift between E_x and E_y of equal amplitude. The sign of the phase shift determines the direction of the polarisation rotation, resulting in left- and right-circularly polarised light (CPL). In this work, right-circularly polarised (RCP) light is defined as a clockwise rotation of the polarisation vector *from the point of view of the wave source*. Conversely, left-circularly polarised (LCP) light is defined as a counter-clockwise rotation of the polarisation vector in the same frame. The wave equations for left- and right-circularly polarised light in this convention are given by equation 2.2 [23, §8.1.2]).

$$\begin{aligned}\mathbf{E}_{RCP} &= E_0\left[\hat{\mathbf{x}}\cos(k_z z - \omega t) + \hat{\mathbf{y}}\sin(k_z z - \omega t)\right] \\ \mathbf{E}_{LCP} &= E_0\left[\hat{\mathbf{x}}\cos(k_z z - \omega t) - \hat{\mathbf{y}}\sin(k_z z - \omega t)\right]\end{aligned} \tag{2.2}$$

Since left- and right-circular polarisation states are orthogonal, any arbitrary polarisation can also be represented by the linear combination of LCP and RCP waves. For example, linear polarisation can be represented as the linear combination of equal amplitude LCP

and RCP waves $\mathbf{E}_{LCP}$ and $\mathbf{E}_{RCP}$ [24, §3.3].

Outside of the special cases of CPL and linearly polarised light, polarisation is described as elliptical, since both the total field amplitude, and the direction of polarisation, can vary as the wave propagates, resulting in an elliptical profile. The orientation of the elliptical profile, the ellipticity of the profile, and the direction of polarisation rotation, all depend on both the amplitudes of E_x and E_y, and the phase between them. Experimentally, elliptical and circular polarisations of light are realised by making use of an anisotropic, birefringent medium: one which has different refractive indices in orthogonal axes. Anisotropy in the real part of refractive index means that components of light polarised along the orthogonal axes, known as the medium's fast and slow axes, propagate with different phase velocities and accumulate a relative phase shift during propagation [25, §2.4]. By designing the thickness of the material such that the accumulated phase shift is $2m\pi \pm \pi/2$ at the operating wavelength λ (where m is some integer), elliptically and circularly polarised light can be obtained. Such a device is known as a quarter-wave plate (QWP), as it induces a shift of $\lambda/4$ between orthogonal polarisation components [23, §8.7.1]. The orientation of the ellipses major axis depends on the direction of the incident polarisation, and the ellipticity depends on the angle of the material's fast axis relative to the direction of incident polarisation (figure 2.1). Similarly, the orientation of linear polarisation can be rotated (known as "optical rotation", OR) by making use of a half-wave plate (HWP), which induces a relative phase shift of $2m\pi \pm \pi$ between orthogonal polarisation components. The angle of optical rotation also depends on the angle of the material's fast axis relative to the direction of incident polarisation.

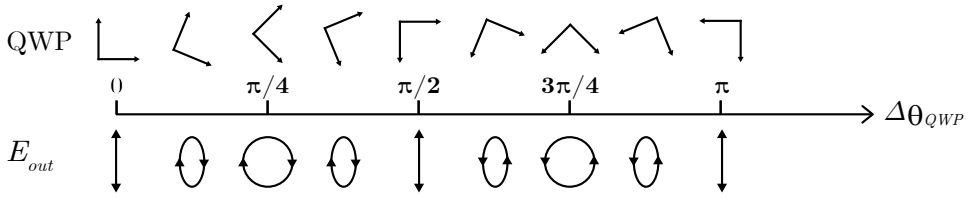

Figure 2.1: *Output polarisation from a QWP at an angle $\Delta\theta_{QWP}$ to the input polarisation. The angle of the incident polarisation (and subsequent elliptical and linear outputs) can be controlled by a half-wave plate.*

Whereas linear birefringence results from structural anisotropy, a medium with structural *chirality*, such as a chiral molecular system, can exhibit a similar dissymmetry in its interaction with LCP and RCP light. This leads to chiral-optical (chiroptical) effects, directly beneficial for both polarisation optics, and the characterisation of unknown chiral structures. The rest of this chapter discusses the physical origin of chiroptical effects relevant to this work, and the parameters used to characterise the interactions between chiral structures and light.

2.1 Structural Chirality

In the simple case of a linear, isotropic medium, the macroscopic electromagnetic response of the material is described by the constitutive relations given in equation 2.3. These

relate the material's internal electric displacement field $\tilde{\mathbf{D}}$ and magnetic field strength $\tilde{\mathbf{H}}$ to external electric and magnetic fields $\tilde{\mathbf{E}}$ and $\tilde{\mathbf{B}}$, where tildes denote complex values. Here, ε and μ are complex scalars and correspond to the isotropic electric permittivity and magnetic permeability of the material.

$$\begin{aligned} \tilde{\mathbf{D}} &= \tilde{\varepsilon}\tilde{\mathbf{E}} \\ \tilde{\mathbf{B}} &= \tilde{\mu}\tilde{\mathbf{H}} \end{aligned} \tag{2.3}$$

In the general case however, we cannot assume isotropy. Furthermore, $\tilde{\mathbf{D}}$ and $\tilde{\mathbf{H}}$ may depend on both $\tilde{\mathbf{E}}$ and $\tilde{\mathbf{B}}$ (magnetoelectric coupling). For a bi-anisotropic medium (anisotropic, with no-zero magnetoelectric coupling), the constitutive relations take the form of equation 2.4.[26, 27]. Here, $\tilde{\varepsilon}$, $\tilde{\mu}$, $\tilde{\xi}$, and $\tilde{\zeta}$ are 3×3 matrices due to the anisotropy of the material. $\tilde{\xi}$, and $\tilde{\zeta}$ are pseudo-scalars (behaving as scalars, but changing sign under parity inversion), and describe the magnetoelectric coupling.

$$\begin{bmatrix} \tilde{\mathbf{D}} \\ \tilde{\mathbf{B}} \end{bmatrix} = \begin{bmatrix} \tilde{\varepsilon} & \tilde{\xi} \\ \tilde{\zeta} & \tilde{\mu} \end{bmatrix} \begin{bmatrix} \tilde{\mathbf{E}} \\ \tilde{\mathbf{H}} \end{bmatrix} \tag{2.4}$$

In the case of a non-gyrotropic material (exhibiting no magneto-optic rotation), equation 2.4 has additional constraints, due to time-reversal symmetry, given in equation 2.5 [26].

$$\begin{aligned} [\tilde{\xi}]^{\mathbf{t}} &= -[\tilde{\zeta}] \\ [\tilde{\varepsilon}]^{\mathbf{t}} &= [\tilde{\varepsilon}] \\ [\tilde{\mu}]^{\mathbf{t}} &= [\tilde{\mu}] \end{aligned} \tag{2.5}$$

The expressions shown in equation 2.3 are a special case of equation 2.4, where no magnetoelectric cross-coupling is present, so $\tilde{\xi} = \tilde{\zeta} = \mathbf{0}$, and due to isotropy $\tilde{\varepsilon}$ and $\tilde{\mu}$ become scalars. In the case of a non-chiral anisotropic material, $\tilde{\xi} = \tilde{\zeta} = \mathbf{0}$ however $\tilde{\varepsilon}$ and $\tilde{\mu}$ remain as matrices. Most relevant in this discussion however is the special case of a homogeneous bi-isotropic (isotropic chiral) medium. In this case the matrix components reduce to scalars, but all four components remain. The constraints given in equation 2.5 apply, and so we find that $\xi = -\zeta$.

There are several ways to write the remaining relations, including Post's relations [27], Born's relations [28, 29] , and Tellegen's relations [27, 30, 31] (equation 2.6). Tellegen's relations will be used here, however the various forms are equivalent.

$$\begin{bmatrix} \tilde{\mathbf{D}} \\ \tilde{\mathbf{B}} \end{bmatrix} = \begin{bmatrix} \varepsilon_0\tilde{\varepsilon}_r & i\tilde{\kappa}\sqrt{\mu_0\varepsilon_0} \\ -i\tilde{\kappa}\sqrt{\mu_0\varepsilon_0} & \mu_0\tilde{\mu}_r \end{bmatrix} \begin{bmatrix} \tilde{\mathbf{E}} \\ \tilde{\mathbf{H}} \end{bmatrix}. \tag{2.6}$$

Here, $\tilde{\varepsilon}_r$ and $\tilde{\mu}_r$ are the relative permittivity and permeability of the material respectively, and $\tilde{\kappa}$ is known as the structural "chirality parameter". In order to describe electromagnetic wave propagation through the chiral medium, we start by making use of the source-free time-harmonic Maxwell's equations in SI units convention. For a field oscillating at a

frequency ω, these take the form:

$$\nabla \cdot \tilde{\mathbf{D}} = \nabla \cdot \tilde{\mathbf{E}} = 0 \tag{2.7}$$

$$\nabla \cdot \tilde{\mathbf{B}} = \nabla \cdot \tilde{\mathbf{H}} = 0 \tag{2.8}$$

$$\nabla \times \tilde{\mathbf{E}} = \frac{\partial \tilde{\mathbf{B}}}{\partial t} = i\omega \tilde{\mathbf{B}} \tag{2.9}$$

$$\nabla \times \tilde{\mathbf{H}} = -\frac{\partial \tilde{\mathbf{D}}}{\partial t} = -i\omega \tilde{\mathbf{D}}. \tag{2.10}$$

For simplicity, equation 2.6 can be rewritten in terms of $\varepsilon = \varepsilon_0 \tilde{\varepsilon_r}$, $\mu = \mu_0 \tilde{\mu_r}$, and $\gamma = \tilde{\kappa}\sqrt{\mu_0 \varepsilon_0}$ to give

$$\tilde{\mathbf{D}} = \varepsilon \tilde{\mathbf{E}} + i\gamma \tilde{\mathbf{H}} \tag{2.11}$$

$$\tilde{\mathbf{H}} = \frac{1}{\mu}(\tilde{\mathbf{B}} + i\gamma \tilde{\mathbf{E}}). \tag{2.12}$$

Inserting equation 2.9 into equation 2.12 gives an expression for $\tilde{\mathbf{H}}$ eliminating all fields other than $\tilde{\mathbf{E}}$:

$$\tilde{\mathbf{H}} = \frac{1}{\mu}\left(\frac{1}{i\omega}\nabla \times \tilde{\mathbf{E}} + i\gamma \tilde{\mathbf{E}}\right). \tag{2.13}$$

Then, by equating expressions for $\tilde{\mathbf{D}}$ from equations 2.10 and 2.11 we obtain

$$\frac{i}{\omega}\nabla \times \tilde{\mathbf{H}} = \varepsilon \tilde{\mathbf{E}} + i\gamma \tilde{\mathbf{H}}. \tag{2.14}$$

Substituting equation 2.13 into equation 2.14 gives

$$\frac{i}{\omega\mu}\nabla \times \left(\frac{1}{i\omega}\nabla \times \tilde{\mathbf{E}} + i\gamma \tilde{\mathbf{E}}\right) = \varepsilon \tilde{\mathbf{E}} + i\frac{\gamma}{\mu}\left(\frac{1}{i\omega}\nabla \times \tilde{\mathbf{E}} + i\gamma \tilde{\mathbf{E}}\right). \tag{2.15}$$

For a *homogeneous* isotropic chiral medium this can be simplified to obtain the following differential equation for the electric field:

$$\nabla \times (\nabla \times \tilde{\mathbf{E}}) - (\varepsilon\mu - \gamma^2)\omega^2 \tilde{\mathbf{E}} - 2\omega\gamma \nabla \times \tilde{\mathbf{E}} = 0. \tag{2.16}$$

By making use of the vector identity $\nabla \times (\nabla \times \tilde{\mathbf{E}}) = \nabla(\nabla \cdot \tilde{\mathbf{E}}) - \nabla^2 \tilde{\mathbf{E}}$ and equation 2.7, this is further simplified to give

$$\nabla^2 \tilde{\mathbf{E}} + (\varepsilon\mu - \gamma^2)\omega^2 \tilde{\mathbf{E}} + 2\omega\gamma \nabla \times \tilde{\mathbf{E}} = 0. \tag{2.17}$$

Due to isotropy and homogeneity we can, without loss of generality, assume a monochromatic plane-wave solution propagating in the z direction with a wavevector k of the form

$$\tilde{\mathbf{E}} = \begin{bmatrix} \tilde{E}_x \\ \tilde{E}_y \\ \tilde{E}_z \end{bmatrix} e^{ikz} \tag{2.18}$$

where $\tilde{E}_x$, $\tilde{E}_y$, and $\tilde{E}_z$ are the complex scalar amplitudes of x, y, and z components of

the oscillating electric field respectively. The problem can be further simplified by noting that $\nabla \cdot \tilde{\mathbf{E}} = 0$ (equation 2.7), and therefore $\tilde{E}_z = 0$. Inserting the plane-wave solution into equation 2.17, and leaving in vector notation, gives:

$$\nabla^2 \begin{bmatrix} \tilde{E}_x e^{ikz} \\ \tilde{E}_y e^{ikz} \\ 0 \end{bmatrix} + (\varepsilon\mu - \gamma^2)\omega^2 \begin{bmatrix} \tilde{E}_x e^{ikz} \\ \tilde{E}_y e^{ikz} \\ 0 \end{bmatrix} + 2\omega\gamma\nabla \times \begin{bmatrix} \tilde{E}_x e^{ikz} \\ \tilde{E}_y e^{ikz} \\ 0 \end{bmatrix} = 0. \tag{2.19}$$

Expanding the del operator terms using

$$\nabla^2 \begin{bmatrix} \tilde{E}_x e^{ikz} \\ \tilde{E}_y e^{ikz} \\ 0 \end{bmatrix} = \begin{bmatrix} \tilde{E}_x \\ \tilde{E}_y \\ 0 \end{bmatrix} (-k^2 e^{ikz}), \qquad \nabla \times \begin{bmatrix} \tilde{E}_x e^{ikz} \\ \tilde{E}_y e^{ikz} \\ 0 \end{bmatrix} = \begin{bmatrix} -\tilde{E}_y \\ \tilde{E}_x \\ 0 \end{bmatrix} (ike^{ikz}) \tag{2.20}$$

reduces equation 2.19 to

$$-k^2 \begin{bmatrix} \tilde{E}_x \\ \tilde{E}_y \end{bmatrix} e^{ikz} + (\varepsilon\mu - \gamma^2)\omega^2 \begin{bmatrix} \tilde{E}_x \\ \tilde{E}_y \end{bmatrix} e^{ikz} + 2i\omega k\gamma \begin{bmatrix} \tilde{E}_x \\ -\tilde{E}_y \end{bmatrix} e^{ikz} = 0. \tag{2.21}$$

Equation 2.21 can then be recast as an eigenproblem of the form $\underline{M}\mathbf{E} = 0$, specifically:

$$\begin{bmatrix} (\varepsilon\mu - \gamma^2)\omega^2 - k^2 & -2i\omega k\gamma \\ 2i\omega k\gamma & (\varepsilon\mu - \gamma^2)\omega^2 - k^2 \end{bmatrix} \begin{bmatrix} \tilde{E}_x \\ \tilde{E}_y \end{bmatrix} = 0. \tag{2.22}$$

This problem has nontrivial solutions only if

$$\det(\underline{M}) = \begin{vmatrix} (\varepsilon\mu - \gamma^2)\omega^2 - k^2 & -2i\omega k\gamma \\ 2i\omega k\gamma & (\varepsilon\mu - \gamma^2)\omega^2 - k^2 \end{vmatrix} = 0. \tag{2.23}$$

Finding the determinant of $\underline{M}$ gives

$$\det(\underline{M}) = \omega^4(\gamma^2 - \varepsilon\mu)^2 - 2k^2\omega^2(\gamma^2 + \varepsilon\mu) + k^4 = 0. \tag{2.24}$$

Solutions to this expression then directly yield the dispersion relations for light propagating through the medium:

$$k_\pm = \omega(\sqrt{\varepsilon\mu} \pm \gamma). \tag{2.25}$$

In terms of the chirality parameter κ, these can be rewritten as

$$k_\pm = k_0 \left(\sqrt{\tilde{\mu}_r \tilde{\varepsilon}_r} \pm \tilde{\kappa} \right) \tag{2.26}$$

where $k_0 = \omega/c_0$ is the wave number in vacuum (and $c_0 = 1/\sqrt{\mu_0\varepsilon_0}$ is the speed of light in vacuum). The associated eigenwaves $\tilde{\mathbf{E}}_+$ and $\tilde{\mathbf{E}}_-$ are given by

$$\tilde{\mathbf{E}}_\pm = \begin{bmatrix} \tilde{E}_x \\ \pm i\tilde{E}_y \end{bmatrix} e^{ikz} \tag{2.27}$$

and correspond to right (+) and left (−) circularly polarised light respectively [28, §2.2][32]. The refractive indices of the medium for propagating RCP and LCP light are therefore given by equation 2.28 [27, 33, 34].

$$\tilde{n}_{\pm} = \sqrt{\tilde{\mu}_r \tilde{\varepsilon}_r} \pm \tilde{\kappa} \tag{2.28}$$

Larger values of $\tilde{\kappa}$ lead to larger chiral dissymmetry: the difference in the optical response of a material to left- and right-circularly polarised light. Additionally, for a sufficiently large value of $\tilde{\kappa}$, negative refractive index can be achieved for one direction of CPL [35].

2.2 Chiroptical Effects

Any material with a non-zero chirality parameter κ will necessarily exhibit chiroptical effects dependent on its real and imaginary parts. As in section 2.1, the real part of the refractive index of a medium n describes the phase velocity of light propagating through the medium, and the imaginary part describes the absorption of light by the medium. From equation 2.26, $\mathrm{Im}(\kappa)$ thus describes the differential *absorption* of LCP and RCP light, known as circular dichroism (CD). In linear optics, the circular dichroism at a particular

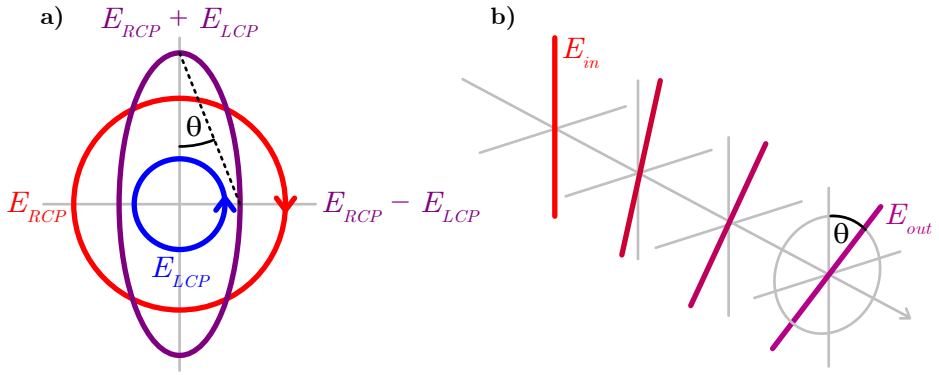

Figure 2.2: ***a)*** *Schematic diagram of circular dichroism, characterised by the ellipticity ellipticity θ defined in terms of the field amplitudes of RCP and LCP light E_{RCP} and E_{LCP}. The ellipticity is given by equation 2.29.* ***b)*** *Schematic diagram of optical rotation, showing linearly polarised light rotated by an angle θ throughout propagation through an optically active medium.*

wavelength of light λ is quantified by the ellipticity $\theta(\lambda)$, as defined by equation 2.29, and shown schematically in figure 2.2a [24, §9.2].

$$\theta(\lambda) = \arctan\left(\frac{E_{RCP}(\lambda) - E_{LCP}(\lambda)}{E_{RCP}(\lambda) + E_{LCP}(\lambda)}\right) \tag{2.29}$$

Here, E_{RCP} and E_{LCP} are the amplitudes of RCP and LCP light *after* interaction with the chiral material. If $\mathrm{Im}(\kappa) = 0$, light can still be absorbed by the medium, but due to mirror symmetry, RCP and LCP light will be absorbed equally, and the CD as defined in equation 2.29 is zero. For a non-zero $\mathrm{Im}(\kappa)$, E_{RCP} and E_{RCP} depend on both the magnitude of $\mathrm{Im}(\kappa)$, and the propagation length through the absorbing medium. If the propagation length is known, then circular dichroism can be used as a probe for the chirality parameter κ. Correspondingly, $\mathrm{Re}(\kappa)$ describes the differential *phase velocity* for

LCP and RCP light. Since linearly polarised light can be represented by a superposition of equal-amplitude LCP and RCP waves, a linearly polarised wave, of vacuum wavevector k_z propagating through a medium with RCP and LCP refractive indices given by n_+ and n_- respectively, is described by equation 2.30 [23, §8.10].

$$\mathbf{E} = E_0 \cos(k_z(\frac{n_+ + n_-}{2})z - \omega t) \left[\hat{\mathbf{x}} \cos(k_z(\frac{n_+ - n_-}{2})z) + \hat{\mathbf{y}} \sin(k_z(\frac{n_+ - n_-}{2})z)\right] \tag{2.30}$$

At any point in time throughout propagation, the RCP and LCP components are oscillating in phase and with equal amplitudes, meaning that the resultant wave remains linearly polarised. However, the orientation of the linear polarisation will rotate throughout propagation, with the rate and direction of rotation depending on the magnitude and sign of $n_+ - n_-$ respectively. This effect is the chiral counterpart to birefringence, where orthogonal *linear* polarisations exhibit different phase velocities. It is thus known as "circular birefringence". In the case of linear birefringence, optical rotation is achieved by utilising a fixed $\lambda/2$ phase shift, and rotating the mediums fast axis relative to the incident polarisation to control the angle of rotation [36, A3.10]. Conversely, a material exhibiting circular birefringence will rotate linearly polarised light continuously during propagation, shown schematically in figure 2.2b. Therefore, the resulting angle of optical rotation (θ in figure 2.2b) depends on both the strength of circular birefringence, and the propagation length through the medium. Optical rotation can therefore also be used as a method to characterise the chirality parameter κ of the material. Collectively, circular dichroism and optical rotation are referred to as "optical activity" [23, §8.10].

Generally, in real materials the refractive index n is strongly wavelength-dependent. The refractive index $n(\lambda)$ includes contributions from the wavelength-dependent structural chirality parameter $\kappa(\lambda)$. The dependence of $n(\lambda)$ on $\kappa(\lambda)$ directly leads to wavelength-dependent CD and OR, the latter known as optical rotatory dispersion (ORD) [24, §9.2]. CD spectra can be measured by taking extinction spectra LCP and RCP light propagating through the material, and applying equation 2.29 at each wavelength, where E_{RCP} and E_{RCP} are the amplitudes of the transmitted RCP and LCP light respectively. Similarly, ORD spectra can be obtained by propagating linearly polarised light through the medium, and detecting the intensity of transmitted light through a rotatable analysing polariser. The analyser angle transmitting maximum intensity gives the resulting angle of polarisation, which can be compared to the incident polarisation to find the angle of optical rotation. Again, this can be taken at each wavelength to construct an ORD spectrum. It is important to reiterate however, that OR and CD depend on the real and imaginary parts of the same complex refractive index n. CD and ORD spectra are thus intrinsically linked by the Kramers-Kronig transforms [37, 38]: each can be obtained from the other, and they fundamentally contain the same information.

2.2.1 Chiroptical Effects from Extrinsic Chirality

It is possible to obtain a chiroptical response from structures that exhibit neither 3D nor planar chirality. Instead, chirality is introduced by the geometry of the experiment itself; the wave-vector, the surface normal and the direction of curvature on the structure form a chiral triad. The fundamental mechanism for this optical activity is shown in figure 2.3. When illuminated at normal incidence, the structure geometry remains unchanged when projected onto the transverse plane of the incident light (figure 2.3 left). However, when the sample is illuminated at an oblique angle the projection of the structure geometry onto the transverse plane of incident light becomes distorted. Under inversion, the structure's projection can no longer be superimposed onto itself by in-plane rotation, and is therefore planar chiral, as shown in figure 2.3 (right). If optical activity due to extrinsic chirality is measured at an oblique angle of incidence ϕ, then the chiroptical response should change sign when measured at an angle of incidence of $-\phi$. That is, any measured circular dichroism will reverse sign, and any optical rotation will rotate in the opposite direction. This can perhaps be more intuitively understood by considering the geometry shown in figure 2.3. The projection of the structure's mirror image at oblique incidence is identical to its own projection at the opposite angle of incidence. By reversing the angle of incidence, the chirality of the experimental geometry is reversed, and any chiroptical effects will correspondingly change sign. Plum et al. showed that asymmetric transmission

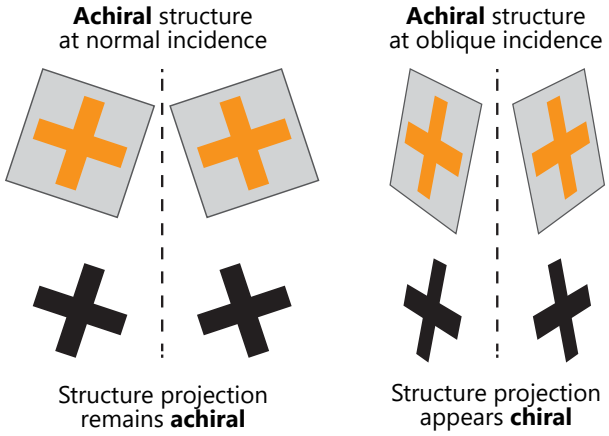

Figure 2.3: *Schematic representation of extrinsic chirality in an achiral structure.*

can occur in any structure whose projection onto the transverse plane of incident light is 2-dimensionally chiral and anisotropic [39]. It is therefore possible to achieve chiroptical effects utilising geometrically simpler structures than those that are intrinsically chiral.

For applications requiring manipulation of light polarisation, such as optical rotation or circular dichroism, it is perfectly possible to use extrinsic instead of intrinsic chirality. An early study by Plum et al., for example, measured a chiroptical response from achiral split-ring structures at microwave wavelengths [40]. These structures were shown to exhibit both circular dichroism and optical rotation when illuminated at oblique incidence. At normal incidence, no significant optical activity was measured for either structure. The circular birefringence resulted in rotation of linear polarisation exceeding 60° for microwaves. Later observations, directly comparing extrinsic and intrinsic chirality, con-

firmed that the former can yield significantly stronger response [41]. More recent work has pushed towards optical-wavelength chiroptical responses due to extrinsic chirality. Cao et al. demonstrated, experimentally and computationally, strong circular dichroism in the mid-IR region ($\approx 2.4\,\mu m$), resulting from extrinsic chirality in achiral metallic nanostructures [42]. Both enantiomorphs of the structure can be obtained by tilting the sample to opposite angles. This fact, it is suggested, can be utilised to simplify experiments requiring both enantiomers of a nanostructure, by removing the need to fabricate two separate structures. More recently, Belardini et al. have demonstrated strong chiroptical effects at *optical* wavelengths from a surface of tilted nanowires [43]. It was shown that upon rotating the sample by 180°, both the circular dichroism and angle of optical rotation change sign, as expected for extrinsic chirality. The same work also reported that extrinsic chirality affects nonlinear chiroptical measurements (discussed further in section 3) in a similar way. Nonlinear chiroptical measurements were taken as a function of the angle of incidence of light, for opposite orientations of the nanowires. As expected, the opposite orientations resulted in a reversal of the nonlinear chiroptical response. Additional work demonstrated the same dependency of the nonlinear chiroptical response on the angle of optical incidence, and that extrinsic chirality is induced by the relative angle between the light and the surface normal [44].

The relative simplicity of fabrication for achiral nanostructures could open the field to more readily available and easier to mass-produce geometries. The key here would be to consider the experimental geometry as a whole. However, in experiments aiming to characterise the chirality of materials at oblique incidence, contributions to measurable chiroptical effects from extrinsic chirality can complicate analysis. Importantly, extrinsic chirality can be identified by comparing the symmetry of contributions from intrinsic and extrinsic chirality. Chiroptical effects originating from true intrinsic chirality should be invariant upon rotation of the angle of incidence. Conversely, contributions originating from extrinsic chirality will reverse as the angle of incidence changes sign.

2.2.2 Chiroptical Effects from Anisotropy

It was shown earlier in section 2 that the rotation and circularly polarisation of linearly polarised light can occur in achiral, anisotropic materials. Despite applications in polarisation optics, structural anisotropy raises issues when characterising chiral systems. Within stereochemistry, chiroptical analysis historically tends to occur in isotropic, homogenous liquid molecular systems [45]. In these cases, the anisotropy of individual molecules has no significant effect on the macroscopically measured optical activity. This is due to the 3-dimensional averaging out of anisotropy for a large number of randomly oriented molecules. However, the work in this thesis makes use of planar metallic "nanomaterials", discussed in greater depth in section 4. These nanomaterials are commonly fabricated by patterning metallic inclusions onto a 2-dimensional surface, and so typically cannot be isotropically arranged.

Previous work has demonstrated that, towards the nanoscale, achiral, anisotropic structures can locally generate circularly polarised light [46]. Conversely, a linearly birefringent

material can convert circularly polarised light to linearly polarised light. Such birefringent materials can also exhibit linear dichroism (a difference in the absorption of orthogonal linearly polarisations). This can lead to an apparent circular dichroism, actually the combined effect of linear birefringence and linear dichroism. Likewise, the operation of half-wave plates demonstrates the ability for anisotropic, achiral media to result in significant optical rotation of linearly polarised light. When characterising the chirality of anisotropic structures, there is thus a prevailing need for experimental techniques capable of disentangling contributions from anisotropy and intrinsic chirality. Fortunately, chiroptical contributions from anisotropy can also be identified with symmetry considerations. Any chiroptical effects measured due to an isotropic structure's intrinsic chirality will be invariant under structure rotation. Conversely, chiroptical effects originating exclusively from anisotropy will necessarily vary as the structure is rotated, reversing sign upon 90° rotation normal to the fast and slow axis of the material. However, this periodic sign change is not strictly necessary in structures that exhibit both intrinsic or extrinsic chirality *and* structural anisotropy. In these cases, the two contributions are effectively competing, and complex chiroptical behaviour can emerge [8]. Isolating the structural chirality from anisotropy and extrinsic chirality is therefore challenging, especially in planar nanomaterials which are often highly anisotropic. In sections 6 and 7 two methods of experimentally isolating the intrinsic chirality of metallic nanomaterials are explored.

2.3 Optical Chirality and "Superchiral" Light

The interaction between a chiral molecule and a chiral electromagnetic field is expected to exhibit a dissymmetry, in that each "handedness" of a chiral field should interact differently with a chiral molecule or nanostructure. A field with a shorter chiral pitch, the distance over which the polarisation vector completes a 360° twist, will exhibit a stronger interaction dissymmetry than a less twisted field. It had long been thought that the maximum possible chiral dissymmetry is obtained for a perfectly circularly polarised monochromatic field, however in 2010 Tang and Cohen proposed a setup in which the dissymmetry exceeds that of CPL (referred to as "superchiral light") at the nodes of a chiral standing wave. [47] The strength of the field chirality can be quantified by Lipkin's 00-zilch density [48] referred to by Tang and Cohen as the "optical chirality" C as defined in equation 2.31. This quantity is a time-even pseudo-scalar, as would be expected for a measure of intrinsic chirality.

$$\begin{aligned} C =& \frac{\varepsilon_0}{2}\tilde{\mathbf{E}} \cdot (\nabla \times \tilde{\mathbf{E}}) + \frac{1}{2\mu_0}\tilde{\mathbf{B}} \cdot (\nabla \times \tilde{\mathbf{B}}) \\ =& -\frac{\varepsilon_0 \omega}{2} \operatorname{Im}[\tilde{\mathbf{E}}(\mathbf{r}) \cdot \tilde{\mathbf{B}}(\mathbf{r})] \end{aligned} \tag{2.31}$$

Here, $\tilde{\mathbf{E}}$ and $\tilde{\mathbf{B}}$ denote the complex electric and magnetic field amplitudes respectively. The optical chirality relates to the spin angular momentum of the field [49], and describes the degree to which the electric and magnetic field lines wrap around a helical axis [47, 50]. Tang and Cohen showed that the enantioselectivity of optical excitation of a molecule is

highly dependent on C, and so it stands that such a superchiral field can lead to significant enhancement of the enantioselective excitation of chiral molecules.

The general microscopic response of a chiral molecule to a monochromatic electromagnetic field is described by an induced electric dipole moment $\tilde{\mathbf{p}}$ and magnetic dipole moment $\tilde{\mathbf{m}}$ as in equation 2.32.

$$\begin{aligned}\tilde{\mathbf{p}} &= \tilde{\alpha}_{ee}\tilde{\mathbf{E}} - i\tilde{\alpha}_{em}\tilde{\mathbf{B}} \\ \tilde{\mathbf{m}} &= i\tilde{\alpha}_{em}\tilde{\mathbf{E}} + \tilde{\alpha}_{mm}\tilde{\mathbf{B}}\end{aligned} \tag{2.32}$$

Here, $\tilde{\alpha}_{ee}$ and $\tilde{\alpha}_{mm}$ correspond to $\tilde{\alpha}$ and $\tilde{\chi}$ in references [47] and [51], α_{ee} is the electric polarisability, and α_{mm} is the magnetic susceptibility. $\tilde{\alpha}_{em}$ is the mixed magneto-electric polarisability and is directly related to the material chirality parameter κ (section 2.1). Physical quantities are obtained from the real parts of equation (14). For an incident electric field $\tilde{\mathbf{E}} = \tilde{\mathbf{E}}_0 e^{-i\omega t}$ and $\tilde{\mathbf{B}} = \tilde{\mathbf{B}}_0 e^{-i\omega t}$ the rate of excitation of a molecule from right (+) and left (−) CPL is given by equation 2.33 [47, 51].

$$A^{\pm} = \frac{\omega}{2}\langle \mathbf{E}\cdot\dot{\mathbf{p}} + \mathbf{B}\cdot\dot{\mathbf{m}}\rangle_t = \frac{\omega}{2}\mathrm{Im}(\tilde{\mathbf{E}}^*\cdot\tilde{\mathbf{p}} + \tilde{\mathbf{B}}^*\cdot\tilde{\mathbf{m}}) \tag{2.33}$$

Substituting equation 2.32 into equation 2.33 leads to equation 2.34, which can be rewritten in terms of the generalised optical chirality C to give equation 2.35 [51]. Here $\tilde{\alpha}''_{em} = \mathrm{Im}(\tilde{\alpha}_{em})$.

$$A^{\pm} = \frac{\omega}{2}(\tilde{\alpha}''_{ee}\left|\tilde{\mathbf{E}}\right|^2 + \tilde{\alpha}''_{mm}\left|\tilde{\mathbf{B}}\right|^2) \pm \tilde{\alpha}''_{em}\omega\mathrm{Im}(\tilde{\mathbf{E}}^*\cdot\tilde{\mathbf{B}}) \tag{2.34}$$

$$A^{\pm} \simeq \frac{\omega}{2}(\tilde{\alpha}''_{ee}\left|\tilde{\mathbf{E}}\right|^2 + \tilde{\alpha}''_{mm}\left|\tilde{\mathbf{B}}\right|^2) \pm \tilde{\alpha}''_{em}\frac{2}{\varepsilon}C \tag{2.35}$$

The time averaged electric and magnetic energy densities $\langle U_E\rangle_t = \frac{\varepsilon}{4}\left|\tilde{\mathbf{E}}\right|^2$ and $\langle U_B\rangle_t = \frac{1}{4\mu}\left|\tilde{\mathbf{B}}\right|^2$ can be introduced here, and substituted into equation 2.35 to give the rate of excitation in terms of energy density as in equation 2.36.

$$\begin{aligned}A^{\pm} &\simeq \frac{2}{\varepsilon}\tilde{\alpha}''_{ee}\omega\left(\langle U_E\rangle_t + \gamma\langle U_B\rangle_t\right) \pm \tilde{\alpha}''_{em}\frac{2}{\varepsilon}C \\ \gamma &= \frac{\tilde{\alpha}''_{mm}}{\tilde{\alpha}''_{ee}}\varepsilon\mu = \frac{\tilde{\alpha}''_{mm}}{\tilde{\alpha}''_{ee}}\frac{n^2}{c^2}\end{aligned} \tag{2.36}$$

We can now define the dissymmetry factor g of the chiroptical interaction by equation 2.37.

$$g = \frac{A^+ - A^-}{\frac{1}{2}(A^+ + A^-)} \tag{2.37}$$

In Tang and Cohen's proposal [47] the magnetic field was disregarded as negligible. Under this assumption, the dissymmetry factor is found to be

$$g = -\frac{\tilde{\alpha}''_{em}}{\tilde{\alpha}''_{ee}}\frac{2C}{\omega\langle U_E\rangle_t} \tag{2.38}$$

Note that under this approximation, the dissymmetry factor splits into properties of the

molecule only ($\tilde{\alpha}''_{em}/\alpha''_{ee}$) and properties of the field only ($2C/\omega\langle U_E\rangle_t$), however in the general case the dissymmetry factor cannot be separated in this way and is significantly more complex [51]. The full expression accounting for magnetic energy density can be simplified by assuming a small dissymmetry factor such that $n_+ \approx n_-$, to give equation 2.39. [51]

$$g = -\frac{\tilde{\alpha}''_{em}}{\tilde{\alpha}''_{ee}} \frac{2C}{\omega[\langle U_E\rangle_t + \gamma\langle U_B\rangle_t]} \tag{2.39}$$

The limitation in chiroptical enhancement is now clear: in regions of low electric energy density, the magnetic energy density is maximised and should not be considered negligible. The γ term in equation 2.39 is then the key limiting factor for the dissymmetry enhancement. The energy density terms in the denominator can no longer be reduced to arbitrarily small values in order to continually increase chiral dissymmetry. However, the chiral dissymmetry can still be increased by reducing the total electromagnetic energy density, increasing the structural chirality parameter of the medium, and increasing optical chirality C of the electromagnetic field.

Despite these limitations, Tang and Cohen experimentally verified enhanced chiral dissymmetry using superchiral nodes on a standing wave, as previously proposed. By comparing the fluorescence emission of chiral and achiral molecular layers under left- and right-polarised superchiral standing waves, they demonstrated an $11\times$ dissymmetry enhancement compared to circularly polarised light [50]. This experimental configuration has clear practical limitations however, in that the target sample must be positioned at, or near, a node of a standing wave. Slight positional deviations of the sample, or the partially reflecting mirror, could easily result in the sample entering an anti-node, at which the optical chirality is minimised. To alleviate this limitation, experimental configurations have been proposed that fix the positioning of the standing wave, and the sample surface. Rather than using a partially reflective mirror to generate a standing wave, periodic photonic crystal structures have been used to form Bloch waves, which can lead to superchiral nodes at fixed positions through the photonic crystal structure [52, 53, 54]. By designing the structure and angle of optical incidence such that a node of high optical chirality occurs at the termination surface of the structure, chiral fields can be formed over large surface areas, used for sensing and characterisation of molecules attached to the material surface [52, 53]. These superchiral Bloch waves have been used to demonstrate two orders of magnitude increase in circular dichroism signal compared to probing with circularly polarised light [53]. Typically however, a more common method of experimentally realising superchiral light is the use of plasmonic nanomaterials, capable of generating periodic small regions of high optical chirality at the surface of a quasi-2-dimensional material. This is discussed further in section 4.1.3.1.

2.4 Conclusions

Across a wide range of research fields, chirality, the lack of mirror symmetry, is a key structural property, especially prevalent in biomolecular systems. Particularly, many pharmaceutical drugs are chiral, with enantiomers often exhibiting dramatically different medical

effects. Because of this, chiral optical (chiroptical) effects have become a widespread method for characterising the structural properties of complex molecular systems. We have shown that structural anisotropy can be utilised to form chiral polarisation states of light, which can in turn be used to directly probe material chirality. By considering the propagation of light through a medium exhibiting coupling between induced electric and magnetic dipoles, we have shown that left- and right-circularly polarised light will propagate through a chiral medium with different refractive indices. This chiral dissymmetry directly leads to circular dichroism, and optical rotation, two measurable probes of the real and imaginary parts of the chiral medium's refractive index. In section 2.3, it was shown that, perhaps contrary to intuition, pure circularly polarised light does not necessarily lead to the strongest chiral dissymmetry. In fact, by interfering circularly polarised fields, the nodes of an elliptically polarised standing wave can exhibit a twisted field gradient stronger than that of CPL. This has allowed for molecular chiroptical measurements with significantly greater sensitivity than those undertaken with pure circularly polarised light. As well as "superchiral" configurations, enhanced chiroptical sensitivity has been demonstrated by making use of nonlinear optics; an extremely symmetry-sensitive frequency conversion effect within media driven by intense electromagnetic fields. The following section discusses the microscopic origin of nonlinear scattering, the macroscopic descriptions of nonlinear media, and the symmetry properties of second-harmonic generation in particular, for use in chiroptical characterisation measurements.

Chapter 3

Nonlinear Optics

In this section we will discuss how nonlinear optics can be used as a sensitive probe for structural symmetry, in particular chirality. This will primarily focus on second-harmonic generation (SHG), and the macroscopic description of SHG in nonlinear media. By considering the symmetry of tensors describing the nonlinear properties of a dielectric medium, it is revealed that SHG is a highly sensitive technique for probing chirality. Chiroptical effects at the second-harmonic provide valuable intrinsic background reduction, and entirely new information compared to linear chiroptical effects discussed previously. First however, we will first consider the microscopic behaviour of a single oscillating dipole used to describe the origin of nonlinear optical behaviour.

3.1 The Lorentz Oscillator

In the Lorentz model of an oscillating dipole driven by a time-varying electric field $E(t)$, the 1-dimensional motion of an electron, with an effective mass m_0 and charge $-q$, in a harmonic potential $U(x) = (1/2)kx^2$ is described by equation 3.1 [55, §9.4][25, §2.2.1]

$$m_0\frac{d^2x}{dt^2} + m_0\gamma\frac{dx}{dt} + m_0\omega_0^2 x = -qE(t). \tag{3.1}$$

Here, x is the positional displacement of the electron, and $m_0\gamma\frac{dx}{dt}$ describes a damping force for a damping ratio γ. ω_0 describes the resonant frequency of the system, and is defined in terms of a spring constant k by $\omega_0 = \sqrt{k/m_0}$. The restoring force $-m_0\omega_0^2 x = -kx$ is related to the potential $U(x)$ by

$$F_{restoring} = -\frac{d}{dx}U(x) = -\frac{d}{dx}(1/2)kx^2 = -kx. \tag{3.2}$$

The displacement $x(t)$ of the electron, of charge e, results in a dipole moment $p(t) = -ex(t)$, leading to a macroscopic induced polarisation of a material given by $P(t) = Np(t)$ where N is the number of oscillators per unit volume [23, §3.5.1].

In the case of a driving field $E(t) = \mathrm{Re}[E_0 e^{-i(\omega t+\phi_E)}]$, oscillating at a frequency ω with a phase ϕ_E, solutions for $x(t)$ take the form of $x(t) = \mathrm{Re}[x_0 e^{-i(\omega t+\phi_x)}]$. Phase information is encoded by making x_0 and E_0 complex, and so these expressions can be substituted

into equation 3.1 and solved for x_0 giving

$$x_0 = \frac{-qE_0}{m_0(\omega_0^2 - \omega^2 - i\gamma\omega)}. \tag{3.3}$$

The macroscopic induced polarisation $P(t) = Nqx(t)$ is now given by equation 3.4 [25, §2.2.1].

$$\begin{aligned} P(t) =& Nq\left(\frac{-qE_0}{m_0(\omega_0^2 - \omega^2 - i\gamma\omega)}\right)\mathrm{Re}[e^{-(i\omega t)}] \\ =& \frac{Nq^2}{m_0}\left(\frac{1}{\omega_0^2 - \omega^2 - i\gamma\omega}\right)\mathrm{Re}[E_0 e^{-(i\omega t)}] \\ =& \frac{Nq^2}{m_0}\left(\frac{1}{\omega_0^2 - \omega^2 - i\gamma\omega}\right)E(t). \end{aligned} \tag{3.4}$$

We can now introduce the macroscopic electric susceptibility χ, such that the induced polarisation $P(t)$ can be directly related to the electric field by $P(t) = \varepsilon_0\chi E(t)$. In the linear case given in equation 3.4, the susceptibility is given by

$$\chi = \frac{Nq^2}{\varepsilon_0 m_0}\left(\frac{1}{\omega_0^2 - \omega^2 - i\gamma\omega}\right) \tag{3.5}$$

In the frequency domain, when driving at a frequency ω this notation can be equivalently given as $P(\omega) = \varepsilon_0\chi(\omega)E(\omega)$.

3.1.1 Nonlinear Terms

A more general anharmonic potential contains higher-order terms, and can be described by $U(x) = (1/2)kx^2 + (1/3)\beta_2 x^3 + (1/4)\beta_3 x^4 + ...$ The corresponding restoring force leads to an equation of motion

$$\frac{d^2x}{dt^2} + \gamma\frac{dx}{dt} + \omega_0^2 x + \beta_2 x^2 + \beta_3 x^3 + ... = -\frac{q}{m_0}E(t). \tag{3.6}$$

For an oscillating $E(t)$, solving for $x(t)$ is difficult, however we can make use of the fact that, in general, $\omega_0^2 \ll \beta_2 \ll \beta_3 \ll ...$ to describe the nonlinearity as a small perturbation to the system, and find a power series solution. We introduce a parameter a characterising the perturbation, and make the substitutions $E(t) \to aE(t)$ and $x \to ax_1 + a^2x_2 + a^3x_3 + ...$ into equation 3.6. In order for this expansion of x to be a valid solution, each term in equation 3.6, when grouped by powers of a, must satisfy the equation separately [56, §1.4.1]. Equations of motion for the lowest three orders thus take the forms of [56, §1.4.1]:

$$\begin{aligned} &\frac{d^2x_1}{dt^2} + \gamma\frac{dx_1}{dt} + \omega_0^2 x_1 = -\frac{q}{m_0}E(t) \\ &\frac{d^2x_2}{dt^2} + \gamma\frac{dx_2}{dt} + \omega_0^2 x_2 = \beta_2 x_1^2 \\ &\frac{d^2x_3}{dt^2} + \gamma\frac{dx_3}{dt} + \omega_0^2 x_3 = 2\beta_2 x_1 x_2 + \beta_3 x_1^3 \\ &... \end{aligned} \tag{3.7}$$

For convenience we introduce the denominator function $D(\omega)$, and again consider a system driven by an electric field oscillating at a frequency ω.

$$D(\omega) = \omega_0^2 - \omega^2 - i\gamma\omega \tag{3.8}$$

The lowest-order in equation 3.7 (x_1) is equivalent to the system described by equation 3.1. As equation 3.3 provides an expression for our x_1 term, x_1 can be given in terms of the denominator function as

$$x_1(t) = \frac{-q}{m_0 D(\omega)} E_0 e^{-i\omega t}. \tag{3.9}$$

Squaring $x_1(t)$ and substituting in to the second-order expression in equation 3.7 to obtain $x_2(t)$ gives both a DC component ($\omega = 0$), and components oscillating at $\pm 2\omega$, proportional in amplitude to E_0^2 [56, §1.4.1], described by

$$x_2(t)|_{\mp 2\omega} = \frac{\beta_2 q^2}{m_0^2 D(\pm 2\omega) D^2(\omega)} E_0^2 e^{\pm i 2\omega t} \tag{3.10}$$

This is a specific degenerate case of second-order nonlinearity, where the driving field oscillates at a single frequency ω. More generally, second-order nonlinear effects can be driven by two fields oscillating at different frequencies ω_1 and ω_2, with complex amplitudes E_{ω_1} and E_{ω_2} respectively. In this case, $x_2(t)$ has components oscillating at $\omega_1 \pm \omega_2$ described by equation 3.11 [56, §1.4.1].

$$x_2(t)|_{\omega_1 \pm \omega_2} = \frac{\beta_2 q^2}{m_0^2 D(\omega_1 \pm \omega_2) D(\omega_1) D(\pm\omega_2)} E_{\omega_1} E_{\omega_2} e^{i(\omega_1 \pm \omega_2)t}. \tag{3.11}$$

In this work, however, we will focus on the degenerate case of second-order nonlinearity, resulting in motion at 2ω.

Following from equation 3.4, from the second-order nonlinear term $x_2(t)$ results in an additional component in the induced polarisation, $P(t)|_{\mp 2\omega} = Nqx_2(t)|_{\mp 2\omega}$, oscillating at 2ω and proportional to E_0^2. The second-order electric susceptibility $\chi^{(2)}$ is introduced to describe the second-order polarisation, such that $P(2\omega) = \varepsilon_0 \chi^{(2)} E(\omega)^2$. Higher-order nonlinearity is described by additional components in the induced polarisation, characterised by higher-order susceptibilities $\chi^{(n)}$.

3.2 The Dielectric Susceptibility

The general, 3-dimensional, macroscopic response of a material to an electric field is described by susceptibility tensors, as shown in equation 3.12 [56, §1.1].

$$P_i(t) = \epsilon_0 \big[\chi_{ij}^{(1)} E_j(t) + \chi_{ijk}^{(2)} E_j(t) E_k(t) + \chi_{ijkl}^{(3)} E_j(t) E_k(t) E_l(t) + \dots \big]. \tag{3.12}$$

Here each of the indices $i, j, k, l, \dots$ are the Cartesian directions of the associated field (ie. each index can take on x, y, or z.) For each higher-order term, an additional field is required, and the rank of the associated susceptibility tensor increases accordingly. We also find that even harmonics require a material lacking inversion symmetry. Under inversion

we apply $\mathbf{r} \to -\mathbf{r}$, hence $\mathbf{P} \to -\mathbf{P}$, and $\mathbf{E} \to -\mathbf{E}$. For a centrosymmetric medium, it follows that $\mathbf{P}(-\mathbf{E}) = -\mathbf{P}(\mathbf{E})$, and so by equating components, for any even n terms, $\chi^{(n)} = -\chi^{(n)}$ meaning $\chi^{(n)} = 0$. Generally, any odd/even rank Cartesian tensors are odd/even under parity inversion. Therefore, nonlinear processes at even-order harmonics are forbidden in centrosymmetric media.

3.2.1 Linear Electric Dipoles

The 3-dimensional linear response of a material in the dipole approximation can be described entirely by the first-order term in equation 3.12. In the frequency domain, this becomes

$$P_i(\omega) = \epsilon_0 \chi^{(1)}_{ij}(\omega) E_j(\omega). \tag{3.13}$$

In vector notation, this is given explicitly by

$$\mathbf{P}(\omega) = \epsilon_0 \begin{bmatrix} \chi_{xx} & \chi_{xy} & \chi_{xz} \\ \chi_{yx} & \chi_{yy} & \chi_{yz} \\ \chi_{zx} & \chi_{xy} & \chi_{zz} \end{bmatrix} \cdot \mathbf{E}_1(\omega). \tag{3.14}$$

When studying nonlinear effects, the emitted radiation from the linear response will still be present, and is almost always significantly stronger than the nonlinear response.

3.2.2 Second-Order Electric Dipoles

For second-order effects $\chi^{(2)}_{ijk}$ is a rank 3 tensor of 27 components, which can be fully represented by equation 3.15 [57].

$$\chi^{(2)}_{ijk} = \begin{bmatrix} \chi_{xxx} & \chi_{xyy} & \chi_{xzz} & \chi_{xyz} & \chi_{xzy} & \chi_{xzx} & \chi_{xxz} & \chi_{xxy} & \chi_{xyx} \\ \chi_{yxx} & \chi_{yyy} & \chi_{yzz} & \chi_{yyz} & \chi_{yzy} & \chi_{yzx} & \chi_{yxz} & \chi_{yxy} & \chi_{yyx} \\ \chi_{zxx} & \chi_{zyy} & \chi_{zzz} & \chi_{zyz} & \chi_{zzy} & \chi_{zzx} & \chi_{zxz} & \chi_{zxy} & \chi_{zyx} \end{bmatrix} \tag{3.15}$$

Second-order nonlinear effects require two fields, however in practice these can be a single high-intensity field. We will first consider the general case allowing for two separate fields.

In the frequency domain, two input fields $E_j(\omega_p)$ and $E_k(\omega_q)$ lead to an internal polarisation $P_i(\omega_p \pm \omega_q)$. As seen earlier, the susceptibility must now contain information about the response to three fields (two in, one out), each in three dimensions. The polarisation is then described by equation 3.16 [56, §1.3].

$$P_i(\omega = \omega_p \pm \omega_q) = \epsilon_0 \sum_{jk} \sum_{(pq)} \chi^{(2)}_{ijk}(\omega, \omega_p, \omega_q) E_j(\omega_p) E_k(\omega_q). \tag{3.16}$$

The sum $\sum_{(pq)}$ is over fields whose frequencies sum to a fixed $\omega = \omega_p \pm \omega_q$. For two distinct input fields, at ω_1 and ω_2, ω_p and ω_q can each take one of these two values. This

means that for known but different input frequencies, the polarisation can be given by

$$P_i(\omega = \omega_1 + \omega_2) = \epsilon_0 \sum_{jk} \left[\chi^{(2)}_{ijk}(\omega, \omega_1, \omega_2) E_j(\omega_1) E_k(\omega_2) + \chi^{(2)}_{ijk}(\omega, \omega_2, \omega_1) E_j(\omega_2) E_k(\omega_1).\right] \tag{3.17}$$

Due to permutation symmetry, where $E_j(\omega_1) = E_k(\omega_1)$ and $E_j(\omega_2) = E_k(\omega_2)$, this reduces to [56, eq. 1.3.15]

$$P_i(\omega = \omega_1 + \omega_2) = \epsilon_0 \sum_{jk} 2\chi^{(2)}_{ijk}(\omega, \omega_1, \omega_2) E_j(\omega_1) E_k(\omega_2). \tag{3.18}$$

For second-harmonic generation, we consider the case of a single input field, where now $\omega_p = \omega_q = \omega_1$, resulting in a polarisation $P_i(\omega = 2\omega_1)$. In this case, the sum $\sum_{(pq)}$ collapses to a single term, and the polarisation is described by

$$P_i(\omega = 2\omega_1) = \epsilon_0 \sum_{jk} \chi^{(2)}_{ijk}(\omega, \omega_1, \omega_1) E_j(\omega_1) E_k(\omega_1). \tag{3.19}$$

The measurable second-harmonic electric field $\mathbf{E}(2\omega)$ can then be obtained from $\mathbf{E}(2\omega) \sim [\mathbf{n} \times \mathbf{P}(2\omega)] \times \mathbf{n}$, where $\mathbf{P}(2\omega)$ is a vector describing the induced polarisation from equation 3.19, and $\mathbf{n}$ is a unit vector describing the angle of observation.

3.2.3 Reducing $\chi^{(2)}$ with Permutation Symmetry

Since $E_j(\omega_1)$ and $E_k(\omega_1)$ are indistinguishable for a single input beam, in the case of SHG we can reduce $\chi^{(2)}_{i,j,k}$ to a 3×6 matrix. This is because (for j,k) x, y and y, x are equal, x, z and z, x are equal, and z, y and y, z are equal. We need only consider half of these terms, and terms where $j = k$ [56, §1.5.2]. We define our new matrix d_{il} with the replacements in table 3.1.

Table 3.1

j,k:	1,1	2,2	3,3	2,3 or 3,2	1,3 or 3,1	1,2 or 2,1
l:	1	2	3	4	5	6

The remaining terms are then rearranged, reducing from equation 3.15 to

$$d_{il} = \begin{pmatrix} \chi_{xxx} & \chi_{xyy} & \chi_{xzz} & \chi_{xyz} & \chi_{xzx} & \chi_{xyx} \\ \chi_{yxx} & \chi_{yyy} & \chi_{yzz} & \chi_{yzy} & \chi_{yzx} & \chi_{yxy} \\ \chi_{zxx} & \chi_{zyy} & \chi_{zzz} & \chi_{zyz} & \chi_{zxz} & \chi_{zyx} \end{pmatrix} \tag{3.20}$$

Following the same reduction and rearrangement, the tensor product of the fields under permutation symmetry is also reduced, leaving the polarisation for second-harmonic

generation in 3 dimensions in the form of equation 3.21 [58, §38.3].

$$\begin{pmatrix} P_x \\ P_y \\ P_z \end{pmatrix} = \begin{pmatrix} \chi_{xxx} & \chi_{xyy} & \chi_{xzz} & \chi_{xyz} & \chi_{xzx} & \chi_{xyx} \\ \chi_{yxx} & \chi_{yyy} & \chi_{yzz} & \chi_{yzy} & \chi_{yzx} & \chi_{yxy} \\ \chi_{zxx} & \chi_{zyy} & \chi_{zzz} & \chi_{zyz} & \chi_{zxz} & \chi_{zyx} \end{pmatrix} \begin{pmatrix} E_x E_x \\ E_y E_y \\ E_z E_z \\ 2E_y E_z \\ 2E_z E_x \\ 2E_x E_y \end{pmatrix} \tag{3.21}$$

3.2.4 Reducing $\chi^{(2)}$ with Rotational Symmetry

The number of tensor components can also be reduced by considering rotational symmetry. If we rotate the system by an angle θ about a particular axis, we can define the new, rotated axes by applying a set of coordinate transformations. For example, rotating in the $x-y$ plane, about the z axis, applies the transformations

$$\begin{aligned} x &\to x\cos\theta - y\sin\theta \\ y &\to x\sin\theta + y\cos\theta \\ z &\to z. \end{aligned} \tag{3.22}$$

In matrix notation, this is given by

$$\begin{pmatrix} x' \\ y' \\ z' \end{pmatrix} = \begin{bmatrix} \cos\theta & -\sin\theta & 0 \\ \sin\theta & \cos\theta & 0 \\ 0 & 0 & 1 \end{bmatrix} \begin{pmatrix} x \\ y \\ z \end{pmatrix}. \tag{3.23}$$

Following the same reasoning, we reach the matrices for rotating about each coordinate axis.

$$\begin{aligned} R^z(\theta_z)_{ij} &= \begin{bmatrix} \cos\theta_z & -\sin\theta_z & 0 \\ \sin\theta_z & \cos\theta_z & 0 \\ 0 & 0 & 1 \end{bmatrix} \\ R^y(\theta_y)_{ij} &= \begin{bmatrix} \cos\theta_y & 0 & \sin\theta_y \\ 0 & 1 & 0 \\ -\sin\theta_y & 0 & \cos\theta_y \end{bmatrix} \\ R^x(\theta_x)_{ij} &= \begin{bmatrix} 1 & 0 & 0 \\ 0 & \cos\theta_x & -\sin\theta_x \\ 0 & \sin\theta_x & \cos\theta_x \end{bmatrix} \end{aligned} \tag{3.24}$$

Rotations around multiple axes can then be solved by applying successive rotation matrices in the same way.

For rotational symmetry in the $x-y$ plane, we first rotate the tensor by the angle corresponding to our symmetry using

$$\chi'_{ijk} = R^z(\theta)_{i\alpha} R^z(\theta)_{j\beta} R^z(\theta)_{k\gamma} \chi^{(2)}_{\alpha\beta\gamma}. \tag{3.25}$$

Due to symmetry, the tensor should remain unchanged under this transformation, and so we impose the equality $\chi'_{ijk} = \chi_{ijk}$ to find any component dependencies. Solving for rotational symmetry can show various tensor components as being dependant, or necessarily equalling zero. Examples of this are given in Appendix A.

C_4 Symmetry and Rotational Isotropy It is worth making note of the special case of planar 4-fold rotational symmetry (C_4 symmetry in Schoenflies notation), whose tensor and dependencies are found in Appendix A.1. Due to the set of dependencies and vanishing components, applying an arbitrary $x-y$ rotation to the C_4 tensor results in no change of any components.

Furthermore, a structure is isotropic (C_∞ in Schoenflies notation) when the tensor remains unchanged under any rotation. In tensor notation, for any value of θ we can say that in an isotropic structure

$$R(\theta_z)_{i\alpha}R(\theta_z)_{j\beta}R(\theta_z)_{k\gamma}\chi^{(2)}_{\alpha\beta\gamma} = \chi^{(2)}_{ijk} \tag{3.26}$$

Since this condition is met for a C_4 tensor, 2-dimensional rotational isotropy is found to give the same tensor dependencies as under C_4 symmetry [59, §E.1.8]. In full, we find that for both C_4 and C_∞ structures, the tensors can be reduced to

$$\chi^{(2)}_{ijk} = \begin{bmatrix} 0 & 0 & 0 & \chi_{xyz} & \chi_{xzy} & \chi_{xzx} & \chi_{xxz} & 0 & 0 \\ 0 & 0 & 0 & \chi_{yyz} & \chi_{yzy} & \chi_{yzx} & \chi_{yxz} & 0 & 0 \\ \chi_{zxx} & \chi_{zyy} & \chi_{zzz} & 0 & 0 & 0 & 0 & \chi_{zxy} & \chi_{zyx} \end{bmatrix} \tag{3.27}$$

with dependencies given by

$$\begin{aligned} &\chi_{xyz} = -\chi_{yxz}, \chi_{xzy} = -\chi_{yzx}, \chi_{xzx} = \chi_{yzy} \\ &\chi_{xxz} = \chi_{yyz}, \chi_{zxx} = \chi_{zyy}, \chi_{zxy} = -\chi_{zyx} \\ &\chi_{zzz} \end{aligned} \tag{3.28}$$

3.2.5 Reducing $\chi^{(2)}$ with Mirror Symmetry

So far we have only considered structure lacking mirror symmetry, that is those which are chiral. The application of mirror symmetry for achiral structures can further reduce the number of independent tensor components.

A reflection in the y-z plane can be described by a transformation matrix

$$A^y_{ij} = \begin{bmatrix} -1 & 0 & 0 \\ 0 & 1 & 0 \\ 0 & 0 & 1 \end{bmatrix} \tag{3.29}$$

If the line of mirror symmetry lies at an angle relative to this, the rotation matrices in equation 3.24 can be applied to the system first.

Under mirror symmetry about the y axis, we impose the equality

$$A^y_{i\alpha}A^y_{j\beta}A^y_{k\gamma}\chi^{(2)}_{\alpha\beta\gamma} = \chi^{(2)}_{ijk}. \tag{3.30}$$

From here, the initial and reflected tensors can be compared. It is found that the general tensor for such an achiral structure reduces to

$$\chi^{(2)}_{ijk} = \begin{bmatrix} 0 & 0 & 0 & 0 & 0 & \chi_{xzx} & \chi_{xxz} & \chi_{xxy} & \chi_{xyx} \\ \chi_{yxx} & \chi_{yyy} & \chi_{yzz} & \chi_{yyz} & \chi_{yzy} & 0 & 0 & 0 & 0 \\ \chi_{zxx} & \chi_{zyy} & \chi_{zzz} & \chi_{zyz} & \chi_{zzy} & 0 & 0 & 0 & 0 \end{bmatrix} \tag{3.31}$$

These component reductions can then be applied on top of any other symmetries exhibited by the structure.

Chiral Isotropic Structures Another special case worth noting regards mirror symmetry in planar isotropic (and C_4) structures. Under mirror symmetry, the C_4/C_∞ tensor (equation 3.28) reduces to

$$\chi^{(2)}_{ijk} = \begin{bmatrix} 0 & 0 & 0 & 0 & 0 & \chi_{xzx} & \chi_{xxz} & 0 & 0 \\ 0 & 0 & 0 & \chi_{yyz} & \chi_{yzy} & 0 & 0 & 0 & 0 \\ \chi_{zxx} & \chi_{zyy} & \chi_{zzz} & 0 & 0 & 0 & 0 & 0 & 0 \end{bmatrix} \tag{3.32}$$

Since only 3 independent components are removed, the chirality of an isotropic structure can be fully described by the following components:

$$\chi_{xyz} = -\chi_{yxz}, \chi_{xzy} = -\chi_{yzx}, \chi_{zxy} = -\chi_{zyx} \tag{3.33}$$

In the case of SHG, applying permutation symmetry reduces this further to

$$d_{il} = \begin{pmatrix} 0 & 0 & 0 & 0 & \chi_{xzx} & 0 \\ 0 & 0 & 0 & \chi_{yzy} & 0 & 0 \\ \chi_{zxx} & \chi_{zyy} & \chi_{zzz} & 0 & 0 & 0 \end{pmatrix} \tag{3.34}$$

The chirality is now described by a single pseudo-scalar term, since under permutation symmetry $\chi_{xyz} = -\chi_{yzx}$. Because of this, for C_4/C_∞ structures the chiral contribution to SHG is often parametrised by this single "chiral component" χ_{xyz}.

3.3 Second-Harmonic Generation as a Probe of Chirality

From section 3.2 we know that non-zero SHG intrinsically requires a lack of centrosymmetry. For chiroptical measurements, this presents a clear advantage over the analysis of linear chiroptical effects. In linear measurements, any achiral background will contribute to the overall measured signal, reducing the contrast of chiroptical effects. However, a centrosymmetric, achiral bulk material cannot result in even-order nonlinear emission: SHG is forbidden, and so the achiral background is removed. In a system of chiral molecules amongst an achiral background, only the chiral structures, and weak contributions from

surface interfaces, can contribute to SHG. This intrinsic background removal can significantly increase the contrast in chiroptical dissymmetry.

Aside from the background-reduction advantages, a somewhat more subtle advantages is also presented: Unlike linear chiroptical effects which *require* coupling between electric dipoles and, typically weak, magnetic dipoles (section 2.1), we have shown in section 3.2.5 that any structure lacking mirror symmetry can have a chiral contribution to SHG within the electric dipole approximation alone. In second-harmonic generation experiments, analogues of linear circular dichroism and optical rotation can thus be measured. Second-harmonic generation optical rotation (SHG-OR) closely follows the definition discussed in section 2.2: The angle of SHG-OR is given by the angle between the incident polarisation axis, and the angle of linearly polarised SHG from the material. The nonlinear analogue of circular dichroism is, however, somewhat less clearly defined. Often, SHG optical activity experiments measure a difference in the SHG *intensity* from RCP and LCP incident light, I_{RCP} and I_{LCP} respectively, and normalised to $(I_{RCP}-I_{LCP})/(I_{RCP}+I_{LCP})$. Contrary to circular dichroism in linear optics (see equation 2.29, this quantity typically gives no spectral information, and relates to the field intensity, rather than amplitude. While sometimes still referred to as circular dichroism, a more suitable name would be "circular intensity difference" (CID), as used commonly in Raman optical activity measurements [60, §1.4]. In this work, SHG-CID will be used, defined by

$$\text{SHG-CID} = \frac{I_{RCP}^{SHG} - I_{LCP}^{SHG}}{I_{RCP}^{SHG} + I_{LCP}^{SHG}}. \tag{3.35}$$

Importantly, since the electric-dipole-only mechanism of the SHG chiroptical effects is fundamentally different to their linear chiroptical counterparts, SHG-CID and SHG-OR are not intrinsically linked by any simple relation. The two effects provide complementary information, allowing for more comprehensive structural characterisation.

While strong SHG optical rotation has been demonstrated in chemical characterisation applications [61, 62], it has received significantly less attention than the relatively widespread use of SHG-CID. First introduced in 1993 [63], SHG-CID was shown to be 3 orders of magnitude higher contrast than linear optical activity. Even early experiments demonstrated monolayer sensitivity to both chirality and anisotropy when measuring SHG-CID spectra [64], attributed to SHG-CID being an electric dipole allowed effect. Further experiments and theoretical analysis showed that since SHG-CID is electric dipole allowed, it can be much more sensitive to structural chirality than linear techniques, which require magneto-electric cross coupling, often present but not necessarily found in chiral structures [65]. It has, however, also been shown that magneto-electric cross coupling can still contribute to SHG-CID, by measuring SHG circular and linear dichroism in helical aggregates of achiral molecules [66]. In more recent years, nonlinear chiroptical measurements have been combined with spectroscopic and microscopic measurement techniques. Again largely due to extreme symmetry/surface sensitivity, SHG microscopy has significant advantages over linear microscopy in many cases, in particular for cellular and tissue imaging. Samples can be pumped by intense laser light in the IR spectral region, allowing

structural information to be obtained without the need for ultra-violet (UV) illumination. UV wavelengths are required by many fluorescence techniques, but often lead to sample damage due to strong absorption in molecular systems [67]. SHG-CID imaging has thus been used as a high-contrast chirally sensitive method for imaging and obtaining structural information of tissue samples [68, 69], even allowing differentiation between skin tissue with and without disorders [70]. Beyond bio-imaging and chemical characterisation, second-harmonic generation has been used in the chiroptical characterisation of metallic nanomaterials, through both nonlinear microscopy [71, 72, 73] and more direct measurements [74, 75, 8]. Such nanomaterials often lead to further enhancement of nonlinear emission, and are discussed further in section 4.1.2.

3.4 Conclusions

By considering the electromagnetic behaviour of a medium within the electric dipole approximation, we have shown how nonlinear optical measurements, specifically second-harmonic generation, can give robust information about the symmetry of a material. Nonlinear counterparts to the measurable chiroptical effects described in section 2.2 are known to be much more sensitive, and higher contrast, than linear effects, while providing complementary information. This is typically owing to the significantly reduced background from achiral contributions, and the high symmetry-sensitivity of SHG emission. In an isotropic, chiral medium, the intrinsic chirality is described by a single independent susceptibility tensor component. However, the chirality of an anisotropic medium is described by a large number of independent components, entangled with terms associated with anisotropy. Despite this, chiroptical effects originating from structural anisotropy will vary, as the structure is transformed, with different symmetry compared to those originating from intrinsic chirality. Therefore, in anisotropic structures, further consideration of the symmetry of the response can allow the disentangling of chirality from anisotropy. Generally, especially in molecular systems, the nonlinear response of a material is much weaker than the linear response. By fully exploiting the symmetry sensitivity of SHG, this response can be enhanced and utilised in chiroptical characterisation experiments, however in molecular systems this is often not possible. In the following chapter, we will discuss the emergence of plasmonic nanomaterials, which allow unprecedented enhancement of nonlinear emission, chiroptical dissymmetry, and the virtually limitless exploration of structurally-tailored artificial metamaterials.

Chapter 4

Plasmonic Nanomaterials

Recent advances in the fabrication of nano-scale, tailor-designed structures have allowed the exploration of novel optical effects arising from the interaction between light and nanomaterials. Perhaps most commonly exploited are plasmonic materials: metallic structures within a dielectric environment whose optical properties are affected not only by material choice, but also their structural geometry. The general response of a metal surface to incident light can be modelled in terms of plasma oscillations. By treating the metal as a free-electron gas (plasma) surrounding a lattice of positive charges, the electromagnetic response can be described by the motion of this plasma in response to external electromagnetic fields. At a metal-dielectric interface, incident light can drive electron-density waves that propagate along the metal surface. The coupled electromagnetic radiation and electron-density waves are known as surface plasmon polaritons (SPPs), and will propagate along the metal-dielectric interface, with an exponentially decaying intensity normal to the surface.

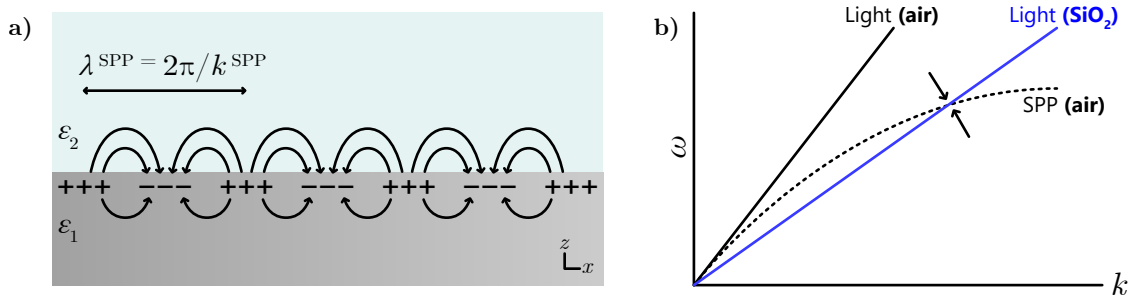

Figure 4.1: ***a)*** *Schematic of a surface plasmon polariton, of wavevector k^{SPP}, at a metal-dielectric interface. Charge density waves form in the metal surface, leading to surface-localised electromagnetic fields at the dielectric interface.* ***b)*** *Representative dispersion curves for surface plasmon polaritons and light at the interface of air and SiO_2. For any particular interface, SPPs cannot be excited by light impinging from the dielectric at that interface. Light propagating through glass can however be phase-matched to a SPP at a metal-air interface, for example. The momentum-matching point is illustrated with arrows.*

We consider an interface between a metal and a dielectric, of permittivities ε_1 and ε_2 respectively (figure 4.1a). The metal necessarily has permittivity $\mathrm{Re}(\varepsilon_1) < 0$. Excitation of SPPs require the real parts of ε_1 and ε_2 to be of opposite sign, that is, the interface is between a conductor and an insulator. In this configuration, the dispersion relation for

a surface plasmon polariton propagating in the x direction, oscillating at frequency ω, is given by equation 4.1 [76, §2.2].

$$k_x^{SPP} = k_0\sqrt{\frac{\varepsilon_1\varepsilon_2}{\varepsilon_1+\varepsilon_2}} = \frac{\omega}{c}\sqrt{\frac{\varepsilon_1\varepsilon_2}{\varepsilon_1+\varepsilon_2}}. \tag{4.1}$$

For light incident on the interface via the dielectric described by ε_2, the optical dispersion relation $k_0 = \omega/c = \omega\sqrt{\mu_0\varepsilon_2}$ shows that the optical momentum in the direction of SPP propagation will always be lower than that of the SPP (figure 4.1b). Conservation of momentum must be considered when optically exciting surface plasmon polaritons, and so SPPs cannot be excited by light incident from the same dielectric as at the metal interface. Various experimental configurations have been demonstrated to allow the excitation of SPPs with optical radiation [76, 77], most commonly the Kretschmann and Otto geometries. These involve exciting a SPP at a metal-dielectric interface with light propagating through a different dielectric, interacting at an adjacent interface. In order for momentum matching to be properly realised, the projection of k_0 onto the axis of SPP propagation must match, and so depends strongly on the angle of optical incidence. Importantly for many applications, this angle is highly sensitive to changes in the dielectric environment. This allows the characterisation molecules attached to the metal surface by scanning the angle of incidence and observing induced shifts, leading to applications in molecular sensing and characterisation [77].

In this work, we make use of plasmonic structure with characteristic dimensions comparable to, or smaller than, the wavelength of light in order to alleviate the momentum matching conditions. In these cases, the surface plasmons are confined to the nanoparticle surface, and are known as localised surface plasmons.

4.1 Localised Surface Plasmons

For small diameter $d \ll \lambda$ metallic nanoparticles, the phase of an oscillating electromagnetic field can be assumed constant over the particle, known as the "quasi-static approximation". In this approximation, the electron gas is driven to coherently oscillate at the particle surface. The lowest-order response of the particle to incident light can thus be described by an induced dipole moment $\tilde{\mathbf{p}}$, much like the simple Lorentz oscillator in section 3.1 (figure 4.2a). For a metallic nanoparticle with an electric polarisability $\tilde{\alpha}$, the induced dipole moment is described by

$$\tilde{\mathbf{p}} = \tilde{\alpha}\tilde{\mathbf{E}}. \tag{4.2}$$

Importantly, the induced dipolar plasmon mode is non-propagating, and so the momentum-matching requirements for exciting propagating surface plasmon polaritons are alleviated. The localised surface plasmon can be coherently excited by any oscillating electromagnetic field, and will reach a maximum excitation efficiency at a particular resonant frequency determined by the effective polarisability $\tilde{\alpha}(\omega)$ of the nanoparticle. This effective polarisability depends strongly on the nanoparticle material, geometry, and the permittivity

of the surrounding medium. Analytical expressions for $\tilde{\alpha}(\omega)$ are well established for simple spherical nanoparticles of radius $a \ll \lambda$ and permittivity $\varepsilon(\omega)$ [76, 7]. For a metallic nanoparticle of permittivity ε_1 surrounded by a dielectric of permittivity ε_2, the polarisability is given by equation 4.3.

$$\tilde{\alpha}(\omega) = 4\pi a^3 \frac{\varepsilon(\omega) - \varepsilon_2(\omega)}{\varepsilon(\omega) + 2\varepsilon_2(\omega)}. \tag{4.3}$$

At the point where $|\varepsilon(\omega)+2\varepsilon_2(\omega)|$ is at its minimum, i.e $\varepsilon(\omega) = -2\varepsilon_2(\omega)$, the polarisability is maximally enhanced, determining the resonant frequency of the localised surface plasmon. However, in many systems the nanoparticle geometry is significantly more complex, and the localised surface plasmon (LSP) resonance cannot be determined analytically. Regardless of the particle geometry however, a particular resonant frequency will exist at which the plasmonic nanoparticle will resonantly scatter. Similar to surface plasmon polaritons, the sensitivity of the resonant frequency to the dielectric environment makes spectral analysis of the plasmonic scattering a sensitive technique for characterising nearby molecules, and has also gained popularity in molecular sensing applications [78, 79, 80].

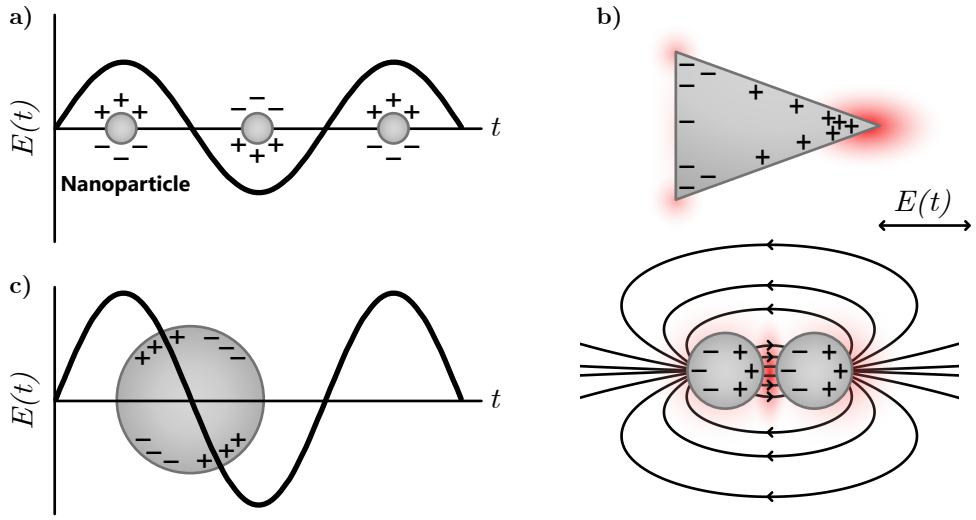

Figure 4.2: ***a)*** *For sub-wavelength metallic nanoparticles, charge is coherently driven at the surface, and the particle can be approximated as an oscillating dipole.* ***b upper)*** *Charge is efficiently confined to the surface of sharp geometric features in conducting structures, resulting in an enhanced electric field intensity around these regions.* ***b lower)*** *A pair of nanoparticles separated by some small distance will couple via the near-field, and function as a single dipole with an additional capacitance from the gap. Charge is efficiently confined to the inner surface, resulting in an enhanced electric field intensity between the two particles.* ***c)*** *For metallic nanoparticles of dimensions comparable to the wavelength of light, charge is driven with a varying phase across the surface, and higher-order plasmon modes are permitted (schematic of a quadrupolar mode is depicted).*

4.1.1 Electromagnetic Field Confinement

An effect crucial to this work, and indeed the field of nanophotonics generally, is the ability for plasmonic nanoparticles to confine electromagnetic fields into sub-wavelength "hotspots". This confinement results in two useful properties: the field is highly localised to small regions of space, allowing targeting of electromagnetic interactions to regions

below the diffraction limit, and correspondingly, the field intensity is enhanced within these regions. The precise mechanism of field confinement depends largely on the system being considered, however perhaps the simplest contribution is from the localised surface plasmon resonance. When a metallic nanoparticle is excited close to a plasmon resonance, the induced dipole oscillates at its maximum amplitude. This results in a resonant scattering of light, leading to locally enhanced electromagnetic fields around the particle. For sub-wavelength nanoparticles, this allows for sub-wavelength field confinement: the localised surface plasmon mode volume is limited by the particle's dimensions, and the local electromagnetic field is determined by the, now tightly confined, surface plasmon oscillation. Coupling this surface plasmon mode to incident light results in an enhanced local electromagnetic field at the particle surface. Like the LSP resonance itself, the enhancement factor (the ratio of the field amplitude at the particle surface, and without the particle present) at resonance strongly depends on the particle material, geometry, and surroundings [81, 82].

Aside from enhanced near-fields at the plasmon resonance, geometric effects can lead to even greater levels of field confinement, with correspondingly high intensity enhancements. Broadly, any effect that confines charge to a region of space within a conductor will lead to enhanced electromagnetic fields at the conductor surface. An important contribution in plasmonic nanostructures can come from the lightning-rod effect. In the context of electrostatics, the lightning-rod effect describes the confinement of electric fields at sharp gradients of conducting structures, such as corners or tapered tips (figure 4.2b, upper). Charge is confined more efficiently to regions of sharp surface gradients on a charged conductor, and so the electric field lines at the surface of the conductor will generally be localised around these sharp features. In spherical nanoparticles, the curvature of the sphere results in charge confinement at the surfaces along the axis of excitation polarisation, resulting in greater field confinement along this direction [82]. However, nanostructure geometries with sharper features greatly increase the field enhancement associated with the lightning-rod effect, localising the field strongly at sharp corners and edges [83, 84, 85].

Another contribution to field enhancement associated with charge confinement is from coupling between plasmonic nanostructures. A simple example is a pair of sub-wavelength nanoparticles, separated by a distance $d \ll \lambda$. This system behaves as a pair of point dipoles interacting via the near-field (figure 4.2b, lower). In the limit of small separation d, the coupled system will radiate as a dipole, and resonantly scatter when excited by light at its resonant frequency. When driven by a field polarised along the chain, the gap between particles introduces a capacitance dependent on particle geometry and separation. This capacitance red-shifts the resonant frequency of the longitudinal hybridised plasmon mode along that axis. When driven by light polarised perpendicular to the chain, a transverse hybridised plasmon mode is excited, with lower inter-particle capacitance, blue-shifting the resonant frequency. Crucially, the capacitance of the inter-particle gap results in the confinement of charge on the inner surfaces of the particles. The confinement of charge directly leads to confinement of the electromagnetic fields in the region between particles. Both the inter-particle field confinement, and associated shifts in the LSP resonance have been studied experimentally and theoretically for long chains of nanoparticles [86, 87],

pairs of nanoparticles [88], and periodic nanostructure arrays [89, 90, 72].

The ability to strongly confine electromagnetic fields has found a wide range of applications, of particular note in surface-enhanced Raman scattering (SERS) [91, 78]. Raman scattering experiments typically probe molecular transitions by spectroscopically analysing light inelastically scattered from a molecule. Spectral shifts in the scattered light correspond to the energy of molecular transitions, acting as a probe for substance composition. However, the probability of inelastic scattering is low compared to elastic scattering, and thus Raman scattering is typically a very weak effect. In SERS experiments, molecular samples are bound close to a nanostructured metal surface. Incident light resonantly excites surface plasmons in the metallic structures, leading to an enhanced near-field at the metal surface. The enhanced near-field scatters from the molecular sample, and the plasmonic nanostructures can then function as resonant transmitting antennae for the scattered light, providing a second source of enhancement. The combination of these two sources of enhancement lead to a potential enhancement in the overall detected Raman scattering signal of 10^{10} [92]. Although the precise limitations of SERS are debated [93], enhancements of several orders of magnitude have nevertheless been experimentally demonstrated using coupled spherical nanoparticles [94], bowtie antennae (making use of the lightning-rod enhancement) [92], and roughened metal surface, showing sensitivity down to single-molecule detection [95]. Plasmonic field confinement has also found applications in sub-wavelength imaging [96], photodetection [97], and scanning near-field optical microscopy (SNOM) [98] by making use of sub-wavelength resonant antennae.

4.1.2 Enhanced Second-Harmonic Generation

In section 3 we established that the amplitude of second-harmonic generation varies with E^2, and correspondingly the SHG intensity follows E^4, where E is the amplitude of incident light. This sensitivity to the driving field amplitude allows SHG to be greatly enhanced in regions of strong local fields, such as plasmonically confined hotspots. The requirement for inversion asymmetry generally prevents SHG from the bulk of metallic structures. However, the metallic surface interface breaks centrosymmetry allowing surface SHG. Surface plasmons then confine the incident light to the nanoparticle surface, increasing the surface SHG intensity. The first experimental demonstration of SHG enhancement from surface plasmons reported a $30\times$ increase in SHG intensity [99]. Since then, orders of magnitude SHG enhancement have been demonstrated from a range of nanoparticle geometries including coupled nanoparticles [100], individual particles within plasmonic cavities [101], periodic nanostructure arrays [90], and metallic nanoshells [102]. Enhanced SHG has also been deployed as an experimental probe for measuring confined fields between a plasmonic nanoparticle and metallic surface, with applications in sub-wavelength spatial measurements [103].

Importantly, plasmon enhanced SHG has been applied to molecular sensing platforms. As discussed in section 3.3, second-harmonic generation has long been used in chemical characterisation [104], molecular sensing [105], and disease diagnosis [67] owing to its symmetry sensitivity, both providing structural information [106] and reducing back-

ground signal from SHG-forbidding structures [107]. However, second-harmonic signals from small quantities of molecules tend to be weak. By making use of both the intensity enhancement [108, 109] and sensitivity to changes in the nanostructures surrounding medium [110], plasmonic nanomaterials have provided a platform to greatly improve the sensitivity of sensing techniques. Similarly, we discussed in section 3.3 the use of second-harmonic generation as an ideal probe for structural chirality, due to the intrinsic lack of centrosymmetry of chiral structure. It has been shown that, in large part due to the enhancement in SHG intensity from local-field confinement, plasmonic nanomaterials can lead to increased sensitivity of nonlinear optical activity measurements [72, 111, 71].

4.1.3 Enhanced Chiral-Optical Interactions

It is known that plasmonic nanomaterials are able to enhance chiroptical effects. While no single mechanism for this is common between all demonstrations, field confinement is often a primary contribution, as the optical field can be more tightly confined to the dimensions of, for example, individual molecules, increasing the fraction of incident light that interacts with the molecule. However, plasmonic nanomaterials offer an additional unique advantage: the freedom of fabrication techniques allows almost limitless exploration of structural symmetries, directly opening up greater possibility for optimising the chiroptical properties through tuning structural geometry. Aside from more common lithographic techniques, many novel fabrication methods have been proposed for the development of chiral metallic nanoparticles, including shadow deposition techniques for complex structures [112], and techniques based on molecular scaffolding. For example DNA, whose helical structure is an archetypal example of chirality in nature, can be used as a scaffold to helically-arrange metallic nanoparticles into chiral clusters [113]. Similar methods, of using chiral molecules to arrange achiral nanoparticles, have been demonstrated and experimentally shown to exhibit significantly enhanced optical activity [114, 115, 116]. This sensitivity has previously allowed the attomolar detection of DNA, by making use of DNA-linked achiral gold nanorods [117].

Even without exhibiting structural chirality, it has been shown that plasmonic nanoparticles can lead to enhanced detection of chiroptical effects. For example, achiral nanostructures can be designed such that the plasmon resonance matches with a molecular transition. The enhanced local fields at resonance allow for enhanced optical interaction with the molecule. This principle has been demonstrated to enhance the molecular absorption by up to 5 orders of magnitude, for applications in extremely low concentration molecular detection [80]. In cases where the plasmon resonance is away from any molecular resonance, chirality can still be "transferred" from molecules to nearby plasmonic nanostructures. Enhanced circular dichroism has been observed from chiral molecules in the gaps of nanoparticle chains, close to the plasmon resonance [118, 119, 120], demonstrating the transfer of chirality from the molecule to the resonating localised surface plasmon. A similar effect has also been observed for molecules near the surface of planar nanostructures on dielectric substrates, showing the transfer of chirality from monolayers of molecules to individual, unchained nanoparticles. This transfer of chirality led to a measurable cir-

cular dichroism unobserved in the absence of plasmonic nanostructures [121]. Notably, aside from enhancements originating from coupling of chiral particles to intense localised field hotspots, plasmonic nanomaterials have been demonstrated to exhibit chiroptical enhancement due to the formation of superchiral local fields.

4.1.3.1 Superchiral Fields from Plasmonic Nanostructures

As discussed in section 2.3, "superchiral" regions of electromagnetic fields, in which the optical chirality exceeds that of circularly polarised light, can be used to significantly enhance the dissymmetry of chiroptical interactions with molecules in these regions. We discussed the use of standing waves, and Bloch waves, to form static regions of high optical chirality, which can be used in molecular detection applications. Another route however is the use of plasmonic nanostructure surfaces to form local regions of superchiral light in the nanostructure's near field. Previous work has shown that plasmonic nanostructures can be used to enhance chiral dissymmetry by $\approx 10^6\times$, with this enhancement being attributed to the presence of superchiral fields [122]. By examining the influence of the presence of proteins on the CD spectra of a chiral plasmonic nanomaterial, it was shown that superchiral sensing regimes allow both the sensitive detection, and the structural analysis, of chiral materials [122]. This led to the theoretical investigation of the superchiral near fields generated from a range of both planar and 3-dimensional chiral plasmonic nanostructures [123]. It has also since been shown that the optical chirality at the surface of nanostructures can be tuned by changing relatively simple geometric properties such as the thickness of a plasmonic nanostructure surface [124]. These surfaces were later used to demonstrate "superchiral polarimetry", measuring the optical rotatory dispersion of the surface in the presence of proteins, which shift the plasmon resonance depending on the protein structure. This shift depends on the handedness of the underlying metasurface, and so is measured as an enhanced chiral asymmetry in the ORD spectra, providing comprehensive structural information [125]. Novel fabrication techniques have also been demonstrated to allow ultra-broadband generation of superchiral fields from chiral plasmonic nanostructures, exhibiting both large circular dichroism and optical rotation at optical wavelengths [20]. Interestingly, it has also been shown that in achiral plasmonic nanostructures pumped with linearly polarised light, although the optical chirality of the near field integrated over all space is 0, regions within the nanostructure's near-field volume exhibit can still high optical chirality [126, 127]. It has been proposed that by masking regions of the structure exhibiting one handedness of optical chirality, a non-zero macroscopic chiroptical response can be obtained within this regime [126]. Crucially to this work, superchiral fields have also been shown to contribute to enhanced second-harmonic optical activity. Both SHG and optical activity have components proportional to electric field gradients, and so regions of high optical chirality are expected to directly enhance SHG, and corresponding nonlinear chiroptical effects [128].

4.2 Metamaterials

By fabricating arrays of sub-wavelength plasmonic nanostructures, it is possible to create artificial "metamaterials". In arrays of nanoparticles supporting localised surface plasmons, the system can be modelled as an array of oscillators with effective polarisabilities. The macroscopic behaviour of the array can then be described as an effective medium, with a susceptibility describing its optical response as in section 3.2. Now, the macroscopic optical properties of the metamaterial are strongly related to the geometry of the individual nanoparticle inclusions, offering unprecedented flexibility to design materials exhibiting optical properties never observed in nature. An often cited example of this is the possibility of a perfect optical lens formed from a metamaterial with negative refractive index, as proposed by Veselago [129], and later expanded on by Pendry [130]. Further work has proposed the use of metamaterials for photonic devices such as perfect reflectors [131], polarisation optics [132], and chiral-optical devices, as discussed in section 4.1.3.

Of particular interest in this work are meta-*surfaces*. These consist of plasmonic nanostructures patterned onto the surface of a dielectric substrate creating a quasi-2-dimensional metamaterial. Whereas 3D metamaterials typically exhibit novel optical properties from light propagating through the bulk, 2D metamaterials act to manipulate the wavefront of incident fields at the surface [133]. This has potential applications in new ultra-thin optical components. Since traditional optics generally rely on small effects building up throughout propagation through the material, they are generally much thicker than a metasurface designed to exhibit the same total effect on the wavefront [134, §3]. Additionally, they are ideal for studying plasmon enhanced SHG, since the primary contribution to SHG comes from the material surface anyway, with little to no bulk contribution.

By treating a plasmonic nanostructure array as an effective medium, a macroscopic description of the optical response can be employed, as in chapters 2 and 3. This allows the nanomaterial to be characterised by macroscopic parameters such as effective susceptibility, refractive index, and structural chirality. These can be quantified by measuring macroscopic effects such as circular dichroism and optical rotation of reflected light, or nonlinear chiroptical counterparts SHG-CID and SHG-OR. The work in chapters 6 and 7 in particular treat our nanostructure samples as an effective medium, with macroscopic properties.

4.3 Beyond the Quasi-Static Approximation

So far we have discussed two extreme cases of surface plasmons: propagating surface plasmon polaritons along an effectively infinitely large plane of metal, and localised surface plasmons coherently driven on the surface of an effectively infinitesimally small metallic particle. However, as discussed further in section 5, and considered in previous works [90, 128], it is important to consider the intermediate regime of nanostructures of dimensions comparable to the wavelength of light. In these cases, the quasi-static approximation breaks down since the phase of the driving field will vary over the geometric span of the structure, and so excited surface plasmons will in turn oscillate with a spatially

varying phase. For small nanoparticles, localised surface plasmons can be considered the lowest-order, dipolar charge density mode (figure 4.2a). The plasmonic behaviour in the intermediate regime can be understood in terms of *higher-order* charge density modes. Importantly , these higher-order modes are still non-propagating, and have zero net momentum. Thus, even in this intermediate regime, momentum matching is not a requirement to excite higher-order localised surface plasmons. Figure 4.2c shows a schematic representation of this effect: a metallic particle is driven by light such that there is a $\approx \pi$ phase shift across the span of the particle, resulting in a quadrupolar plasmon mode. In real structures, many higher-order plasmon modes can be excited, and for structures more geometrically complex than simple ideal spheres, these modes have significantly more complex spatial wavefunctions. Previous work demonstrated that the plasmonic response of metallic nanostructures in this intermediate regime can be decomposed into a set of current density eigenmodes [135]. This work was later extended to arrangements of coupled nanostructures [136]. The optical response can be further understood by applying group theory to the plasmonic eigenmode set [137], allowing the current density modes to be grouped by the optical polarisation states that exclusively excite them. The work in chapter 5 considers nanostructures within this intermediate regime, where a full modal analysis must be employed to properly describe the optical properties of the nanostructure surface.

4.4 Conclusions

By modelling the optical response of a metal as an electron plasma surrounding a lattice of positive charge, we have shown that metallic nanoparticles significantly smaller than the wavelength of light will behave as an oscillating electric dipole. This coherently driven electron oscillation is known as a localised surface plasmon (LSP). The restoring force on the LSP, and hence resonant frequency of the dipole oscillation, will depend not only on the nanoparticle material, but also the geometry of the nanoparticle itself. This allows the optical properties of nanoparticles to be tailored by changing only the dimensions and shape of the particle. Additionally, the surrounding medium will affect the resonant properties of the LSP, and so LSP resonances can be used for the sensitive characterisation of media surrounding, or attached to the surface of, metallic nanoparticles. This surface sensitivity is further enhanced by the remarkable ability for plasmonic nanoparticles to locally confine electromagnetic fields. Three key contributions to field confinement are discussed. When driven at resonance, the plasmonic nanoparticle will resonantly scatter light, increasing the electromagnetic intensity surrounding the nanoparticle. Additionally, nanoparticles with sharp geometric features will confine charge in these regions. This charge confinement directly leads to the confinement of electric fields at the surface, analogous to the lightning rod effect in electrostatics. Finally, charge confinement is also induced when multiple nanoparticles are coupled via the near-field. When a pair of plasmonic nanoparticles are separated by a dielectric medium, the capacitance of the gap confines charge at the inner surface, leading to strong field confinement in the space between the nanoparticles, and a shift in the LSP resonance. Crucially to this work, these confined electromagnetic

fields have been shown to enhance both chiroptical interactions with structures surrounding the confined fields, and nonlinear emission due to the strong intensity dependence of higher-order nonlinearity. By fabricating periodic arrays of sub-wavelength nanostructures, artificial metamaterials can be developed. Since the structure can be modelled as an array of coupled electric dipoles, it can be macroscopically described as an effective medium. The macroscopic optical properties will strongly depend on the nanostructure geometry, material, and surroundings, allowing for plasmonic enhancements to be utilised on a macroscopic scale. The unique ability to design metamaterials of arbitrary geometry allowed the study of chiroptical effects as a sample transitions from one handedness to the other (section 5), of isolating the structural chirality of a highly anisotropic metamaterial (section 6), and finally the first demonstration of optical activity in hyper-Rayleigh scattering, using chiral nanoparticles isotropically suspended in solution (section 7). In these chapters, the enhancement of second-harmonic generation from local-field enhancement, chiroptical interactions from plasmonically enhanced chiral near-fields, and the combined enhancement available from nonlinear chiroptical measurements, have all been used to develop new experimental techniques for the detection and characterisation of chiral metamaterials.

Chapter 5

Enantiomorphing Chiral Nanostructures

Sections of this chapter have been copied verbatim from the (published) manuscript *"Enantiomorphing Chiral Plasmonic Nanostructures: A Counterintuitive Sign Reversal of the Nonlinear Circular Dichroism"*, Joel T. Collins et. al. [6]. Experiments were planned by V. K. Valev. Samples were prepared by N. V. S. Braz and P. A. Warburton. SHG microscopy experiments were executed by V. K. Valev, E. Slenders and M. Ameloot. Linear scattering spectra were obtained by myself and C. Kuppe, and analysed by myself. Near-field and scattering simulations were performed by X. Zheng, G. A. E. Vandenbosch, and V. Moshchalkov. Numerical simulations of the linear far-field reflection CID were performed by S. Zu and Z. Fang. Analysis of the nonlinear microscopy data was performed by myself, with Python code including sections written by V. K. Valev. The formulation and analysis of modal circular-dichroism based on the near-field simulations was also performed by myself. I produced the manuscript draft on which this chapter is based.

In section 4.1 we discussed the formation of electric field "hotspots" at the surface of plasmonic nanomaterials, which can enhance both second-harmonic generation, and chiroptical interactions. These hotspots depend strongly on the optical wavelength and nanostructure geometry. Properly understanding the properties of these chiral hotspots is crucial for their applications, for instance enhancing the optical interactions with chiral molecules. Here, by designing 35 intermediate geometries, a plasmonic nanostructure array is "enantiomorphed" from one handedness to the other, passing through an achiral geometry. Nonlinear multiphoton microscopy is used to demonstrate a new kind of double-bisignate circular dichroism due to enantiomorphing, rather than wavelength change. From group theory, a fundamental origin of this plasmonic chiroptical response is then proposed.

5.1 Introduction

Historically, chirality has been primarily associated with stereochemistry. However, while chirality can be crucial for understanding molecules, molecules are not best suited for

understanding chirality. Ideally, we would like to be able to vary the chirality of a particular structure, i.e., to follow the chiroptical response as chiral systems transition from one form into another. While some geometric parameters of molecular systems can be varied to study chirality [138], it is not possible to *freely* control arbitrary geometric properties of molecules. Modern nanofabrication techniques have gone some way to lifting this limitation. Using modern nanofabrication, it is possible to explore a more complete evolution of chiral forms, by preparing sets of intermediate geometries. This opens the possibility to tune and optimise the chirality parameters. For instance, by maximising the geometric chirality parameter, it is possible to achieve negative refractive index materials with applications in super-lenses [139], as well as various applications that depend on the control of circularly polarised light (CPL). Moreover, by optimising optical chirality (section 2.3), "superchiral" light configurations can be achieved. Importantly, optical chirality is particularly enhanced at the surface of chiral plasmonic nanostructures (section 4.1.3.1), resulting in large enhancements in measurable circular dichroism (CD).

Despite the advantages of creating intermediate geometries, it is rare to find studies where these have been investigated in detail. Between two enantiomorphs, there can be several pathways for intermediate geometries, illustrated in figure 5.1a. Also, *a priori*, it is not clear what the best number of intermediate geometries should be. This is highly dependent on the geometric and material properties of the structures, as well as on the wavelength ranges used. In literature, examples can be found of studying both enantiomorphs of a structure, its achiral variant, and a small number of intermediate steps only [140]. Consequently, important and interesting behaviour can go unnoticed.

Here, we developed an experiment impossible to perform with chiral molecules: by designing 35 intermediate geometries, we can "enantiomorph" plasmonic nanostructures from one handedness to the other, passing through an achiral geometry. We demonstrate a bisignate (of two signs) circular intensity difference (CID) due to enantiomorphing, rather than wavelength change, in the nonlinear emission from near-field hotspots. Contrary to what would be expected from pure geometric considerations, the nonlinear chiroptical signal is double-bisignate. A full modal analysis of the structures is combined with group theory in order to understand this result.

We find that, regardless of their handedness, chiral nanostructures support plasmon modes that can be excited by both left and right circularly polarised (LCP and RCP) light. Furthermore, which modes are dominant (i.e., couple strongest to light) depends on the wavelength or the shape/dimensions of the nanostructure. Therefore, it is possible to engineer chiral nanomaterials that, at a given wavelength, can only be excited with the "wrong" direction of CPL. This allows the possibility of tuning a structures' chiroptical response by selecting particular electromagnetic modes, or sets of modes, among hundreds supported, which can enable more sensitive chiroptical control than what is currently available.

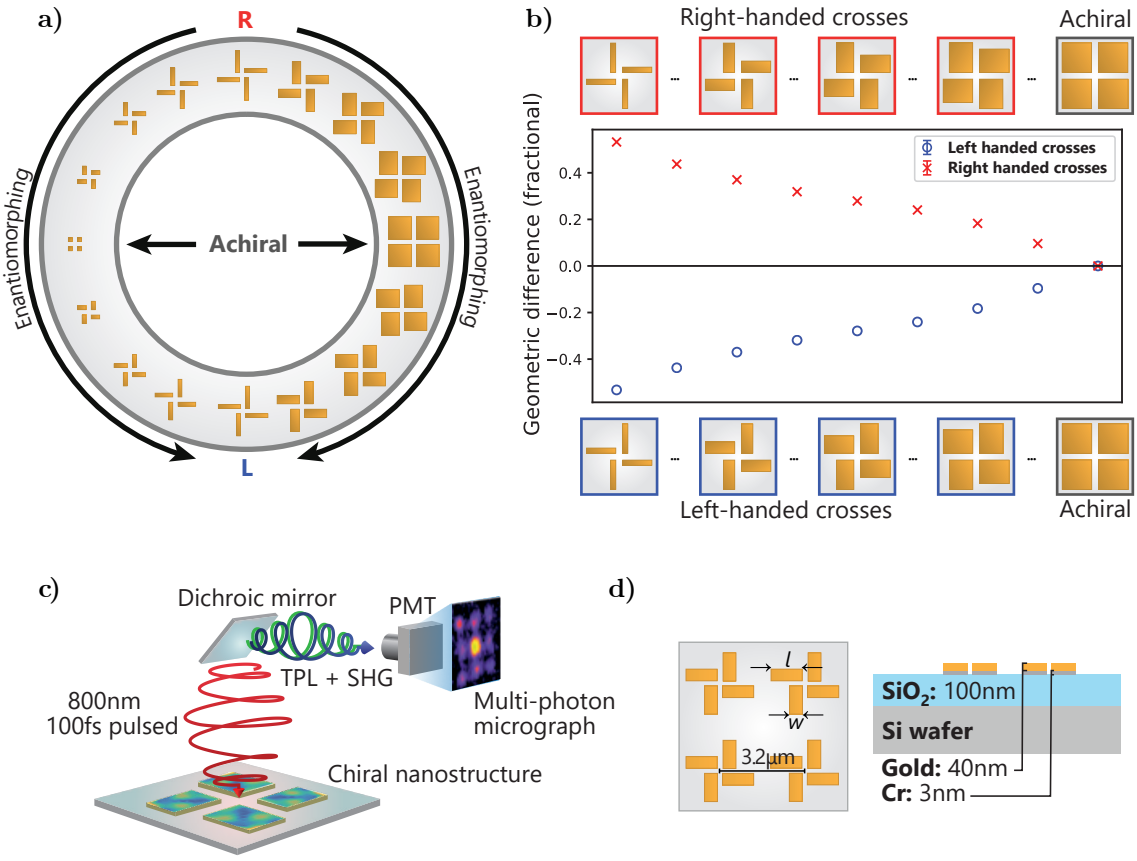

Figure 5.1: ***a)*** *Representation of two possible pathways to enantiomorph a right-handed structure (R) into a left-handed structure (L), through an achiral geometry. Here, we examine the pathway on the right side of the circle.* ***b)*** *As the left-handed chiral crosses change into achiral square structures and into right-handed chiral crosses, the chiral geometric difference diminishes until it reaches 0 in the achiral case and then reverse its value.* ***c)*** *Schematic diagram of the multiphoton microscopy experiments.* ***d)*** *Geometry and depth profile of the chiral crosses samples.*

5.2 Results

Initially, it is useful to consider the geometric chirality of the nanostructure. From here on, we will refer to the crosses as either left- or right-handed, following the convention shown in figure 5.1b. Starting with left-handed crosses, their geometry is morphed in discrete steps, first into achiral squares and then into right-handed chiral crosses (figure 5.1b). For the purposes of comparison, a measure of "chiral geometric difference" describes the area of maximal overlap that can be achieved between left- and right-handed structures, by rotating and translating the two mirror-image shapes, relative to each other (Appendix C.1). As figure 5.1b shows, the chiral geometric difference diminishes until it reaches 0, in the achiral case. This trend is intuitively expected for an enantiomorphing transition, and even matches previously reported optical experiments [138]. However, generally the chiroptical properties of nanostructures depend on more than geometry alone. Without considering material effects, and the properties of the incident light, no direct connection can be assumed between chiral geometric difference and chiroptical effects. This measure of chirality contrasts the double-bisignate response found in the following nonlinear CID measurements.

For these experiments, we made use of a commercial multiphoton microscope with circularly polarised illumination at 800 nm, depicted schematically in figure 5.1c. Note that "dichroic" in the context of a dichroic mirror means different reflectivities at different wavelengths, here used to prevent reflected light at 800 nm from being collected. The collected light consisted mostly of the second-harmonic generation (SHG). Specifically, a bandpass filter allowing 390 nm to 465 nm light was used and, although this filter passes a small part of two-photon luminescence signal, the SHG signal is clearly dominant in this spectral range. Since these nonlinear optical processes are enhanced in the regions of strong local field (chapter 3), they act as a sensitive far-field probe for local-field effects.

The samples are chiral crosses made of Au, deposited by electron beam lithography (EBL) on a Si substrate with a thermal oxide layer, and whose dimensions and depth profile are given in figure 5.1d. Each cross is composed of four separate nanostripes, with varying width w and length l. The separation distance between nanostripes, at the centre of the crosses, is constant at 200 nm. The crosses are arranged in a 40 µm × 40 µm square array, with the distance between cross centres also kept constant at 3.2 µm.

Figure 5.2a shows scanning electron microscopy (SEM) images of sample arrays. In these arrays, the length of the nanostripes is fixed (1000 nm) and the width changes from 200 nm to 1000 nm in steps of 200 nm. Below each SEM are two corresponding multi-photon micrographs, obtained with LCP and RCP. The multi-photon microscopy images are colour coded for intensity, and show bright hotspots at the centre of the chiral crosses (indicated with dashed-line squares for clarity). Similar hotspots have previously been observed at the centre of G-shaped [141] and S-shaped [128] nanostructured arrays. The hotspots correspond to a chiral coupling at the centre of the unit cells that depends on the chirality of the nanostructures and the direction of CPL [128, 63, 61]. This dependence is expressed as a directly observable nonlinear circular intensity difference. Interestingly though, in this set of samples, the nonlinear CID changes sign between the chiral crosses with nanostripe width 200 nm and 600 nm, even though the structures have the same handedness.

The nonlinear CID reversal can be seen more quantitatively in figure 5.2b. Here, the nonlinear CID is obtained from the detected light upon LCP or RCP illumination according to $(I^{MP}_{RCP} - I^{MP}_{LCP})/(I^{MP}_{RCP} + I^{MP}_{LCP})$. The individual multi-photon intensity terms I^{MP}_{RCP} and I^{MP}_{LCP} were obtained from the pixel intensity at the centre of the chiral crosses, where the chiral coupling is maximum and the characteristic response is most pronounced. The nonlinear microscopy images obtained contain roughly 60 crosses of each type (left- and right-handed), with separate images for LCP and RCP illumination. A Python script was used to specify the central regions of 25 crosses, with clearly damaged structured avoided. For each cross, a 5-pixel by 5-pixel square at the defined central region was intensity-averaged (pixel array at 0.09 µm per pixel). This result was itself then averaged over 25 crosses to obtain a final intensity and statistical uncertainty for a particular orientation of cross (left- or right-handed) and input polarisation (LCP or RCP). This was done for each of the considered geometries. It should be noted that the SEM pictures in figure 5.2a are only a subset of the samples we studied. The full set started from $w = 100$ nm and progressed to $w = 1000$ nm, in steps of 50 nm. Upon considering the nonlinear CID from

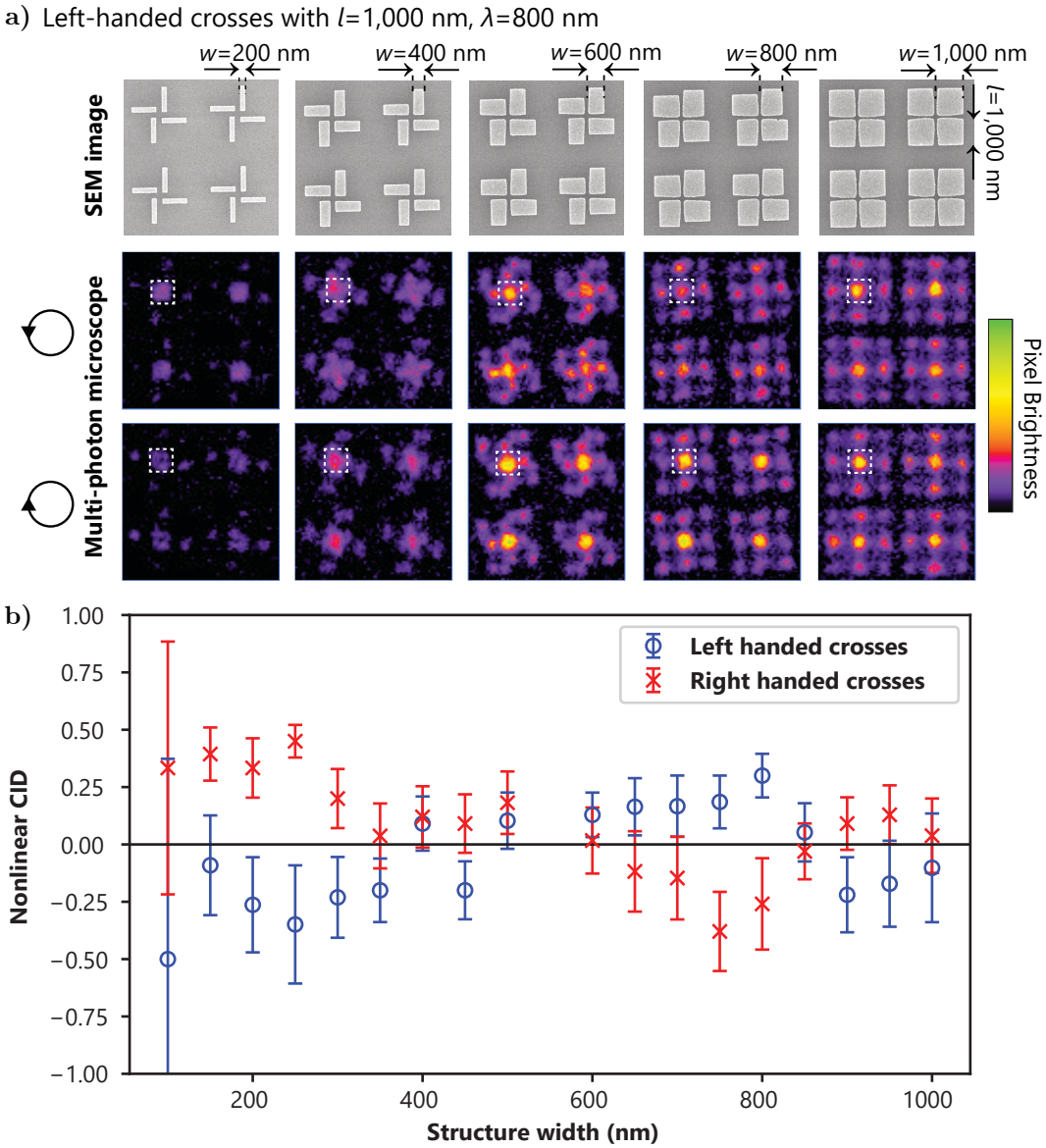

Figure 5.2: *Varying arm width of the nanostructure features at fixed l=1000nm. SEM images of 4 structure cells for each geometry* ***(a top)****, and SHG microscopy images* ***(a, lower)*** *under illumination from left (counter-clockwise arrow) and right (clockwise arrow) circularly polarised light, at* 800 nm *wavelength. Scale (right) corresponds to image pixel brightness.* ***b)*** *Measured total nonlinear CID under* 800 nm *wavelength light is then calculated for each geometry. Our experiments reveal a counter-intuitive behaviour for the second-harmonic generation circular intensity difference (SHG-CID) – both the 0 value and the reversal occur before reaching the achiral geometry.*

all these samples, it is observed that between $w = 200\,\text{nm}$ and $w = 800\,\text{nm}$, the chiroptical response is unambiguously reversed, i.e. with clearly separated error bars. The nonlinear CID that we measured is collected in the far-field (well away from the structure surface), and it is very different from the *linear* circular dichroism in the far-field.

The linear far-field CID response is demonstrated by FDTD simulations data, shown in figure 5.3. Additional linear scattering spectra simulations and experimental data are given in Appendix C.2. The data in figure 5.3 differ significantly from those in figure 5.2b. A key reason for this difference is that the nonlinear CID originates in the near-field, strongly depending on the field intensity at the surface of the structure. To understand the

observed reversal of the nonlinear CID, we need to examine the electromagnetic behaviour at the surface of the nanostructures.

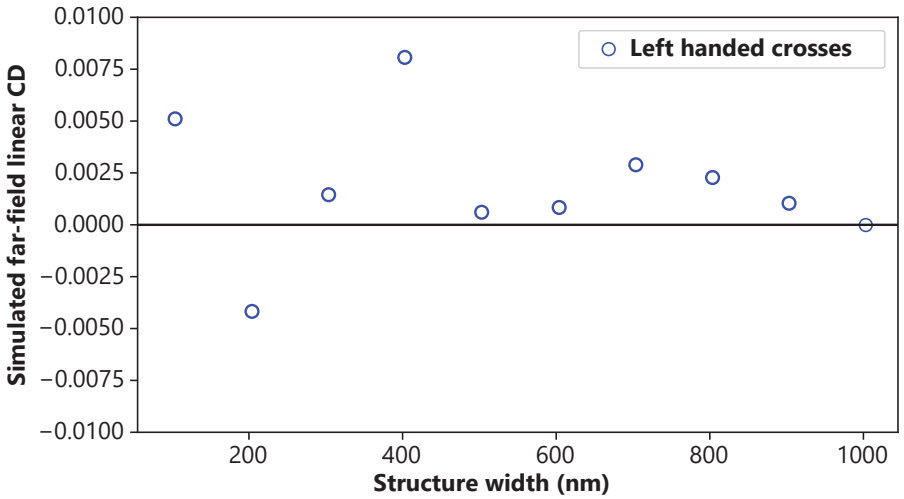

Figure 5.3: *Simulated far-field linear reflection CD for left-handed chiral cross structures. The lineshape of the linear CD response is significantly different to that obtained from nonlinear CID measurements.*

5.3 Discussion

For each nanostructure examined, the induced current flowing in the structure due to an incident field was obtained by X. Zheng and G. A. E. Vandenbosch using the methods detailed in references [6, 135]. For a given structure, the full induced current solution $\mathbf{J}$ is characterised by a set of modes $\mathbf{J_n}$ and corresponding eigenvalues λ_n. Each structure is associated with a different set of modes, and the amplitudes of each mode describe their coupling strengths to a particular incident field. These methods are well established, but here the analysis was taken further by making use of group theory. Each available mode associated with a given structure geometry can be placed in one of four orthogonal irreducible representations $\Gamma_{j=1,2,3,4}$. These representations correspond to exclusive excitation with either the two orthogonal linear polarisations (Γ_1 for horizontal and Γ_2 for vertical) or the two circular polarisations (Γ_3 for LCP and Γ_4 for RCP). Importantly, each mode in the 3rd irreducible representation has a "correlated" mode in the 4th irreducible representation, with identical eigenvalues forming an "accidentally degenerate pair". Crucially, the LCP coupling coefficient of a given Γ_3 mode may be different from the RCP coupling coefficient of the correlated Γ_4 mode. This difference in a mode pair's ability to couple to LCP and RCP incident light can be seen as a type of modal CID, and is shown in figure 5.4a, b.

Figure 5.4a shows pairs of correlated modes in the structures with width 200 nm. In blue, the Γ_3 modes are ranked according to their coupling coefficient to LCP. The correlated Γ_4 modes, which only couple to RCP, are shown in red. In an achiral structure, both the blue and red sets would have identical values and ranking. Not surprisingly, the presence of chirality in the structure breaks the symmetry and, overall, the blue modes

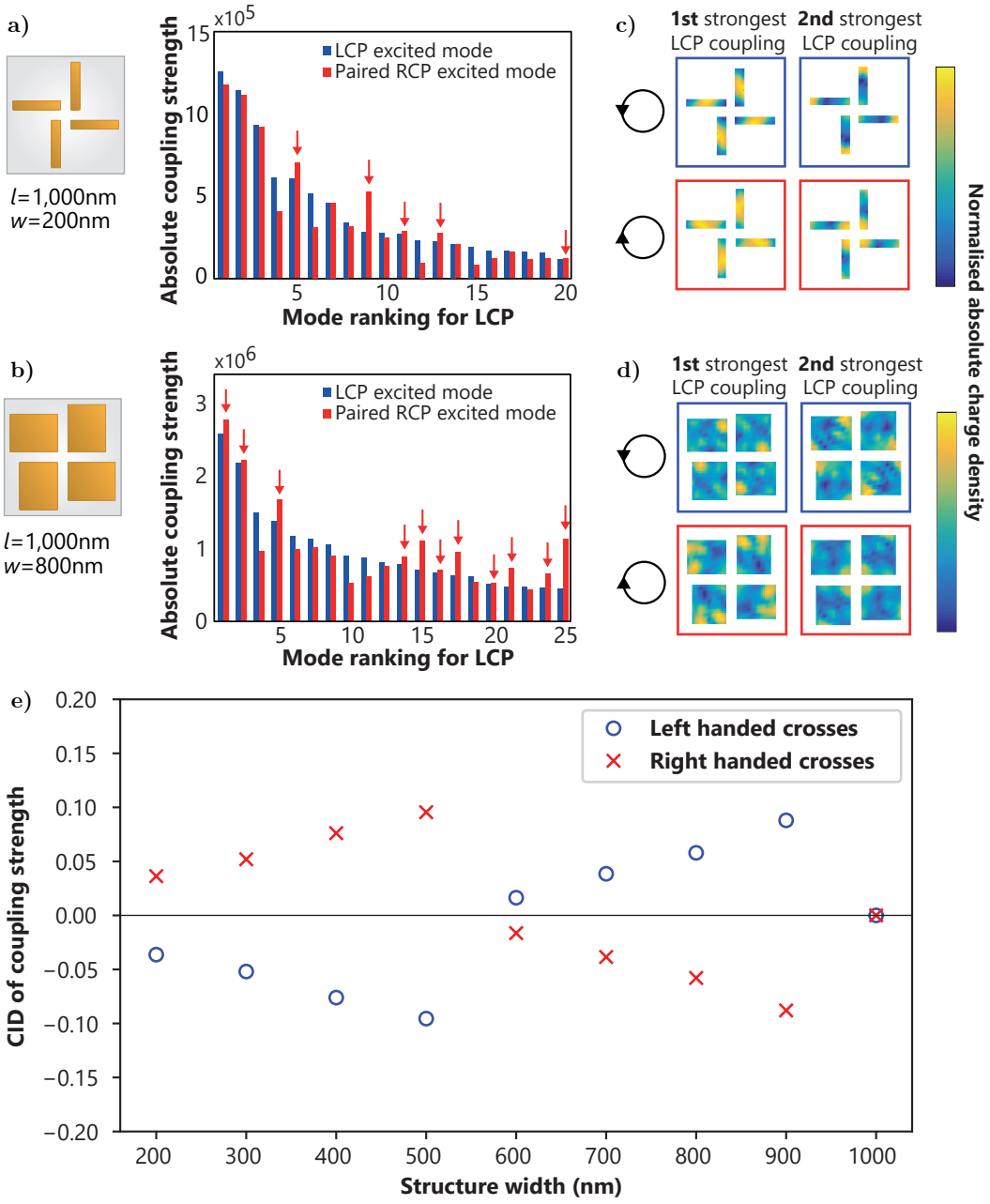

Figure 5.4: ***a-e****. Simulation results showing modal composition of chiroptical response. Modal analysis of structures with arm length 1000nm, width 200nm* ***(a)*** *and 800nm* ***(b)****. The most LCP-dominant modes for each structure are plotted showing both LCP coupling strength (blue) and the correlated-mode RCP coupling strength (red). Modes coupling stronger to RCP than LCP are marked with arrows. Examples of individual modes (normalised absolute charge density) are shown for width* 200 nm ***(c)*** *and 800nm* ***(d)****. The total coupling strength CID as defined in equation 5.4 is plotted for varying arm width, at fixed* $l = 1000$ nm *under* 800 nm *wavelength light* ***(e)****.*

have higher coupling coefficients. But counter-intuitively, we also find that, in some pairs, the red modes have higher coupling coefficients. This means that, for such modes, light of the "wrong chirality" couples more efficiently to the chirality of the nanostructure. An example of this behaviour is indicated with an arrow on the figure. As we will see next, the exception can become the rule as we continue changing the cross width towards an achiral structure.

Figure 5.4b shows pairs of correlated modes in the structures with width 800 nm. Here, there are more red-dominant pairs of correlated modes than in figure 5.4a, to the point that the overall calculated near-field CID is reversed, as in the experimental observation. Therefore, in these plasmonic nanostructures, the chiroptical response originates from the superposition of all the individual modal responses. The modes themselves represent complex spatial distributions of the charge density; as an illustration, the first and second modes from figure 5.4a and 5.4b are shown in figure 5.4c and 5.4d, respectively. Since the near-field intensity is directly related to the total charge density, regions of high charge density will result in SHG hotspots (via local fields) on the structure surface. Therefore, differences in the coupling of charge density modes to LCP and RCP light are directly responsible for the observed SHG-CID.

Mathematically, the overall near-field CID originates from the full solution $\mathbf{J}$ obtained by linearly superposing the contributions from all eigenmodes $\mathbf{J_n}$ [142],

$$\mathbf{J}(\mathbf{r},\omega) = \sum_n c_n(\omega)\mathbf{J_n}(\mathbf{r},\omega). \tag{5.1}$$

Here, $\mathbf{J}$ represents the current flowing at an observation point $\mathbf{r}$ in the nanostructure induced by an incident field $\mathbf{E}(\mathbf{r},\omega)$ oscillating at a frequency ω. For a given incident field, the coupling coefficients c_n are given by [137, 142]

$$c_n(\omega) = \frac{\int_V \mathbf{J}(\mathbf{r},\omega)\cdot\mathbf{E}(\mathbf{r},\omega)d\mathbf{r}}{\lambda_n(\omega)} \tag{5.2}$$

and the volume integration $\int_V$ is carried out over the whole nanostructure [136]. To calculate an overall near-field CID, we make use of the inner product of the coupling coefficients given by

$$\|c_n(\omega)\| = \langle c_n(\omega), c_n(\omega)\rangle = \sum_n c_n(\omega)c_n^*(\omega) \tag{5.3}$$

Here, c_n^* denotes the complex conjugate of c_n. Since the local-field intensity is dependent on the square of all coupling coefficients, the local-field circular-dichroism can be expressed as

$$\mathrm{CID}^{(Local)} \propto \frac{\left\|{c_n}^R(\omega)\right\|^2 - \left\|{c_n}^L(\omega)\right\|^2}{\left\|{c_n}^R(\omega)\right\|^2 + \left\|{c_n}^L(\omega)\right\|^2}. \tag{5.4}$$

The L and R superscripts refer to the solutions for LCP and RCP respectively. The results from equation 5.4 can be found in figure 5.4e, where the calculated near-field CID is plotted as a function of the nanostripe width (w), for the left-handed and right-handed crosses. These numerical results show a bisignate near-field CID response corresponding well to the experimental nonlinear CID curves in figure 5.2b. While figure 5.2a reveals slight deformation towards the centre of the measured crosses, for large (> 400 nm) cross widths, the effect of this deformation on the SHG-CID is minor (see reference [128]). The bisignate trend seen in Figure 5.4e is in good agreement with the experimental data found in figure 5.2b.

This agreement was further verified with a second set of intermediate structures (fig-

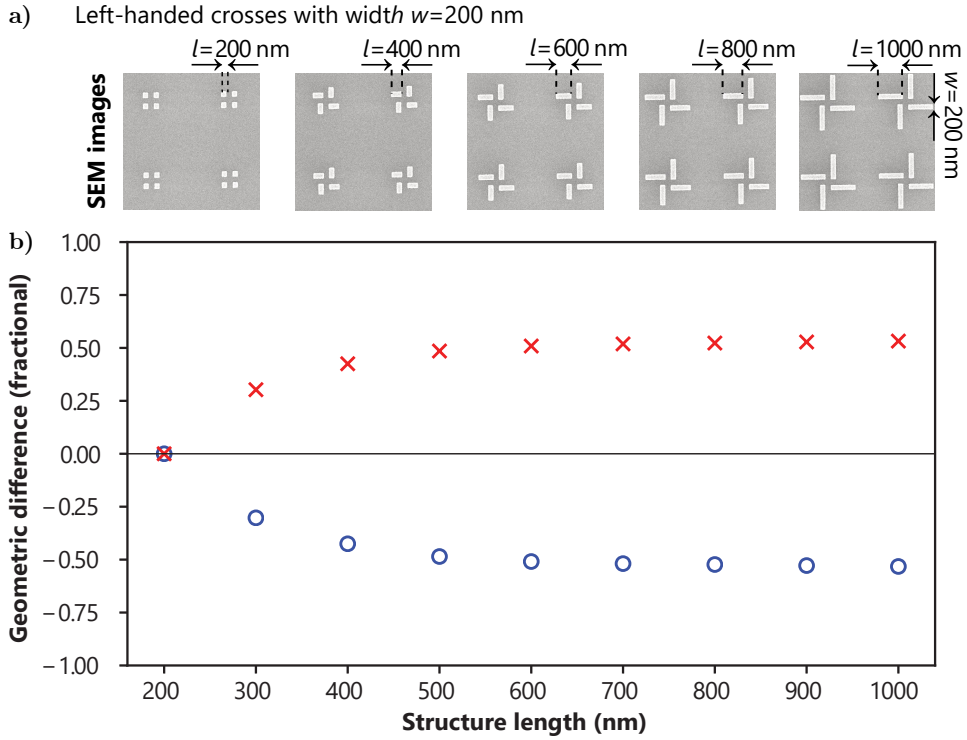

Figure 5.5: *Additional experimental and simulated CID results. Varying arm length of the nanostructure features at fixed $w = 200\,\text{nm}$.* ***a)****. SEM images of 4 structure cells for each geometry.* ***b)****. Chiral geometric difference for structures of fixed arm width $w = 200\,\text{nm}$.*

ure 5.5) in which the nanostripe length is varied, for a constant width of 200 nm. We observe in both the experiments (originating from near-field) and the near-field simulations that the CID emerges away from the achiral structure, and subsequently plateaus (figure 5.6). Although longer nanostripes support more electromagnetic modes than shorter ones, these additional modes spread across the whole structure, and do not influence dramatically the key central region. The nonlinear CID measurements probe the the centre of the crosses and, consequently, it plateaus as nanostripe length increases.

5.4 Conclusions

This chapter has focussed on the bisignate CID response as a function of varying a structure's geometry. With respect to wavelength, both linear and nonlinear chiroptical spectra often exhibit complex bisignate features [143, 144, 145, 146, 147]. This behaviour can be linked to Kuhn's sum-rule [148], which states that the chiroptical response must be zero over all wavelengths. This dependence on wavelength has been analysed in terms of exciton coupling [74] nanoparticle-nanoparticle Coulomb coupling [149], and energy level hybridisation [150]. In particular, in the linear optical case it was shown that the energetic ordering of the hybridised modes can be changed, resulting in a reversal of the linear CD, upon making small relative position shifts between L-shaped nanoparticles [151]. In the context of our group-theory discussion, the coupling coefficients of each mode pair are highly dependent on the wavelength of light. Changing the wavelength will change which mode pairs are dominant within the set, for a particular structure geometry. In principle,

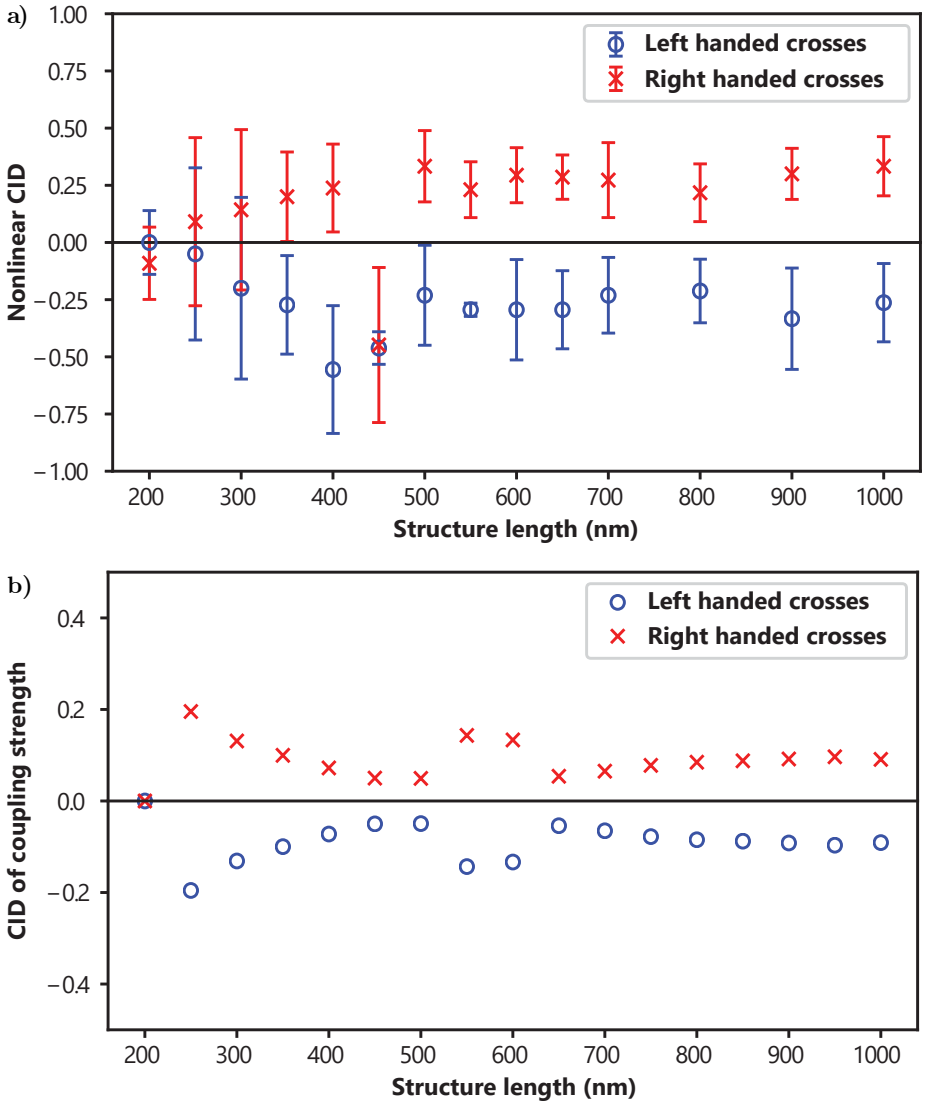

Figure 5.6: *Additional experimental and simulated CID results. Varying arm length of the nanostructure features at fixed* $w = 200\,\text{nm}$. ***a)*** *Measured total multi-photon CID, and* ***(b)*** *total coupling strength CID obtained from modal analysis, under* $\lambda = 800\,\text{nm}$ *wavelength light is then calculated for each geometry. Unlike the case of fixed length and varying width, no bisignate CID is observed here, more closely matching the chiral geometric difference.*

this can also be used to optimise the CID for a fixed structure and variable wavelength. However, it is often desirable, or even necessary, to operate at a particular wavelength, for example if probing molecules attached to the nanostructure surface. In these cases, tuning the structure geometry allows the near-field CID to be optimised around the available wavelength.

In this work, it has been shown that the origin of the chiroptical response in plasmonic nanostructures can be described by the selective excitation of available surface plasmon modes. Therefore, any physical property that affects the modes will allow tuning of the chiroptical response. This mechanism could also be used to explain previous experimental observations of bisignate CID spectra, where different sets of modes can be coupled differently depending on the wavelength of light. Furthermore, we predict that variation of

temperature of the nanostructures (e.g. by laser heating) will change the sets of available modes, due to thermal expansion or a change in permittivity [152], and can lead to tuning the chiroptical response. Further physical processes that involve excitation of specific plasmonic modes (Fano resonance, spasers, electromagnetically induced transparency, etc.) can also be used to tune that response for desired applications. In practice, maximising the chiroptical response in any plasmonic nanostructure is allowed by suppression of the modes that couple to light "with the wrong chirality". Equally important, by locally enhancing a particularly strong mode (e.g. via coupling to an auxiliary structure) it may be possible to enhance the chiroptical interaction with molecules. In many cases, these molecular interactions will occur at specific wavelength ranges. In this chapter it is shown that the chiroptical response at a specific wavelength can be enhanced, and even reversed, by tuning structure geometry alone. This tuneability will lead to improved enantioselectivity for molecular sensing, separation and synthesis.

Chapter 6

Optical Activity in Plasmonic Metasurfaces

Sections of this chapter have been copied verbatim from the (published) manuscript *"Second Harmonic Generation Optical Rotation Solely Attributable to Chirality in Plasmonic Metasurfaces"*, Joel T. Collins et. al. [4]. V. K. Valev designed the nonlinear experimental setup. A.G.Mark fabricated the samples. SHG data were collected by myself, and D. C. Hooper. Linear optical data were collected by myself and C. Kuppe. I analysed both the SHG and linear data. Tensor analysis and analytical verification of experimental results were performed by myself. I produced the manuscript draft on which this chapter is based.

As discussed in section 2.2.2, both linear and nonlinear optical rotation can occur even in achiral structures, if the structure is birefringent due to anisotropy, making pure chiral information difficult to obtain [8]. Crucially however, chiroptical effects resulting from anisotropy in planar nanomaterials exhibit a strong dependence on structural orientation about the surface normal. Here we report large second-harmonic generation optical rotation of $\pm 45°$, due to intrinsic chirality in a highly anisotropic helical metamaterial. The SHG *intensity* is found to depend strongly on the structural anisotropy, however even at oblique incidence the SHG-OR is invariant as the sample is rotated about the surface normal. The results show that by tuning the geometry of anisotropic nanostructures, the interaction between anisotropy, chirality, and experiment geometry can allow greater control over the chiroptical properties of plasmonic metamaterials.

6.1 Introduction

In this set of experiments, we made use of chiral optical metamaterials (section 4.2), whose properties are determined by both the choice of materials, and their geometry. Previously, large plasmon-enhanced linear CD and OR effects have been reported in chiral metamaterials [145, 153, 154, 155, 156]. Because CD and OR originate from the real and imaginary part of the refractive index, respectively, the two effects are linked by the Kramers-Kronig transforms (section 2.2). However, this link is not necessary for nonlinear chiroptical effects; since nonlinear CID and OR do not result from the real and imaginary

parts of a single complex number.

For second-harmonic generation (SHG), the two nonlinear chiroptical effects SHG-CID and SHG-OR are fundamentally different from, and can be highly complementary to, linear chiroptical effects. For the latter, interacting parallel components of electric and magnetic dipoles are strictly necessary. This necessity is lifted in the nonlinear case. Since SHG is a three-wave mixing process, chiroptical effects can arise from the 3D chiral arrangement of electric dipoles only [57]. SHG chiroptical effects can also originate from the interaction between electric and magnetic dipoles, as well as between electric dipoles and quadrupoles. This specificity allows SHG to discriminate between two principal models of chirality [157]: Kuhn's "chirally-coupled dipoles" [148] and Kauzmann's "one electron on a helix" [158, 159] models. More precisely, the two can be separated by measuring SHG-OR.

Whereas SHG-CID has been demonstrated from numerous chiral nanomaterials [8, 73, 111, 160, 75], far less attention has been devoted to SHG-OR. Previous studies have demonstrated SHG-OR in plasmonic nanostructures, where the origin of the effect can be ambiguous [161, 162, 163], since SHG-OR can originate from both intrinsic chirality and anisotropy. An unambiguously chiral origin of SHG-OR has not been previously reported in nano/meta-materials.

6.2 Results

Here, we demonstrate clear SHG-OR in plasmonic metamaterials, which is due to intrinsic chirality; the SHG-OR angle does not depend on the sample rotation angle and it reverses upon mirroring the geometry. Conversely, for the same sample, the linear OR angle depends strongly on the rotation of the sample, which demonstrates a dominant contribution from anisotropy rather than chirality, in the linear case. Moreover, we show that SHG-OR can also be dominantly sensitive to the anisotropy of the samples, depending on the experimental geometry and on the particular values of the nonlinear susceptibility tensor components involved.

The samples used in these experiments are arrays of hexagonally-arranged Au:Cu (80:20) nanohelices, fabricated by A.G.Mark using a glancing-angle shadow growth method [164]. The structures are shown schematically and in a cross-sectional SEM image in figure 6.1a and figure 6.1(b) respectively. Only one handedness of the structures is shown, however both left- and right-handed nanohelices were investigated. The individual nanohelices have a pitch of 37 nm, and height of 81 nm, a wire thickness of 18 nm, and the nanohelices have an inner and outer diameter of 28 nm and 55 nm, respectively. Consequently, the structures are substantially sub-wavelength ($\approx \lambda/10$, at 800 nm). The experimental setup (shown schematically in figure 6.1c) was designed to precisely measure the polarisation of SHG emission from the samples.

$8.4\,\mathrm{mW} \pm 0.1\,\mathrm{mW}$ of pulsed light centred at 800 nm (62 kW peak power, appendix B.1) was directed to a half-wave plate and rotated to a specific linear polarisation angle. An RG665 long pass filter removed any existing SHG from the beam, before an achromatic lens focused the 800 nm light onto our sample at 45 deg incidence. A BG39 filter then removed reflected 800 nm light, passing only the 400 nm SHG emission which was then collimated

by another lens. The SHG emission then passed through an analysing polariser, before being focused onto a photomultiplier tube (PMT). The PMT output is pre-amplified and sent to an SRS SR400 Gated Photon Counter. By varying both the sample azimuthal rotation angle and the analysing polariser angle, a heatmap is produced. The latter shows the intensity of SHG emission, as a function of both sample rotation (along the y-axis) and analyser rotation (along the x-axis).

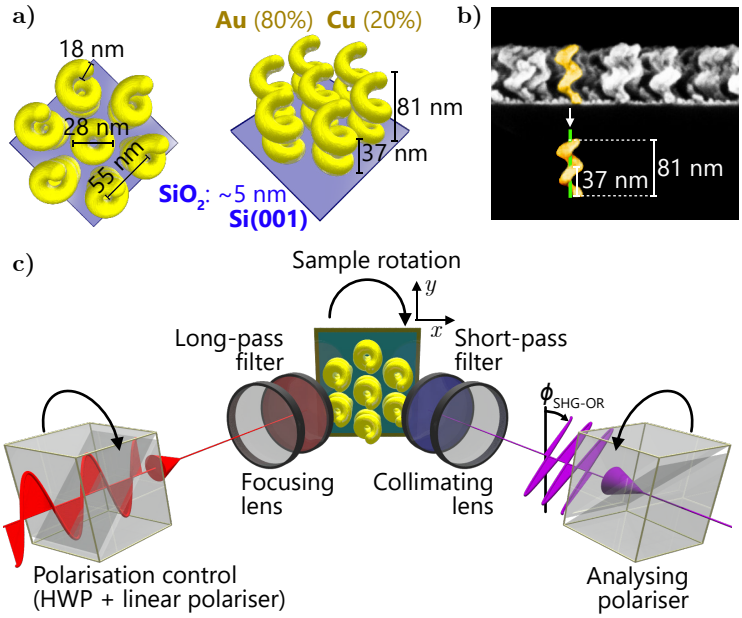

Figure 6.1: ***a)*** *Schematic diagram of one handedness of nanohelix array, showing structure spacing* 55 nm*, height* 81 nm*, and pitch* 37 nm*.* ***b)*** *Side-on SEM of the metamaterial surface, of the same handedness. A single helix has been highlighted for clarity.* ***c)*** *Schematic of experimental setup, showing S-polarised* 800 nm *incident light. For optical rotation measurements, the analysing polariser is continuously rotated, for a series of sample azimuthal rotations.*

Figure 6.2 shows SHG hotspots corresponding to the polarisation of SHG emission as the sample is rotated. The green markers on Figure 6.2 show the angle of SHG polarisation for each sample rotation angle. Relative to the incoming S-polarised (perpendicular to the plane of incidence) light, an SHG-OR of approximately $+45°$ is observed for the left-handed structures. Importantly, the SHG-OR angle does not change significantly over regions of strong SHG emission. Moreover, upon measuring the right-handed structures, the SHG-OR reverses to approximately $-45°$. While the data for the right-handed structure are noisier due to slight sample damage, the results are still clear. The reversal is exactly as expected for SHG-OR due to intrinsic chirality. The intensity of SHG emission does vary sinusoidally with rotation, suggesting a dipole coupling between the incident light and the end terminations of the nanohelices. After coupling into the structures via the end termination, the polarisation of light is then rotated by the intrinsic chirality of the helical structure.

Importantly however, SHG-OR is not always independent of sample anisotropy. As discussed in section 6.3, SHG is a highly symmetry-sensitive technique, whereby symmetry is expressed in the values of nonlinear susceptibility tensor elements. Depending on the experimental geometry, and on the values of these tensor elements, competing sym-

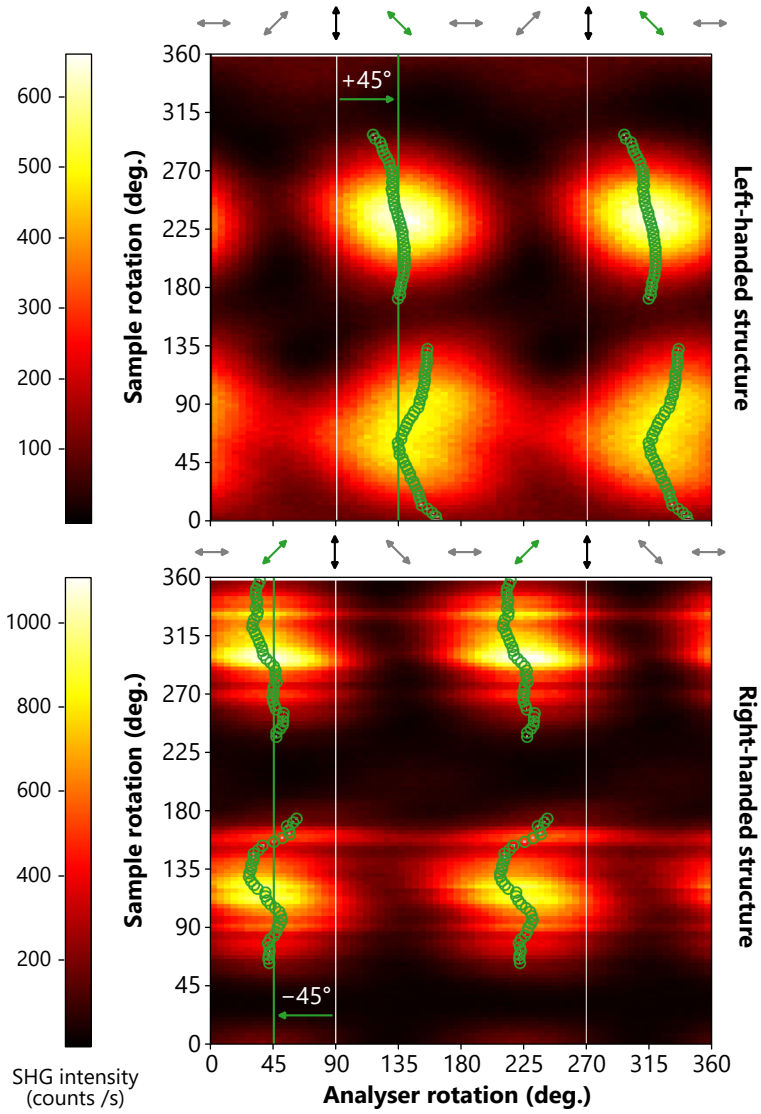

Figure 6.2: *SHG optical rotation heatmaps for both enantiomorphs of helical metamaterial. S-polarised incident light results in rotated linearly polarised SHG emission. By continuously rotating the analyser, the angle of maximum intensity at each sample rotation can be obtained (shown in green markers). For the left-handed structure an SHG-OR angle of around +45° is found. In the mirrored, right-handed structure, the SHG-OR changes sign, to around −45°. Importantly, in both cases the angle remains relatively unchanged upon sample rotation, though the overall intensity varies periodically.*

metries within the structure can be dominant in the measured results. This is directly demonstrated in figure 6.3. The data presented in figure 6.3 were obtained from the same nanohelices, however whereas in figure 6.2 we used S-polarised light, here P-polarised light was employed. As in figure 6.2, the heat maps correspond to SHG intensity as a function of sample and analyser rotation angles. Contrary to figure 6.2, the SHG-OR angle changes significantly over the regions of SHG emission, closely following the sample rotation angle. This behaviour is exactly as expected for SHG-OR dominantly due to sample anisotropy. The experimental geometry must be carefully selected to address the structural chirality exclusively. Furthermore, additional data presented in Appendix D demonstrate that the precise experimental conditions required to isolate instrinsic chirality, and anisotropy,

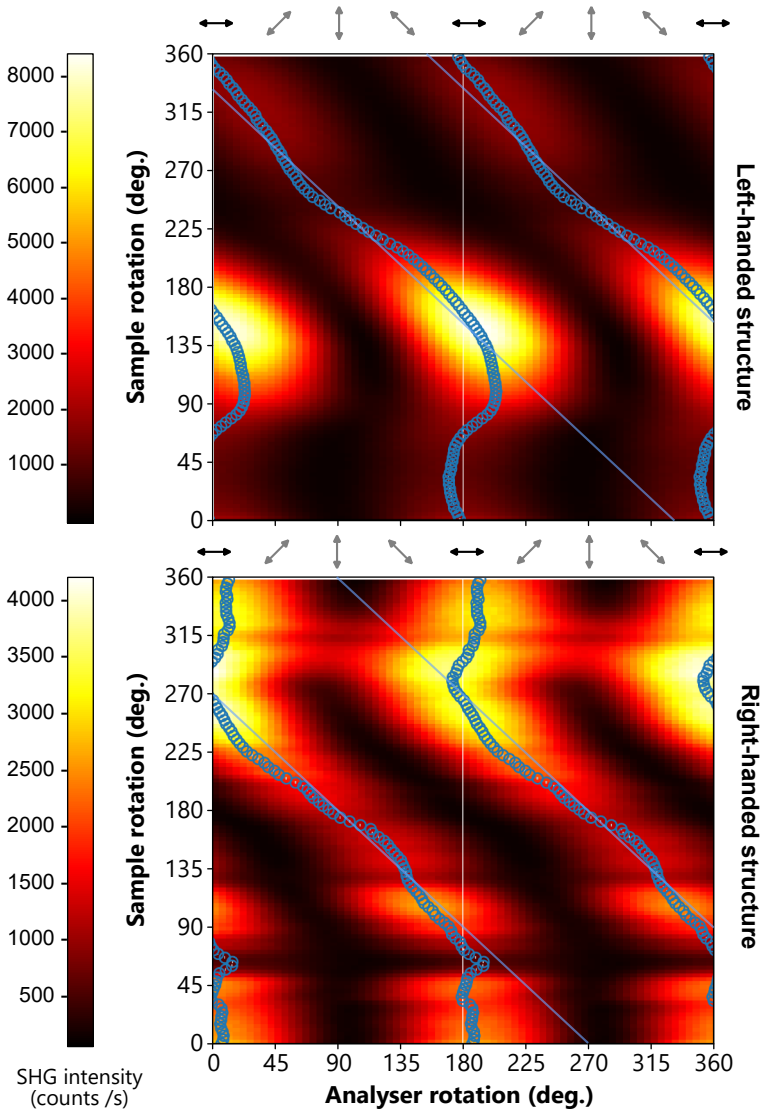

Figure 6.3: *SHG optical rotation heatmap for both enantiomorphs of the helical metamaterial, for P-polarised (parallel to the plane of incidence) incident light. In this case, both the angle of SHG-OR and the intensity of SHG emission are strongly dependent on sample rotation. Additionally, there is no clear reversal between enantiomorphs of the metamaterial. Instead, the sign of SHG-OR reverses under sample rotation, suggesting contributions from anisotropy dominating over contributions from the structure's intrinsic chirality.*

depend strongly on the geometry of the nanomaterial. We observe that changes in the nanohelix separation have a large impact on the nonlinear optical activity, entangling the effects of chirality and anisotropy. Changes in the nanohelix dimensions with the same separation have a less dramatic effect, preserving the anisotropy-dominated SHG-OR under p-polarised illumination, but also exhibiting no behaviour *exclusively* attributable to chirality.

The nonlinear chiroptical behaviour reported here is in stark contrast to the linear chiroptical case. The linear OR of the nanohelices was investigated with optical microscopy and spectroscopy. Microscopy images were obtained on a commercial Zeiss Axio Imager M2m wide-field microscope, with a halogen lamp for illumination. Images were taken in bright-field reflection mode, through an Epiplan-Neofluar 20×/0.50 HD DIC objective,

using an Axiocam 105 colour camera. Incident polarisation was controlled using a fixed Zeiss linear polariser slider, with the output image analysed with a Zeiss 360 deg rotatable analyser slider. The analyser can be precisely rotated through 360°. Under crossed polariser geometry, only light that has experienced OR reaches the detector. By rotating the analyser, the sign of this OR can be obtained.

Figure 6.4a shows a 3×3 array of optical microscopy images (in colour) of the nanohelices. The rows correspond to three different sample rotation angles (0°, 45° and 90°) and the columns corresponds to three analyser rotation angles (85°, 90°, 95°). The sign of OR is revealed by colour contrast in the images. For a sample oriented at 0° and an analyser positioned at 85°, the image appears green. Upon rotating the analyser to 95°, the colour changes to red. However, upon orienting the sample at 90°, the colour contrast reverses, indicating an opposite OR. This behaviour suggests that the angle of OR depends on sample orientation and that OR changes sign every 90°. This trend is confirmed in figure 6.4b, showing an OR spectral map, obtained by rotating the sample between crossed polarisers. Spectra were obtained by diverting the microscope image to a collection lens focusing onto a 400 µm diameter multimode optical fibre. The output of the fibre was connected to an Ocean Optics QE Pro commercial spectrometer, running with a 500 ms integration time. The spectral data is normalised to account for the spectral lineshape of our halogen lamp source. Reference spectra were obtained using a silver mirror to measure the spectral lineshape of the source only. The measured metamaterial spectra were divided by this reference to give spectra independent of the illumination source. Here, a 90° rotational periodicity for the OR is clearly visible, at wavelengths above 550 nm. The behaviour of the sample is consistent with that of a radiating dipole rotated through 360°. Such a dipole can be situated at the end-termination of the nanohelices. In the ranges of study, this dipole is excited by wavelengths from 550 nm to 800 nm. The latter is the fundamental wavelength used for the SHG data in Figures 6.2 and 6.3, where the SHG intensity also depends on coupling to the end-termination dipole, as discussed above.

6.3 Discussion

Due to the sub-wavelength dimensions and separation of nanostructure inclusions, our sample can be treated as an effective dielectric medium, described by effective susceptibility tensors as in section 3.2. At a given optical frequency ω, the nonlinear chiroptical effects are described in terms of the nonlinear susceptibility tensors, relating the induced polarisation (P) at the second-harmonic (2ω) to the driving electric (E) and magnetic (B) fields, by equation 6.1.

$$P_i(2\omega) = \varepsilon_0 \chi_{ijk}^{eee} E_j(\omega) E_k(\omega) + \varepsilon_0 \chi_{ijk}^{eem} E_j(\omega) B_k(\omega) + \varepsilon_0 \chi_{ijk}^{eme} B_j(\omega) E_k(\omega) \qquad (6.1)$$

The indices i, j, and k describe the Cartesian directions of the fields, and can represent x, y, or z (see figure 6.1c). The superscripts e and m stand for electric and magnetic dipole transitions, respectively, while ε_0 is the permittivity of vacuum. In addition to equation 6.1, the incident electromagnetic fields can induce a magnetisation M_i analogous

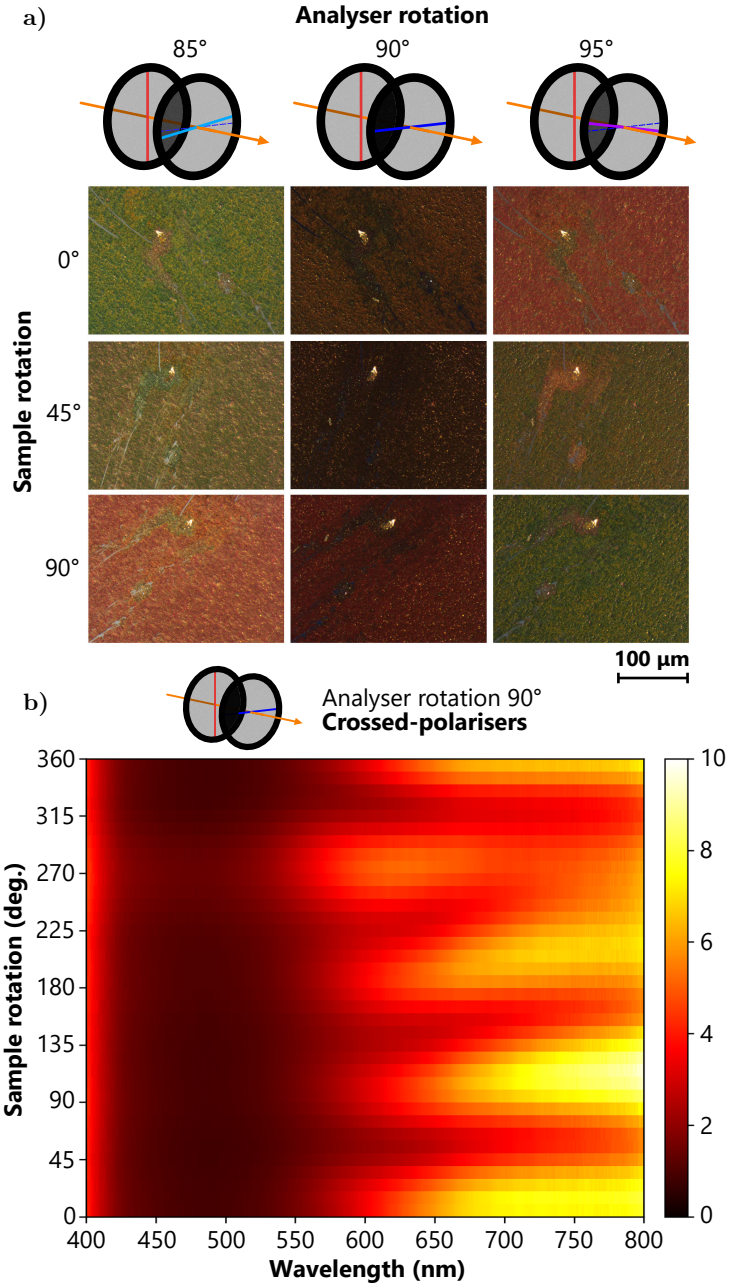

Figure 6.4: *Linear optical rotation data obtained through microscopy.* ***a)*** *Microscopy images of left-handed structure under illumination by linearly polarised white light, with various almost-crossed analysing polariser angles. By rotating the analyser slightly away from crossed (90°), the spectral dependence of optical rotation can be observed. Longer wavelengths are transmitted more through the analyser when oriented at +5° away from crossed. Upon rotating the structure by 90° the OR reverses.* ***b)*** *Linear OR map obtained from a spectrometer connected to the microscope viewport, showing clear dependence on sample rotation. Since the sample is between crossed polarisers, positive and negative OR both increase the measured intensity.*

to the polarisation P_i. In our experiment (figure 6.2), the incident electric field is polarised perpendicularly to the main helix axis, therefore this magnetic contribution is excluded. Away from resonance, the magnetic component of the incident light is much weaker than the electric component. In this analysis, only the contributions from electric dipoles (eee) are considered. Furthermore, for collinear SHG experiments, the incident fields $E_j(\omega)$ and $E_k(\omega)$ are indistinguishable. This allows equation 6.1 to be reduced under permutation

symmetry as in section 3.2.3.

The presence of spatial symmetry can further reduce the number of non-zero tensor components. The presence of surface isotropy (full rotational symmetry about the surface normal) would eliminate 11 components (section 3.2.4). We can refer to these as the "anisotropy components". Likewise, for a tensor with mirror symmetry, 8 components are eliminated (section 3.2.5). These "chirality components" are therefore only present in chiral structures. Importantly, both anisotropy and chirality tensor components can contribute to SHG-OR.

The nanohelix sample is a chiral, anisotropic surface. With S-polarised light, $E_j(\omega)$ and $E_k(\omega)$ are polarised along the sample y-axis. Therefore, only the χ_{xyy}, χ_{yyy} and χ_{zyy} tensor components are addressed. Here, we examine each component individually. First, we can see that χ_{zyy} is neither an in-plane anisotropy, nor a chirality parameter. Second, χ_{yyy} is an anisotropy but not a chirality parameter. And third, χ_{xyy} relates to *both* anisotropy and chirality. Rotating the sample by an angle θ around the surface normal is equivalent to applying a rotation operation to the $\chi_{ijk}(2\omega)$ tensor. The treatment can be simplified by introducing effective nonlinear susceptibility tensor components as given in equation 6.2.

$$\begin{aligned}
&\chi^{eff}_{xyy}(\theta) = \cos\theta\sin^2\theta(\chi_{xxx} - 2\chi_{yyx}) \\
&+ \cos^2\theta\sin\theta(2\chi_{xyx} - \chi_{yyy}) + \cos^3\theta(\chi_{xyy}) - \sin^3\theta(\chi_{yxx}), \\
&\chi^{eff}_{yyy}(\theta) = \cos\theta\sin^2\theta(2\chi_{xyx} - \chi_{yxx}) \\
&+ \cos^2\theta\sin\theta(2\chi_{yyx} - \chi_{xyy}) + \cos^3\theta(\chi_{yyy}) - \sin^3\theta(\chi_{xxx}), \\
&\chi^{eff}_{zyy}(\theta) = \cos\theta\sin\theta(2\chi_{zxy}) + \sin^2\theta(\chi_{zxx}) + \cos^2\theta(\chi_{zyy}).
\end{aligned} \tag{6.2}$$

Within the dipole approximation, the angle of SHG-OR is $\phi = \arctan\left(\frac{E_P(2\omega)}{E_S(2\omega)}\right)$. The values of the electric fields at the second-harmonic are obtained from $\mathbf{E}(2\omega) \sim [\mathbf{n} \times \mathbf{P}(2\omega)] \times \mathbf{n}$, where $\mathbf{P}(2\omega)$ is a vector describing the induced polarisation, and $\mathbf{n}$ is a unit vector describing the angle of observation. In our experimental configuration, the angle of optical incidence is 45°, hence $E_P(2\omega) \propto \frac{1}{2}(\chi^{eff}_{zyy}(\theta) - \chi^{eff}_{xyy}(\theta))$ and $E_P(2\omega) \propto \chi^{eff}_{yyy}(\theta)$. The angle of SHG-OR in this configuration is therefore given by equation 6.3.

$$\phi = \arctan\left(\frac{\chi^{eff}_{zyy}(\theta) - \chi^{eff}_{xyy}(\theta)}{2\chi^{eff}_{yyy}(\theta)}\right) \tag{6.3}$$

Likewise, the intensity of SHG emission is given by equation 6.4.

$$I_{SHG} \propto \frac{1}{4}\left|\chi^{eff}_{zyy}(\theta) - \chi^{eff}_{xyy}(\theta)\right|^2 + \left|\chi^{eff}_{yyy}(\theta)\right|^2 \tag{6.4}$$

Although not trivial, the effects of anisotropy and chirality can be disentangled. To achieve this, equation 6.5 presents a suitable set of intrinsic tensor component relationships, as an

example.

$$\begin{aligned}&\chi_{xxx} = \pm 0.5; \chi_{xyy} = \mp 0.58; \chi_{yyx} = \pm 0.55 \\ &\chi_{yxx} = 1.0; \chi_{yyy} = 0.34; \chi_{zyy} = 0.05; \chi_{zxx} = 0.02; \chi_{zyy} = 0.05; \chi_{zyx} = 0.01\end{aligned} \tag{6.5}$$

The top three tensor components are pseudo-scalars associated with chirality, and thus change sign depending on the handedness of the structure (+ and − for left- and right-handed structures, respectively). The lower 6 tensor components describe structural anisotropy, and do not change sign under parity inversion. With the values in equation 6.5, we can calculate the SHG intensity and SHG-OR, for both enantiomorphs, see Figure 6.5. The figure has the same layout as Figure 6.2 and it can be seen that it matches very well the experimental behaviour.

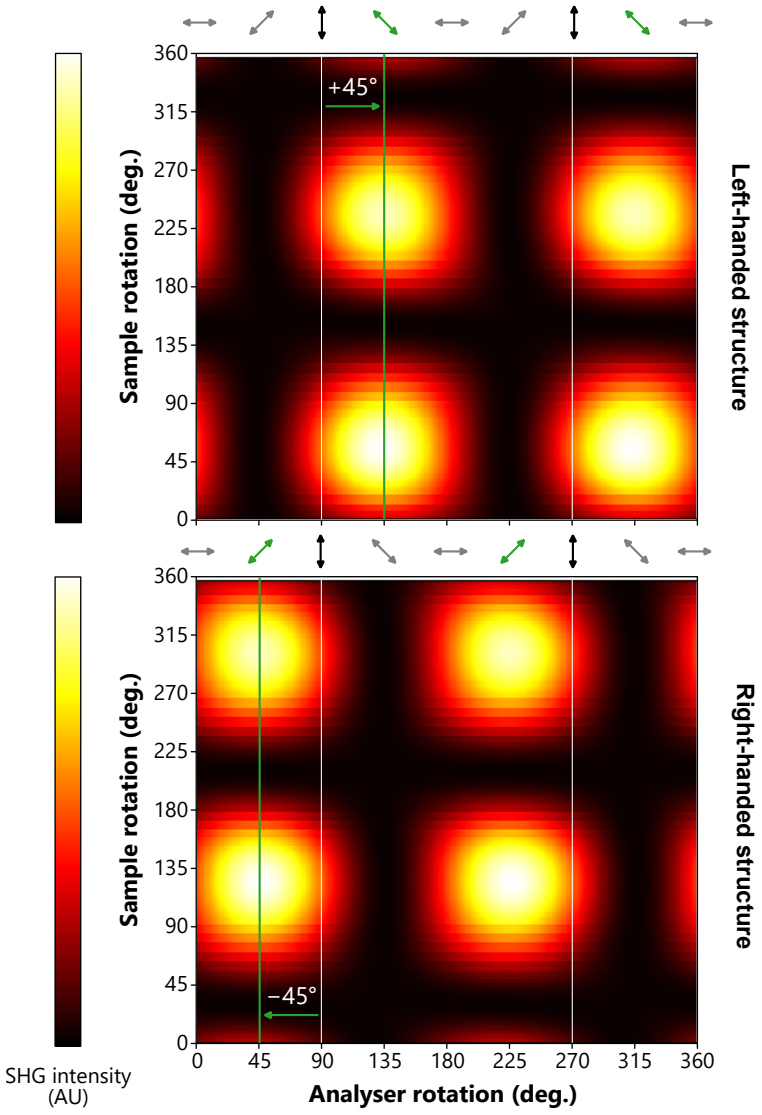

Figure 6.5: *SHG optical rotation heatmaps for the susceptibility tensor relationships given in equation 6.5. The SHG-OR behaviour closely matches that observed in Figure 6.2.*

In an *isotropic* metasurface, composed of nanohelices, two principal models can be used to theoretically quantify the nonlinear optical activity. The first model builds upon Kauzmann's "one-electron chirality" [159]. In its nonlinear treatment, the nonlinear op-

tical activity requires magnetic dipoles caused by the electron's helical motion [158, 165]. The second model, builds upon Kuhn's [148] chirally-coupled electric dipole moments. In its nonlinear treatment, the nonlinear optical. activity requires only electric dipole moments [165]. In plasmonic nanomaterials this could be the coupling between any chirally-arranged metallic features. Importantly, the "one-electron" model permits only SHG-CID, whereas the coupled-dipole model allows SHG-CID, SHG linear dichroism (SHG-LD), and SHG-OR [157]. Unlike linear chiroptical measurements, information is gained by measuring both SHG-CID and SHG-OR: the mechanism of a structure's chiroptical response can be determined by comparing these two nonlinear chiroptical effects.

However, when treating *anisotropic* surfaces, the analysis is much more complex than in the isotropic case. SHG-OR is possible in both models, and there is no simple distinction between the two. Slight changes in the structure design can result in significant changes in the optical behaviour, due to the large number of interacting tensor components responsible for the SHG-OR. As we have observed, this complexity can result in interesting and highly desirable optical properties, under the right experimental and geometric conditions. The flexibility of geometry makes metamaterials an ideal platform for exploring this interplay between structural and experimental geometry.

Finally, it is important to consider that the SHG-OR in Figure 6.2 could, in principle, originate from the out of plane anisotropy axis. SHG-OR effects from this axis would not change under azimuthal sample rotation. However, such an anisotropy-induced SHG-OR would not change sign, depending on the handedness of the nanohelices. Consequently, because our SHG-OR changes sign depending on handedness, we can conclusively attribute it to chirality.

6.4 Conclusions

To conclude, this chapter reports a large SHG-OR effect of ± 45 deg from planar chiral metamaterials. The effect is due to the intrinsic chirality of the helical nanostructures; the angle of SHG-OR is rotationally invariant, and, as expected, it reverses for the mirrored structures. Contrary to their linear chiroptical counterparts, SHG-CID and SHG-OR are not trivially related to one another. Therefore, these results pertain to an important and previously unobserved chiroptical effect in this kind of system. We have demonstrated that, under specific experimental conditions, it is possible to extract purely chiral information from highly anisotropic structures. Further work on disentangling chiral and anisotropic contributions to nonlinear chiroptical effects will unveil the physical mechanisms at work and will lead to their optimisation.

Chapter 7

Optical Activity in Hyper-Rayleigh Scattering

Sections of this chapter are based on the (accepted) manuscript *"First observation of optical activity in hyper-Rayleigh scattering"*, Joel T. Collins et. al. [1]. I designed the nonlinear experimental setup. H.-H. Jeong and P. Fischer fabricated the samples. HRS data were collected by myself, K. R. Rusimova, and D. C. Hooper. Linear optical data were collected by myself, K. R. Rusimova, and F. Pradaux-Caggiano. I analysed both the HRS and linear data, with contributions to the discussion from T. Verbiest. I produced the manuscript draft on which this chapter is based.

As discussed in the previous chapter, separating true chirality of nanomaterials from structural anisotropy is a major challenge. This chapter discusses an experiment designed to entirely remove anisotropic contributions to nonlinear chiroptical measurements in nanostructures: The first observation of optical activity in hyper-Rayleigh scattering (HRS). The effect is demonstrated in a 3D isotropic suspension of Ag nanohelices in water, and shows a complete sign reversal depending on handedness, as would be expected from an intrinsically-chiral origin. Moreover, the effect is significantly stronger than linear optical activity, and is well-pronounced above the multiphoton luminescence background. Because of its sensitivity, isotropic environment, and straightforward experimental geometry, HRS optical activity constitutes a fundamental experimental breakthrough in chiral photonics, for media including nano/metamaterials and chemical molecules.

7.1 Introduction

With the invention of the laser, access to high-intensity light enabled the discovery of nonlinear optical counterparts of optical activity (section 3.3). However, nonlinear chiroptical techniques have not been widely adopted as routine chiroptical probes. A major drawback is that sum-frequency generation (SFG) intensities cannot distinguish between left and right-handed molecules [34]. Second-harmonic processes require symmetry-breaking interfaces and, as shown in section 3.3, are more widely used in the chiroptical characterisation of solids than liquids. In solids however molecules can exhibit anisotropy

that can easily mask the chiral response by contributing to linear dichroism, linear birefringence and circular birefringence [166]. Furthermore, in solid samples, disentangling chirality from anisotropy effects is challenging, particularly for nonlinear optics [8] (section 6). More chiroptical processes have been reported in higher-order nonlinearities, for instance, two-photon absorption circular dichroism [167, 168, 169] – a third-order process. However, higher-order nonlinearities are generally weaker, and the associated experimental techniques are complex. Therefore, nonlinear optical effects capable of distinguishing chiral forms in a liquid are highly desirable.

This chapter discusses the observation of optical activity in hyper-Rayleigh scattering (HRS), 5 orders of magnitude more pronounced than linear OA when considering the volume of optical interaction. HRS [170, 171] occurs when incident light at a fundamental frequency is scattered at the second-harmonic frequency, and is used to determine the symmetry of randomly oriented molecules in a liquid [172]. These experiments made use of sub-wavelength silver chiral nanohelices suspended in water, to form a meta-molecular liquid, and demonstrate a strong HRS signal, well distinguishable above multiphoton luminescence. Polarisation analyses of the HRS establishes that the nanohelices are isotopically arranged in the liquid. The nanohelices give rise to an HRS-CID signal that reverses for opposite chirality of the nanohelices and is much larger than the two- and three-photon luminescence CID. Moreover, the HRS and HRS-CID signals follow variations in fundamental wavelength. Crucially, in comparison to linear OA, the HRS-CID only occurs near the focal point of light, which opens up a range of applications in tiny volumes of liquids. In HRS-CID, incident light at a frequency ω is left- circularly polarised (LCP) or right-circularly polarised (RCP). Meta-molecules in a liquid scatter the incident light into the second-harmonic frequency 2ω. This hyper-Rayleigh scattered light can be detected at 90° to the incident beam propagation direction. Due to the chirality of the scatterers, HRS of different intensity is produced for LCP and RCP light.

7.2 Results

The nanostructures are Ag nanohelices, fabricated by H.-H. Jeong and P. Fischer using a glancing-angle shadow growth method [164], and suspended in water. Additionally, 3-5% Ti is co-deposited with the Ag, in order to improve the structural fidelity of the nanoparticles while causing little change in their optical properties [173]. The Ti results in a rapidly forming oxide layer at room temperature, which quickly saturates at 3-5 nm. Since Ti is more reactive with oxygen than Ag at room temperature, this becomes the dominant oxide layer. In principle, this layer changes the optical properties of the helices, however once the layer has rapidly formed, it grows extremely slowly (taking approximately a year to grow from 4 nm to 5 nm [174, §7.3]). Therefore, the oxide layer will not change significantly over the course of the experiment. Additionally, since the layer has already formed from oxygen exposure, it protects the Ag from any further degradation while suspended in water. For these experiments, Ag nanohelices were used over Au nanohelices (such as those examined in chapter 6) due to exhibiting a stronger plasmon resonance at a given geometry and volume. The results presented below make use of several incident

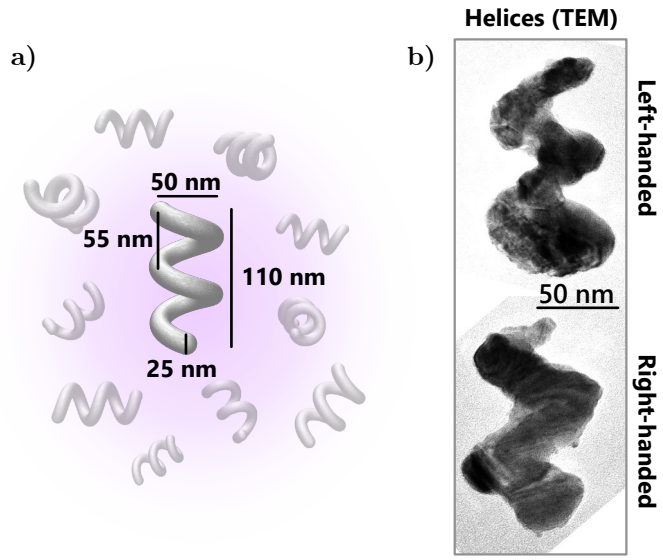

Figure 7.1: ***a)*** *Dimensions (centre-to-centre) of the nanohelices isotropically dispersed in water. Helix height is* 110 nm*, loop diameter is* 50 nm*, loop pitch is* 55 nm*, and wire-diameter is* 25 nm*.* ***b)*** *Transmission Electron Microscopy (TEM) images of left- and right-handed helices.*

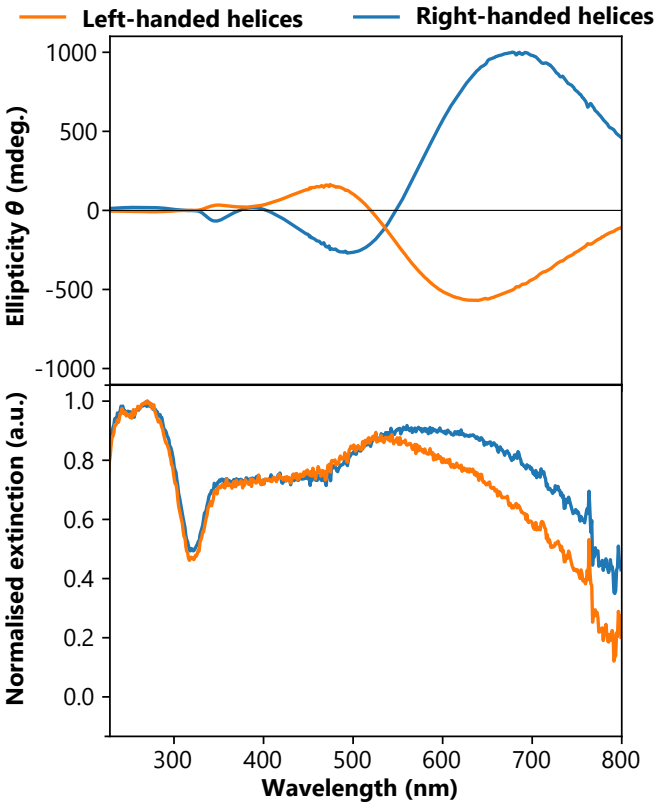

Figure 7.2: *Linear characterisation of the nanohelix solutions.* ***Top:*** *ellipticity spectra, as measured with a CD spectrometer, through a* 1 cm *path length filled with left- and right-handed nanohelix suspensions.* ***Bottom:*** *corresponding normalised extinction spectra from the left- and right-handed nanohelix suspensions. Extinction is obtained from the transmission spectrum and describes both absorption and scattering losses.*

wavelengths, and thus the broader resonance of dispersed nanoparticles allows measurable signal to be obtained over a wider spectral range.

The nanohelices' dimensions, presented in figure 7.1a, are substantially smaller than the wavelength of illumination (720 nm-780 nm). Since the wire radius (12.5 nm) is comparable to the skin depth of Ag for 760 nm light [175], each helix acts as a continuous helical arrangement of effective dipoles. Transmission Electron Microscopy (TEM) images of both chiral forms (enantiomorphs) are shown in figure 7.1b. After fabrication on Si wafers, the wafers are cut into 1 cm^2 pieces that are each sonicated into 1.4 ml water, with 1 mmol of sodium citrate stabiliser to create $\approx$ 20 picomolar suspensions. These suspensions are stable over several days and can be dispensed into standard glass cuvettes for characterisation with linear and nonlinear optical techniques.

Figure 7.2 shows linear ellipticity and extinction spectra (upper and lower panels respectively) for both enantiomorphs, obtained using a commercial Applied Photophysics Chirascan. A N_2-cooled Xe arc lamp is linearly polarised and spectrally separated in space with a pair of prisms, and a variable-width slit is used to select a wavelength with 0.1 nm resolution. A photoelastic modulator (PEM) modulates the beam between LCP and RCP states, which is then directed through the sample cuvette and onto a photomultiplier tube (PMT) detector. The Chirascan then simultaneously measures total extinction and circular dichroism and constructs spectral data by scanning the wavelength. The ellipticity θ is a measure of the CD:

$$\theta(\text{deg.}) = \frac{180}{\pi}\tan^{-1}\left(\frac{\sqrt{I_{RCP}}-\sqrt{I_{LCP}}}{\sqrt{I_{RCP}}+\sqrt{I_{LCP}}}\right) \approx \frac{180}{\pi}\Delta A\left(\frac{\ln 10}{4}\right) \tag{7.1}$$

where I_{RCP} and I_{LCP} denote the intensity of RCP and LCP light, respectively, and $\Delta A = A_{LCP} - A_{RCP}$ is the difference in the attenuation of LCP and RCP light transmitted through the cuvette. The ellipticity spectra exhibit a characteristic bisignate signature that reverses with the handedness of the nanohelices. Their small asymmetry in peak maxima is due to a slight difference in concentration, attributable to experimental variation in the sonication process. Additionally, because the two chiral forms of the nanohelices are grown separately, small imperfections in the structural dimensions are also present, resulting in a slight shift in peak wavelength. The small effect of these imperfections can be seen from the extinction spectra, where the lines deviate only above 550 nm. The extinction is proportional to both the absorption and the scattering from the nanohelices; such scattering can also occur at the second-harmonic frequency of illumination.

Figure 7.3 shows the experimental setup used to measure HRS-CD. 18.9 mW $\pm$ 0.1 mW of pulsed light (139 kW peak power, appendix B.1) with a tunable centre wavelength, was horizontally polarised (p-polarisation), before passing through a quarter-wave plate mounted in an automatic rotation stage to give LCP or RCP light. An RG665 long pass filter removed any existing SHG from the beam, before a 100 mm focal-length achromatic lens focused the incident light onto our cuvette. A 50 mm focal-length collection lens positioned 50 mm from the cuvette, along with a 50 mm focal length curved mirror positioned 100 mm from the opposite side of the cuvette, collected and collimated scattered light. A 200 mm focal length lens then focused the collected light through one of several band-pass filters, onto a photomultiplier tube (PMT). The PMT output was pre-amplified and sent to an SRS SR400 Gated Photon Counter. By changing the band-pass filter, in 10 nm

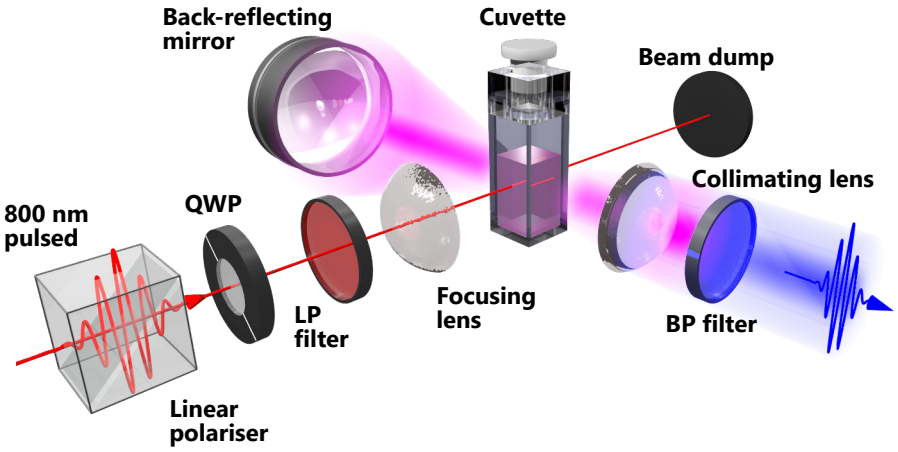

Figure 7.3: *Schematic diagram of the hyper-Rayleigh scattering CID experimental setup. QWP: quarter wave-plate; LP filter: long-pass filter; BP filter: band pass filter.*

increments, a spectrum of the multiphoton scattering is measured.

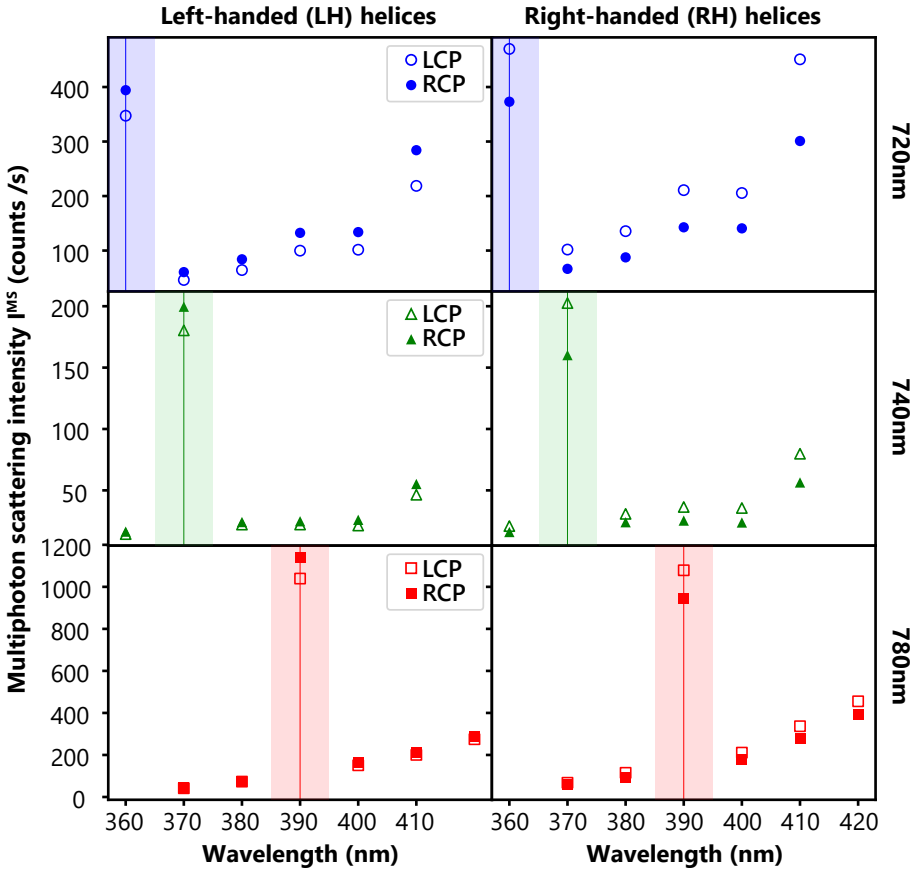

Figure 7.4: *Multi-photon scattering spectra for left- and right-handed helices, under LCP and RCP illumination. Results obtained for fundamental wavelengths of* 720 nm, 740 nm *and* 780 nm *are shown in blue, green, and red, respectively. Vertical coloured lines mark the HRS (second-harmonic) wavelength, demonstrating clear peaks above the multiphoton luminescence background. The HRS unambiguously follows variations of the fundamental.*

Figure 7.4 shows the obtained multiphoton scattering spectra for both left- and right-handed nanohelix suspensions, under LCP and RCP illumination at three fundamental

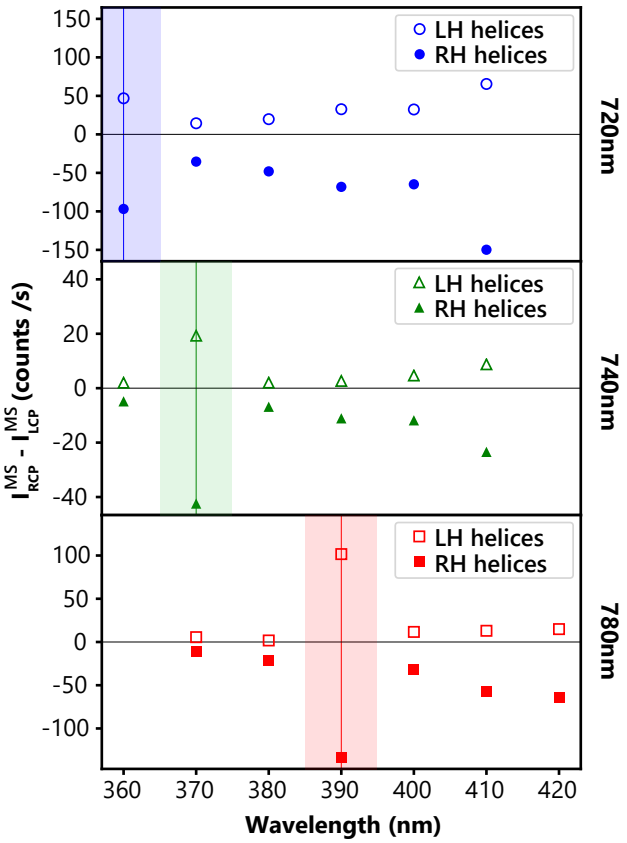

Figure 7.5: *Circular difference in multiphoton scattering intensity (quantified by $I^{MS}_{RCP} - I^{MS}_{LCP}$), for both left-handed (LH) and right-handed (RH) nanohelix suspensions. Again, pump wavelengths of* 720 nm, 740 nm *and* 780 nm *are shown in blue, green, and red, respectively, and vertical coloured lines mark the HRS (second-harmonic) wavelength. The circular difference in the HRS intensity clearly reverses between nanohelix enantiomorphs.*

wavelengths: 720 nm, 740 nm and 780 nm (shown in blue, green, and red respectively). The second-harmonic is marked by a vertical line, with the shaded region denoting the bandwidth of the band-pass filter used. At all three fundamental wavelengths, a clear peak is observed at the second-harmonic, corresponding to hyper-Rayleigh scattering well above the multiphoton luminescence background. Additionally, background measurements were taken by measuring the HRS of the sodium-citrate water solution, without nanohelices. In these experiments, no HRS *or* multi-photon luminescence counts were detected during the 30 second counting window. Additionally, due to the long integration time and corresponding high number of detected counts, statistical uncertainties are negligible, assuming that the detected count rates are governed by Poissonian statistics.

Importantly, a clear difference in HRS intensity between RCP and LCP illumination is also observed. This effect is emphasised in figure 7.5, which shows the circular difference in multiphoton scattering intensities ($I^{MS}_{RCP} - I^{MS}_{LCP}$) for both enantiomorphs, obtained from the data shown in figure 7.4. At all three fundamental wavelengths, a clear peak in circular difference is observed at the second-harmonic, reversing sign between enantiomorphs indicating an intrinsically chiral origin. The HRS-CID is significantly larger than the neighbouring two- and three-photon luminescence CID, which are also recorded.

To further verify the chiral origin of the measured HRS-CID, linearly polarised HRS

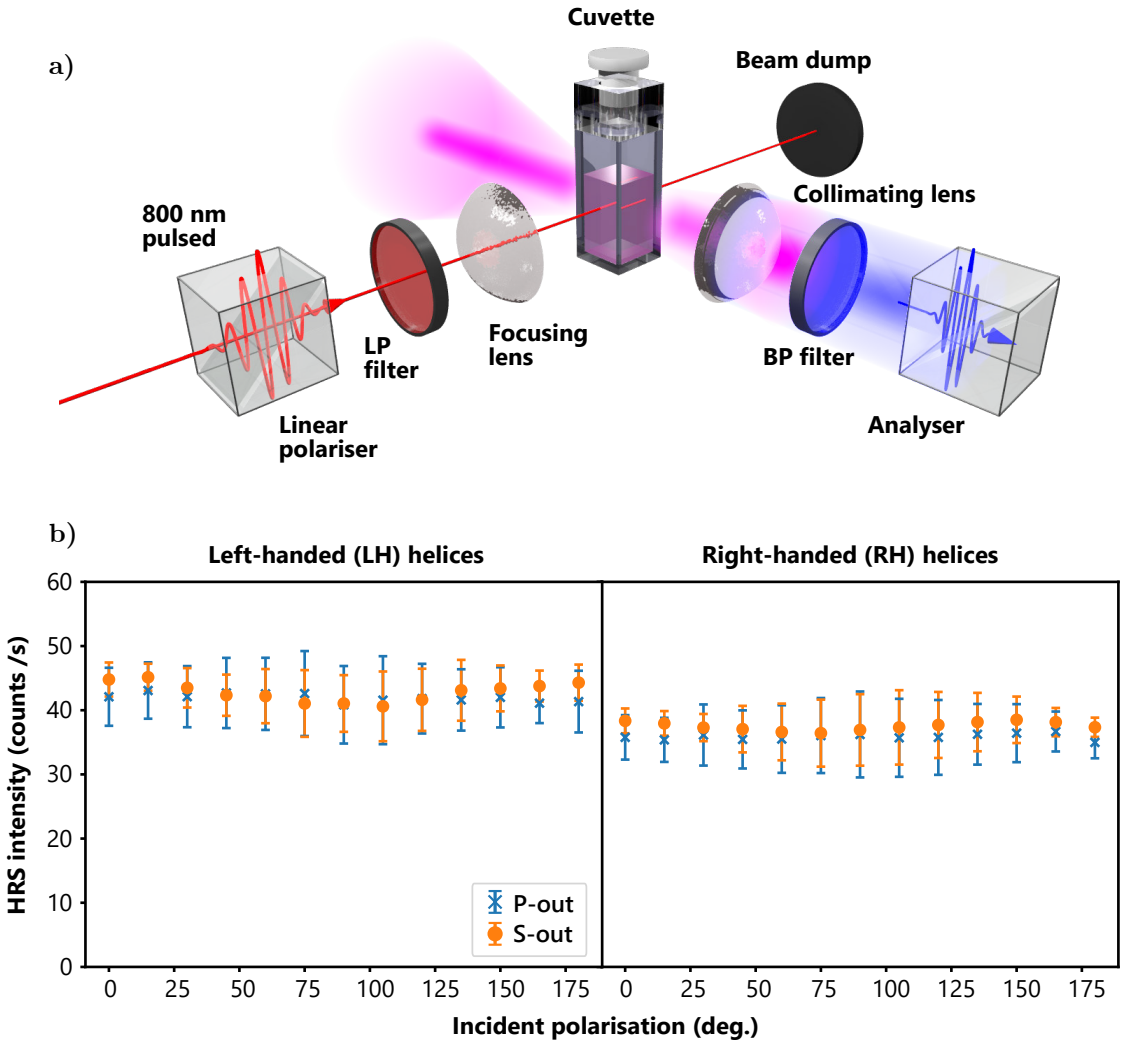

Figure 7.6: *The nanohelices are isotropically suspended in water.* ***a)*** *Schematic of the setup used to measure hyper-Rayleigh scattering of linearly polarised incident light.* ***b)*** *P-polarised (blue crosses) and S-polarised (orange dots) HRS intensity at* 360 nm*, as the polarisation of* 720 nm *incident light is rotated. Both left-handed (LH) and right-handed (RH) nanohelix suspensions exhibit no variation outside of experimental uncertainty, demonstrating a clear isotropic arrangement of helices within the liquid suspension.*

measurements are performed. Figure 7.6a shows the setup used in these measurements. Here, the incident polarisation is linear and can be freely rotated. An analysing polariser is placed before the detector, allowing the HRS signal to be decomposed into P-polarised (horizontal) and S-polarised (vertical) components. Both left- and right-handed nanohelix suspensions were examined, at an incident wavelength of 720 nm, with a 360 nm band-pass filter at the output, selecting the HRS. Figure 7.6b shows the P- and S-polarised components of HRS intensity as the incident polarisation is rotated. For both P- and S-polarised HRS, and for both enantiomorphs, it can be seen that HRS intensity remains constant. This result establishes an isotropic arrangement of nanohelices, and indicates a dipolar origin of the HRS response [176, 57].

Additional reference data was taken, but found to serve only as an interesting contrast to the anisotropy of the nanohelices. In order to measure an HRS reference for a fully

isotropic medium, a water suspension of 20 nm spherical Ag nanoparticles was studied using a similar method as in figure 7.6. Here however, the incident polarisation was fixed at either P- or S-polarised, and the analysing polariser freely rotated. It is important to also note that the spherical nanoparticle suspension is higher concentration (116 picomolar) than our nanohelix suspensions ($\approx$ 20 picomolar), and the scattering cross section can vary significantly with shape. Therefore, the following results should not be directly compared to those obtained for nanohelices. The HRS intensity in this configuration is shown in figure 7.7. For P-polarised incident light, the analyser sweep shows a sinusoidal intensity curve, clearly showing a linearly polarised output. However, under S-polarised illumination, the measured signal reduces to near zero. This is because the nanospheres scatter in a dipole pattern originating from surface charge oscillations along the polarisation axis of incident light. In our experimental configuration, no dipole emission will propagate in the direction of the detector under S-polarised illumination. Conversely, P-polarised illumination will drive dipolar scattering with a P-polarised component in the direction of the detector. This data verifies one important aspect of the nanohelix samples: The helical geometry provides intrinsic chirality, however the helical axis acts, to some extent, as a rod. In this case, the nanohelices scatter in a dipole pattern originating from surface charge oscillations *along the helical axis*, with an amplitude related to the angle between the helical axis, and the angle of incident polarisation. This results in a depolarisation effect, in which light is scattered equally at all polarisation angles due to the random orientation of the nanohelices, as observed in figure 7.6b.

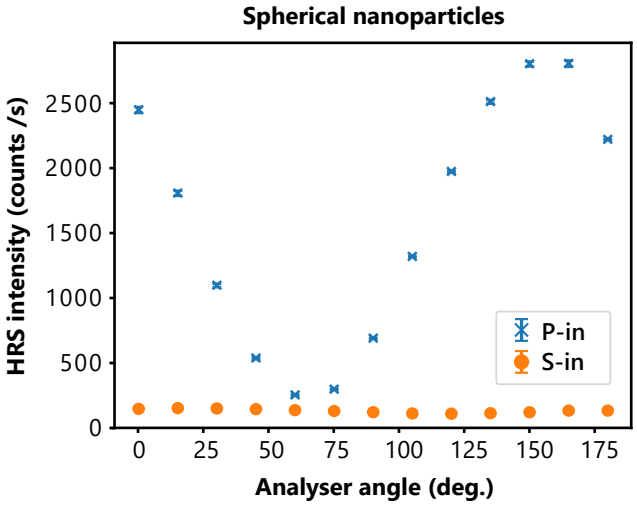

Figure 7.7: *HRS intensity from Ag nanospheres at* 360 nm*, under P-polarised (blue crosses) and S-polarised (orange dots)* 720 nm *illumination, as the analysing polariser is rotated. P-polarised illumination results in linearly polarised emission, whereas S-polarised illumination results in almost zero intensity, both consistent with dipolar emission originating from charge oscillations in the direction of incident polarisation.*

7.3 Discussion

Within the electric dipole approximation, the second-order induced polarisation of a single scatterer is described by the hyperpolarisability tensor β_{ijk}. This tensor is similar in nature

to the second-order susceptibility tensor discussed in section 3.2, and relates the induced polarisation of the particle μ_i to a driving electric field by $\mu_i(2\omega) = \epsilon_0 \beta_{ijk} E_j(\omega) E_k(\omega)$. For a single scatterer, the HRS intensity is thus proportional to the square of the hyperpolarisability tensor β^2_{ijk}. In liquid suspensions, the total measured HRS intensity originates from the incoherent sum of randomly oriented scatterers within the illumination volume. The measured HRS intensity is thus proportional to the rotational average of the square of the hyperpolarisability tensor $\langle I(2\omega) \rangle \propto \langle \beta^2 \rangle$. In a homogeneous suspension of structurally isotropic particles, HRS is forbidden within this electric dipole approximation. By acting on the hyperpolarisability tensor with rotation matrices for all 3 axes and equating to the unrotated tensor for any arbitrary rotation (thus enforcing true 3D isotropy), every component of the hyperpolarisability tensor reduces to zero.

In these experiments however, the individual nanostructures are anisotropic, but randomly oriented on average. During a single laser pulse, and over the sample volume, there will exist slight deviations from perfect average isotropy, an "anisotropic excess". The anisotropic excess prevents HRS from completely cancelling out, allowing for non-zero signal during that pulse, with intensity and polarisation dependent on the orientation of the anisotropic excess. By integrating over many pulses (our 30 second counting window), the orientational dependence of the HRS is averaged out, and general structural information can be obtained. Mathematically, the averaging process is equivalent to integrating the HRS intensity from a single structure over all orientations, and can be described in terms of the normalised triple integral:

$$\langle I(2\omega) \rangle \propto \left(\frac{1}{2\pi} \right)^3 \int_0^{2\pi} \int_0^{2\pi} \int_0^{2\pi} \beta'^2_{ijk}(\theta, \phi, \psi) d\theta d\phi d\psi \tag{7.2}$$

Note that this is different to symmetrising the tensor, which involves integrating β, rather than β^2. Similar to chapter 6, $\beta'_{ijk}(\theta, \phi, \psi)$ describes an effective hyperpolarisability tensor after rotation about the z, y, and x axis by angles θ, ϕ, and ψ respectively. In full tensor notation this is described in terms of the rotation matrices by (given in section 3.2.4) by

$$\begin{aligned} \beta^{(2)\prime}_{ijk}(\theta, \phi, \psi) = & R^x(\psi)_{i\alpha} R^x(\psi)_{j\beta} R^x(\psi)_{k\gamma} \\ & R^y(\phi)_{i\alpha} R^y(\phi)_{j\beta} R^y(\phi)_{k\gamma} \\ & R^z(\theta)_{i\alpha} R^z(\theta)_{j\beta} R^z(\theta)_{k\gamma} \beta^{(2)}_{\alpha\beta\gamma} \end{aligned} \tag{7.3}$$

Applying parity inversion to the hyperpolarisability tensor using a reflection matrix A_{ij}, and performing the same averaging operation, produces an identical non-zero expression. While non-zero HRS is permitted, HRS-CID is forbidden within the electric dipole approximation. Surprisingly, clear HRS-CID was nevertheless experimentally observed. This strongly suggests that our nanohelix structures should not simply be treated as point-like scatterers described by hyperpolarisability tensors. Previous work has outlines two models for the nonlinear optical activity of chiral molecules, in terms of dominant magnetic dipole contributions, and dominant chirally-coupled electric dipole contributions [157]. By considering our nanohelix structures in the context of these molecular models, two potential origins of the observed HRS-CID are proposed.

The first potential origin is if the nanohelices do not behave as a point scatterers. The nanohelix wire thickness is comparable to the materials skin depth, however the helix dimensions overall are significantly larger than this. Therefore, an individual helix can be modelled as a helical arrangement of oscillating achiral point-dipoles. These oscillating dipoles will be chirally coupled, and phase-retardation effects across the span of the helix, due to the chiral arrangement, can lead to a measurable HRS-CD. Importantly, this description can be considered in terms of the nonlinear extension to Kuhn's coupled oscillator model of molecular chirality [157]. The second potential origin is from higher-order contributions to HRS than electric dipoles. We have established that the signal is not of electric quadrupolar origin, from the results presented in figure 7.6b. However, magnetic-dipole contributions can not be ruled out by these results. In chapter 6 we disregarded the magnetic dipole contribution to nonlinear emission as negligible, primarily due to the orientation of helices relative to the incident light. In this experimental configuration however, this is not the case. The helical structure acts as a conductive coil. Driving current along the length of the helix will induce a magnetic field parallel to the induced electric dipole. Now, the magnetic-dipole electric-dipole contribution to nonlinear emission cannot be considered negligible, and this contribution permits HRS-CID. The overall HRS signal would, in this case, be described by an electric dipole contribution exhibiting no CID, and a magnetic-dipole contribution from which the CID originates. Interestingly, this description can be considered in terms of the nonlinear extension to the one-electron on a helix model of molecular chirality [157]. While outside of the scope of this work, it may be possible to distinguish between the two models by measuring optical rotation effects in second-harmonic scattering, as optical rotation is permitted only in the chirally-coupled dipole description of nonlinear emission [157].

For the purposes of comparison to the linear CD spectra, we can characterise the HRS-CD by a polarisation ellipticity:

$$\theta^{HRS}(\text{deg.}) = \frac{180}{\pi} \tan\left(\frac{\sqrt{I^{HRS}_{RCP}} - \sqrt{I^{HRS}_{LCP}}}{\sqrt{I^{HRS}_{RCP}} + \sqrt{I^{HRS}_{LCP}}}\right). \tag{7.4}$$

Here, I^{HRS}_{RCP} and I^{HRS}_{LCP} are the electric field intensities of light scattered at the second harmonic for RCP and LCP illumination, respectively. The measured linear and HRS ellipticities are given in table 7.1. Note that in these data the linear- and HRS-CD are expected to have an opposite sign, due to experimental geometry. Table 7.1 indicates that the measured HRS-CD effect is 3 to 4 times stronger than the linear CD across the range of wavelengths studied. However, when considering the volume of the liquid interacting with incident light, the HRS-CD effect appears significantly more sensitive than its linear counterpart. For a Gaussian beam, at a position z from the focus, with a beam waist w_0 and a Rayleigh range $z(r)$, the beam radius $w(z)$ is given by $w(z) = w_0\sqrt{1 + (z/z_R)^2}$. We define the beam volume as the integral of the spot area $\pi w(z)^2$ between two positions z_i

	Fundamental wavelength (nm)	Linear ellipticity (mdeg.)	HRS ellipticity (mdeg.)
Right-handed helices	720	920	-3299
	740	803	-3356
	780	569	-1890
Left-handed helices	720	-370	1811
	740	-293	1455
	780	-164	1334

Table 7.1: *Linear and HRS ellipticities for left- and right-handed nanohelix suspensions. Values are given at the three fundamental wavelengths used in the HRS experiments.*

(initial) and z_f (final) as:

$$V_{beam} = \int_{z_i}^{z_f} \pi \left({w_0}^2 \sqrt{1 + (z/z_R)^2} \right)^2 dz. \tag{7.5}$$

For these experiments, we assume that significant HRS occurs within the Rayleigh range of the fundamental beam, and so the effective interaction volume is given by V_{beam} integrated between $-z_R$ and z_R. Considering the 10 cm focal length lens used in our experiments, with an incident beam of waist 1.2 mm and $\lambda = 740$ nm fundamental light, the waist at the focus $w_f = (\lambda f)/(\pi w_0)$ is found to be ≈ 20 µm, with a Rayleigh range of ≈ 2 mm. From this, we assume that we measure HRS from a 4 mm path length through the cuvette. The effective beam volume (V_{beam}) is then $\approx 10^{-11}\text{m}^3$ ($= 10$ nl). By comparison, the commercial CD spectrometer uses a 10 mm optical path length with an approximately constant beam radius of ≈ 1 mm, giving an effective beam volume of $\approx 10^{-6}\text{m}^3$ ($= 1$ ml). This value is 5 orders of magnitude larger compared to the nonlinear case. Consequently, the HRS-CD effect is significantly more sensitive than its linear counterpart.

7.4 Conclusions

We have demonstrated the first observation of HRS-CD, by measuring multiphoton scattering spectra from a low concentration isotropic suspension of Ag nanohelices in water. Although complete macroscopic isotropy would forbid HRS, over the time scale of ultrashort laser pulses, and the low interaction volume used, deviations from perfect isotropy allow the chirality of the helices to be probed. In this sense, low concentrations of nanoparticles may in fact be an advantage. Low particle concentrations, and small interaction volumes, are more statistically likely to deviate from perfect isotropy, and over long counting windows, these deviations sum to give a measurable probe of intrinsic chirality.

This technique therefore allows pure chiral symmetry information to be obtained from extremely low concentrations of nanostructures suspended in low volumes of liquid. The range of available miniaturised cuvettes, narrow capillaries, microfluidic channels and hollow-core optical fibres position this new chiroptical characterisation directly within the lab-on-a-chip paradigm. Additionally, since plasmonic nanoparticles can be leveraged to increase the chiroptical response of molecules, this technology potentially allows the

miniaturised characterisation of synthesised chemicals.

Chapter 8

Summary and Conclusions

With the availability of modern nanofabrication techniques, chiral plasmonic nanomaterials, in particular, have opened up the field of nanophotonics to a wide range of novel devices. By optimising structural chirality parameters, negative index metamaterials have been realised, with applications in sub-wavelength imaging. Similar effects have also been utilised for ultra-thin polarisation optics. Perhaps more surprisingly, chiral plasmonic devices have also introduced a new platform for nanorobotics. Key to perhaps more humanitarian applications however is the possibility to realise new, sensitive chemical characterisation techniques for the pharmaceutical and biochemistry industries.

Development within these research areas, and more, has been rapidly accelerated by advances in nanofabrication, and the unparalleled freedom that comes with the use of nanomaterials. The fabrication of novel nanomaterial geometries directly lifts limits on the optical effects available for exploration. In many cases however, the diversity of characterisation experiments has not yet matched the diversity of material geometries available: many "off-the-shelf" experimental techniques are not necessarily perfectly suited to the characterisation of particular nanomaterial geometries. This work has focused on developing experimental techniques designed for the characterisation of chiral nanomaterials fabricated by our collaborators, by specifically considering the unique properties of each, and the experimental challenges these properties may present.

Common to each of the samples studied is the comprehensive use of second-harmonic nonlinear optical effects as probes for chirality. Second-harmonic chiroptical effects have been shown to function as highly sensitive probes for chirality, due to the symmetry sensitivity of second-harmonic generation. In experiments characterising chiral structures within an achiral background, SHG is generally forbidden from the achiral bulk, thus providing intrinsic background reduction. Furthermore, and contrary to linear optical counterparts, SHG chiroptical effects are permitted within the electric dipole approximation, providing entirely new information due to their fundamentally different physical origin. By utilising these various enhancements, we have demonstrated a set of analysis techniques for three very different chiral plasmonic nanomaterials.

Plasmonic structure arrays with dimensions comparable to the wavelength of light can support higher-order plasmon modes, whose spatial profiles directly relate to the material geometry. We have shown that by examining intermediate geometries between opposite

enantiomorphs, unexpected optical behaviour can be observed. Electric field hotspots form at the centre of our chiral cross structures, originating from higher-order hybridised plasmon modes of the coupled nanostripes composing the crosses. Structural chirality directly leads to a circular difference in the hotspot intensity, which was measured using SHG microscopy. By considering modal decompositions of the total plasmonic responses, new avenues for chiroptical optimisation are opened. By tuning the structure geometry, or introducing auxiliary processes that modify the coupling strengths of specific modes, the chiroptical response can be enhanced by suppressing contributions from the "wrong" modes.

In many such planar nanomaterials, structural anisotropy can "dilute" chiroptical measurements, making it difficult to extract pure chiral information over contributions from anisotropy. Previous work has shown that in a helical metamaterial, nonlinear circular intensity difference effects are dominated by structural anisotropy. By instead measuring SHG optical rotation from same helical metamaterial, we have shown that, under specific experimental conditions, it is possible to obtain a chiroptical response that provides separable information about chirality and anisotropy. The conditions depend strongly on both the nanomaterial geometry, and the illumination conditions. Changing, for instance, the polarisation of incident light resulted in a response completely dominated by anisotropy, with no separable chiral information available. Nevertheless, the work demonstrated, for the first time, SHG optical rotation from a chiral metamaterial, which can be exclusively attributed to intrinsic chirality. Carefully selecting the experimental geometry for a particular sample geometry can generally allow for more comprehensive chiral characterisation of anisotropic metamaterials in the future.

Finally, we examined the case of intrinsically removing anisotropy from the experimental system, by suspending randomly oriented silver nanohelices in liquid. In our previous experiments, nonlinear chiroptical effects could be measured by detecting SHG in a reflection geometry. For liquid samples, we employed a hyper-Rayleigh scattering (HRS) geometry, to measure the circular difference in second-harmonic scattering of incident light. Strong HRS circular intensity difference was observed at three different incident wavelengths, well above background. Within the electric dipole approximation, HRS-CID is symmetry forbidden. Our observations can be explained by both magnetic dipole contributions to HRS, and the helices behaving as helical arrangements of coupled dipoles, rather than as point scatterers themselves. Future experiments outside of the scope of this thesis may be able to determine the dominant of these contributions to the observed HRS-CID. In this work we have nevertheless reported the first experimental observation of HRS-CID in a liquid sample, providing pure chiral information independent of the individual nanohelices anisotropy.

As our understanding of chirality in nanophotonics develops, and nanofabrication techniques open up even more design flexibility, it should be expected that the need for tailored characterisation experiments will blossom. It seems only reasonable that the freedom and creativity permitted by modern nanofabrication should be matched by novel detection and characterisation schemes. Throughout this project, we have demonstrated a range of techniques designed to reveal previously unobserved behaviour from particular nanomaterial

samples. By more fully exploiting the level of freedom permitted by such systems, the field of chiral nanophotonics will no doubt benefit from specially tailored characterisation techniques in the future, allowing for more rapid design, characterisation, and enhancement of chiral optical nanomaterials.

Bibliography

[1] J. T. Collins, K. R. Rusimova, D. C. Hooper, H.-H. Jeong, L. Ohnoutek, F. Pradaux-Caggiano, T. Verbiest, D. Carbery, P. Fischer, and V. K. Valev, "First observation of optical activity in hyper-Rayleigh scattering," *Phys. Rev. X*, 2019. Accepted.

[2] S. W. Lovesey, J. T. Collins, and S. P. Collins, "Superchiral photons unveil magnetic circular dichroism," *Phys. Rev. B*, 2018. Submitted.

[3] K. R. Rusimova, D. Slavov, F. Pradaux-Caggiano, D. Carbery, J. T. Collins, S. Gordeev, W. J. Wadsworth, P. J. Mosley, and V. K. Valev, "Atomic dispensers: thermoplasmonic control of alkali vapor pressure for quantum optical applications," *Nature Communications*, 2018. Submitted.

[4] J. T. Collins, D. C. Hooper, A. G. Mark, C. Kuppe, and V. K. Valev, "Second-Harmonic Generation Optical Rotation Solely Attributable to Chirality in Plasmonic Metasurfaces," *ACS Nano*, p. 8b00601, June 2018.

[5] C. Kuppe, C. Williams, J. You, J. T. Collins, S. N. Gordeev, T. D. Wilkinson, N.-C. Panoiu, and V. K. Valev, "Circular Dichroism in Higher-Order Diffraction Beams from Chiral Quasiplanar Nanostructures," *Advanced Optical Materials*, vol. 6, p. 1800098, June 2018.

[6] J. T. Collins, X. Zheng, N. V. S. Braz, E. Slenders, S. Zu, G. A. E. Vandenbosch, V. V. Moshchalkov, Z. Fang, M. Ameloot, P. A. Warburton, and V. K. Valev, "Enantiomorphing Chiral Plasmonic Nanostructures: A Counterintuitive Sign Reversal of the Nonlinear Circular Dichroism," *Advanced Optical Materials*, vol. 1800153, p. 1800153, May 2018.

[7] J. T. Collins, C. Kuppe, D. C. Hooper, C. Sibilia, M. Centini, and V. K. Valev, "Chirality and Chiroptical Effects in Metal Nanostructures: Fundamentals and Current Trends," *Advanced Optical Materials*, vol. 5, p. 1700182, Aug. 2017.

[8] D. C. Hooper, A. G. Mark, C. Kuppe, J. T. Collins, P. Fischer, and V. K. Valev, "Strong Rotational Anisotropies Affect Nonlinear Chiral Metamaterials," *Advanced Materials*, vol. 29, p. 1605110, Apr. 2017.

[9] W. T. Kelvin, "The molecular tactics of a crystal," *Clarendon Press*, 1894.

[10] L. Barron, "True and false chirality and parity violation," *Chemical Physics Letters*, vol. 123, no. 5, pp. 423 – 427, 1986.

[11] N. Vargesson, "Thalidomide-induced teratogenesis: History and mechanisms," 2015.

[12] J. E. Mendelson, D. McGlothlin, D. S. Harris, E. Foster, T. Everhart, P. Jacob, and R. T. Jones, "The Clinical Pharmacology of Intranasal l-Methamphetamine," *BMC Clinical Pharmacology*, vol. 8, p. 4, Dec. 2008.

[13] T. Nishimura, K. Takahata, Y. Kosugi, T. Tanabe, and S. Muraoka, "Psychomotor effect differences between l-methamphetamine and d-methamphetamine are independent of murine plasma and brain pharmacokinetics profiles," *Journal of Neural Transmission*, vol. 124, pp. 519–523, May 2017.

[14] R. Craven, "Ketamine," *Anaesthesia*, vol. 62, pp. 48–53, Dec. 2007.

[15] J. Muller, S. Pentyala, J. Dilger, and S. Pentyala, "Ketamine enantiomers in the rapid and sustained antidepressant effects," *Therapeutic Advances in Psychopharmacology*, vol. 6, pp. 185–192, June 2016.

[16] H. Ulrich Zeilhofer, D. Swandulla, G. Geisslinger, and K. Brune, "Differential effects of ketamine enantiomers on NMDA receptor currents in cultured neurons," *European Journal of Pharmacology*, vol. 213, pp. 155–158, Mar. 1992.

[17] L. A. Nguyen, H. He, and C. Pham-Huy, "Chiral drugs: an overview," *International journal of biomedical science : IJBS*, vol. 2, pp. 85–100, June 2006.

[18] C. Rizza, A. Di Falco, M. Scalora, and A. Ciattoni, "One-Dimensional Chirality: Strong Optical Activity in Epsilon-Near-Zero Metamaterials," *Physical Review Letters*, vol. 115, p. 057401, July 2015.

[19] M. Esposito, V. Tasco, F. Todisco, M. Cuscunà, A. Benedetti, M. Scuderi, G. Nicotra, and A. Passaseo, "Programmable Extreme Chirality in the Visible by Helix-Shaped Metamaterial Platform," *Nano Letters*, vol. 16, pp. 5823–5828, Sept. 2016.

[20] Y. Hou, H. M. Leung, C. T. Chan, J. Du, H. L. W. Chan, and D. Y. Lei, "Ultrabroadband Optical Superchirality in a 3D Stacked-Patch Plasmonic Metamaterial Designed by Two-Step Glancing Angle Deposition," *Advanced Functional Materials*, vol. 26, no. 43, pp. 7807–7816, 2016.

[21] M. J. J. Urban, C. Zhou, X. Duan, and N. Liu, "Optically Resolving the Dynamic Walking of a Plasmonic Walker Couple," *Nano Letters*, vol. 15, pp. 8392–8396, Dec. 2015.

[22] D. Schamel, M. Pfeifer, J. G. Gibbs, B. Miksch, A. G. Mark, and P. Fischer, "Chiral Colloidal Molecules And Observation of The Propeller Effect," *Journal of the American Chemical Society*, vol. 135, pp. 12353–12359, Aug. 2013.

[23] E. Hecht, *Optics: Pearson New International Edition*, vol. 1. Pearson Higher Ed USA, 4th ed., 2013.

[24] W. W. Parson, *Modern Optical Spectroscopy*, vol. 1. Berlin, Heidelberg: Springer Berlin Heidelberg, 2007.

[25] M. Fox, "Optical properties of solids," 2002.

[26] A. Ishimaru, S. W. Lee, Y. Kuga, and V. Jandhyala, "Generalized Constitutive Relations for Metamaterials Based on the Quasi-Static Lorentz Theory," *IEEE Transactions on Antennas and Propagation*, vol. 51, no. 10 I, pp. 2550–2557, 2003.

[27] F. Capolino, *Theory and Phenomena of Metamaterials*, vol. 8. CRC Press, Oct. 2009.

[28] J. Lekner, "Optical properties of isotropic chiral media," *Pure and Applied Optics: Journal of the European Optical Society Part A*, vol. 5, no. November 1994, pp. 417–443, 1999.

[29] S. M. Barnett and R. P. Cameron, "Energy conservation and the constitutive relations in chiral and non-reciprocal media," *Journal of Optics*, vol. 18, p. 015404, Jan. 2016.

[30] J. A. A. Kong, *Electromagnetic Wave Theory*. New York: Wiley, 1st ed. ed., 1986.

[31] I. V. Lindell, A. H. Sihvola, S. Tretyakov, and A. Viitanen, *Electromagnetic Waves in Chiral and Bi-isotropic Media*. Norwood, United States: Artech House, 1994.

[32] R.-L. Chern, "Wave propagation in chiral media: composite fresnel equations," *Journal of Optics*, vol. 15, no. 7, p. 075702, 2013.

[33] C.-W. Qiu, N. Burokur, S. Zouhd, and L.-W. Li, "Chiral nihility effects on energy flow in chiral materials.," *Journal of the Optical Society of America. A, Optics, image science, and vision*, vol. 25, no. 1, pp. 55–63, 2008.

[34] V. K. Valev, J. J. Baumberg, C. Sibilia, and T. Verbiest, "Chirality and Chiroptical Effects in Plasmonic Nanostructures: Fundamentals, Recent Progress, and Outlook," *Advanced Materials*, vol. 25, pp. 2517–2534, May 2013.

[35] J. B. B. Pendry, "A Chiral Route to Negative Refraction," *Science*, vol. 306, pp. 1353–1355, Nov. 2004.

[36] P. Atkins and J. De Paula, *Physical Chemistry*. OUP Oxford, 8th ed., 2010.

[37] J. A. Schellman, "Circular Dichroism and Optical Rotation," *Chemical Reviews*, 1975.

[38] P. L. Polavarapu, "Kramers-Kronig transformation for optical rotatory dispersion studies," *Journal of Physical Chemistry A*, 2005.

[39] E. Plum, V. A. A. Fedotov, and N. I. I. Zheludev, "Asymmetric transmission: a generic property of two-dimensional periodic patterns," *Journal of Optics*, vol. 13, no. 2, p. 024006, 2011.

[40] E. Plum, X.-X. Liu, V. A. Fedotov, Y. Chen, D. P. Tsai, and N. I. Zheludev, "Metamaterials: Optical Activity without Chirality," *Physical Review Letters*, vol. 102, p. 113902, Mar. 2009.

[41] B. M. Maoz, A. Ben Moshe, D. Vestler, O. Bar-Elli, and G. Markovich, "Chiroptical Effects in Planar Achiral Plasmonic Oriented Nanohole Arrays," *Nano Letters*, vol. 12, pp. 2357–2361, May 2012.

[42] T. Cao, C. Wei, L. Mao, and Y. Li, "Extrinsic 2D chirality: giant circular conversion dichroism from a metal-dielectric-metal square array," *Scientific Reports*, vol. 4, p. 7442, 2014.

[43] A. Belardini, M. Centini, G. Leahu, D. C. Hooper, R. Li Voti, E. Fazio, J. W. Haus, A. Sarangan, V. K. Valev, and C. Sibilia, "Chiral light intrinsically couples to extrinsic/pseudo-chiral metasurfaces made of tilted gold nanowires," *Scientific Reports*, vol. 6, p. 31796, Aug. 2016.

[44] A. Belardini, M. Centini, G. Leahu, E. Fazio, C. Sibilia, J. W. W. Haus, and A. Sarangan, "Second harmonic generation on self-assembled tilted gold nanowires.," *Faraday discussions*, vol. 178, pp. 357–62, Jan. 2015.

[45] N. Berova, P. L. L. Polavarapu, K. Nakanishi, and R. W. W. Woody, *Comprehensive Chiroptical Spectroscopy*, vol. 2. Hoboken: John Wiley & Sons, Inc., Feb. 2012.

[46] S. Hashiyada, T. Narushima, and H. Okamoto, "Imaging Chirality of Optical Fields near Achiral Metal Nanostructures Excited with Linearly Polarized Light," *ACS Photonics*, vol. 5, pp. 1486–1492, Apr. 2018.

[47] Y. Tang and A. E. Cohen, "Optical Chirality and Its Interaction with Matter," *Physical Review Letters*, vol. 104, p. 163901, Apr. 2010.

[48] D. M. Lipkin, "Existence of a New Conservation Law in Electromagnetic Theory," *Journal of Mathematical Physics*, vol. 5, no. 5, p. 696, 1964.

[49] M. M. Coles and D. L. Andrews, "Chirality and angular momentum in optical radiation," *Physical Review A - Atomic, Molecular, and Optical Physics*, vol. 85, no. 6, pp. 1–7, 2012.

[50] Y. Tang and A. E. Cohen, "Enhanced enantioselectivity in excitation of chiral molecules by superchiral light.," *Science (New York, N.Y.)*, vol. 332, no. 6027, pp. 333–336, 2011.

[51] J. S. Choi and M. Cho, "Limitations of a superchiral field," *Physical Review A - Atomic, Molecular, and Optical Physics*, vol. 86, no. 6, pp. 1–22, 2012.

[52] A. Sinibaldi, A. Fieramosca, R. Rizzo, A. Anopchenko, N. Danz, P. Munzert, C. Magistris, C. Barolo, and F. Michelotti, "Combining label-free and fluorescence operation of Bloch surface wave optical sensors," *Opt. Lett.*, vol. 39, no. 10, pp. 2947–2950, 2014.

[53] G. Pellegrini, M. Finazzi, M. Celebrano, L. Duò, and P. Biagioni, "Chiral surface waves for enhanced circular dichroism," *Physical Review B*, vol. 95, no. 24, pp. 1–5, 2017.

[54] G. Pellegrini, M. Finazzi, M. Celebrano, L. Duò, and P. Biagioni, "Surface-enhanced chiroptical spectroscopy with superchiral surface waves," *Chirality*, vol. 30, pp. 883–889, July 2018.

[55] D. J. Griffiths, *Introduction to Electrodynamics*. No. 1, Pearson, 3 ed., 2013.

[56] R. W. Boyd, *Nonlinear Optics, 3rd Edition*. Academic Press, 2008.

[57] T. Verbiest, K. Clays, and V. Rodriguez, *Second-order Nonlinear Optical Characterization Techniques: An Introduction*. CRC Press, second edi ed., 2009.

[58] C. L. Tang, "Nonlinear Optics," in *Handbook of Optics* (M. Bass, E. W. Van Stryland, D. R. Williams, and W. L. Wolfe, eds.), ch. 38, pp. 38.1 – 38.26, New York: OSA/McGraw-Hill, 1995.

[59] S. V. Popov, Y. P. Svirko, and N. I. Zheludev, *Susceptibility Tensors for Nonlinear Optics*. CRC Press, 1995.

[60] L. D. Barron, *Molecular Light Scattering and Optical Activity*. Cambridge: Cambridge University Press, 2004.

[61] J. D. Byers, H. I. Yee, and J. M. Hicks, "A second harmonic generation analog of optical rotatory dispersion for the study of chiral monolayers," *The Journal of Chemical Physics*, vol. 101, no. 7, p. 6233, 1994.

[62] A.-M. Pena, T. Boulesteix, T. Dartigalongue, M. Strupler, E. Beaurepaire, and M.-C. Schanne-Klein, "Chiroptical effects in the second harmonic generation from collagens I and IV: Applications in nonlinear microscopy," *Nonlinear Optics Quantum Optics*, vol. 35, no. 1-3, pp. 235–240, 2006.

[63] T. Petralli-Mallow, T. M. Wong, J. D. Byers, H. I. Yee, and J. M. Hicks, "Circular dichroism spectroscopy at interfaces: a surface second harmonic generation study," *The Journal of Physical Chemistry*, vol. 97, pp. 1383–1388, Feb. 1993.

[64] J. D. Byers, H. I. Yee, T. Petralli-Mallow, and J. M. Hicks, "Second-harmonic generation circular-dichroism spectroscopy from chiral monolayers," *Physical Review B*, vol. 49, pp. 14643–14647, May 1994.

[65] T. Verbiest, M. Kauranen, A. Persoons, M. Ikonen, J. Kurkela, and H. Lemmetyinen, "Nonlinear Optical Activity and Biomolecular Chirality," *Journal of the American Chemical Society*, vol. 116, no. 20, pp. 9203–9205, 1994.

[66] K. Fujiwara, H. Monjushiro, and H. Watarai, "Non-linear optical activity of porphyrin aggregate at the liquid/liquid interface," *Chemical Physics Letters*, vol. 394, pp. 349–353, Aug. 2004.

[67] P. Campagnola, "Second Harmonic Generation Imaging Microscopy: Applications to Diseases Diagnostics," *Analytical Chemistry*, vol. 83, pp. 3224–3231, May 2011.

[68] H. Lee, M. J. Huttunen, K.-J. Hsu, M. Partanen, G.-Y. Zhuo, M. Kauranen, and S.-W. Chu, "Chiral imaging of collagen by second-harmonic generation circular dichroism," *Biomedical Optics Express*, vol. 4, p. 909, June 2013.

[69] K. R. Campbell and P. J. Campagnola, "Wavelength-dependent Second Harmonic Generation Circular Dichroism for Differentiation of Col I and Col III Isoforms in Stromal Models of Ovarian Cancer," in *Biomedical Optics 2016*, vol. 2016, (Washington, D.C.), p. JM3A.35, OSA, 2016.

[70] X. Chen, C. Raggio, and P. J. Campagnola, "Second-harmonic generation circular dichroism studies of osteogenesis imperfecta," *Optics Letters*, vol. 37, p. 3837, Sept. 2012.

[71] M. J. Huttunen, G. Bautista, M. Decker, S. Linden, M. Wegener, and M. Kauranen, "Nonlinear chiral imaging of twisted-cross gold nano-objects," *2011 Conference on Lasers and Electro-Optics Europe and 12th European Quantum Electronics Conference, CLEO EUROPE/EQEC 2011*, vol. 1, no. 1, pp. 2501–2503, 2011.

[72] V. K. Valev, "Characterization of nanostructured plasmonic surfaces with second harmonic generation.," *Langmuir : the ACS journal of surfaces and colloids*, vol. 28, pp. 15454–15471, Nov. 2012.

[73] E. A. Mamonov, A. I. Maydykovskiy, I. A. Kolmychek, S. A. Magnitskiy, and T. V. Murzina, "Polarization-resolved second harmonic generation microscopy of chiral G-shaped metamaterials," *Physical Review B*, vol. 96, no. 7, p. 075408, 2017.

[74] A. Guerrero-Martínez, B. Auguié, J. L. Alonso-Gómez, Z. Džolić, S. Gómez-Graña, M. Žinić, M. M. Cid, and L. M. Liz-Marzán, "Intense Optical Activity from Three-Dimensional Chiral Ordering of Plasmonic Nanoantennas," *Angewandte Chemie International Edition*, vol. 50, pp. 5499–5503, June 2011.

[75] A. Belardini, A. Benedetti, M. Centini, G. Leahu, F. Mura, S. Sennato, C. Sibilia, V. Robbiano, M. C. Giordano, C. Martella, D. Comoretto, and F. B. de Mongeot, "Second Harmonic Generation Circular Dichroism from Self-Ordered Hybrid Plasmonic-Photonic Nanosurfaces," *Advanced Optical Materials*, vol. 2, pp. 208–213, Mar. 2014.

[76] S. A. Maier, *Plasmonics: Fundamentals and Applications*. Boston, MA: Springer US, Sept. 2007.

[77] S. Roh, T. Chung, and B. Lee, "Overview of the Characteristics of Micro- and Nano-Structured Surface Plasmon Resonance Sensors," *Sensors*, vol. 11, pp. 1565–1588, Jan. 2011.

[78] E. Petryayeva and U. J. Krull, "Localized surface plasmon resonance: Nanostructures, bioassays and biosensing-A review," *Analytica Chimica Acta*, vol. 706, no. 1, pp. 8–24, 2011.

[79] L. Polavarapu, J. Pérez-Juste, Q.-H. Xu, and L. M. Liz-Marzán, "Optical sensing of biological, chemical and ionic species through aggregation of plasmonic nanoparticles," *Journal of Materials Chemistry C*, vol. 2, no. 36, pp. 7460–7476, 2014.

[80] F. Cheng, X. Yang, and J. Gao, "Ultrasensitive detection and characterization of molecules with infrared plasmonic metamaterials.," *Scientific reports*, vol. 5, p. 14327, 2015.

[81] R. A. Dynich and A. N. Ponyavina, "Effect of metallic nanoparticle sizes on the local field near their surface," *Journal of Applied Spectroscopy*, vol. 75, pp. 832–838, Nov. 2008.

[82] K. Tanabe, "Field Enhancement around Metal Nanoparticles and Nanoshells: A Systematic Investigation," *The Journal of Physical Chemistry C*, vol. 112, pp. 15721–15728, Oct. 2008.

[83] E. C. Dreaden, R. D. Near, T. Abdallah, M. H. Talaat, and M. A. El-Sayed, "Multimodal plasmon coupling in low symmetry gold nanoparticle pairs detected in surface-enhanced Raman scattering," *Applied Physics Letters*, vol. 98, no. 18, pp. 96–99, 2011.

[84] B. Lee, I. M. Lee, S. Kim, D. H. Oh, and L. Hesselink, "Review on subwavelength confinement of light with plasmonics," *Journal of Modern Optics*, vol. 57, no. 16, pp. 1479–1497, 2010.

[85] V. K. Valev, D. Denkova, X. Zheng, A. I. Kuznetsov, C. Reinhardt, B. N. Chichkov, G. Tsutsumanova, E. J. Osley, V. Petkov, B. De Clercq, A. V. Silhanek, Y. Jeyaram, V. Volskiy, P. A. Warburton, G. A. E. Vandenbosch, S. Russev, O. A. Aktsipetrov, M. Ameloot, V. V. Moshchalkov, and T. Verbiest, "Plasmon-Enhanced Sub-Wavelength Laser Ablation: Plasmonic Nanojets," *Advanced Materials*, vol. 24, pp. OP29–OP35, Mar. 2012.

[86] J. R. Krenn, J. C. Weeber, a. Dereux, E. Bourillot, J. P. Goudonnet, B. Schider, a. Leitner, and F. R. Aussenegg, "Direct observation of localized surface plasmon coupling," *Physical Review B (Condensed Matter and Materials Physics)*, vol. 60, no. 7, p. 5029, 1999.

[87] J. R. Krenn, A. Dereux, J. C. Weeber, E. Bourillot, Y. Lacroute, J. P. Goudonnet, G. Schider, W. Gotschy, A. Leitner, F. R. Aussenegg, and C. Girard, "Squeezing the optical near-field zone by plasmon coupling of metallic nanoparticles," *Physical Review Letters*, vol. 82, no. 12, pp. 2590–2593, 1999.

[88] Y. Huang, L. Ma, M. Hou, J. Li, Z. Xie, and Z. Zhang, "Hybridized plasmon modes and near-field enhancement of metallic nanoparticle-dimer on a mirror," *Scientific Reports*, vol. 6, p. 30011, Sept. 2016.

[89] J. Lee, S. Sung, J.-H. Choi, S. C. Eom, N. A. Mortensen, and J. H. Shin, "Ultra sub-wavelength surface plasmon confinement using air-gap, sub-wavelength ring resonator arrays," *Scientific Reports*, vol. 6, p. 22305, Apr. 2016.

[90] V. K. Valev, A. V. Silhanek, Y. Jeyaram, D. Denkova, B. De Clercq, V. Petkov, X. Zheng, V. Volskiy, W. Gillijns, G. A. E. Vandenbosch, O. A. Aktsipetrov, M. Ameloot, V. V. Moshchalkov, and T. Verbiest, "Hotspot Decorations Map Plasmonic Patterns with the Resolution of Scanning Probe Techniques," *Physical Review Letters*, vol. 106, p. 226803, June 2011.

[91] S. Nie, "Probing Single Molecules and Single Nanoparticles by Surface-Enhanced Raman Scattering," *Science*, vol. 275, pp. 1102–1106, Feb. 1997.

[92] D. P. Fromm, A. Sundaramurthy, A. Kinkhabwala, P. J. Schuck, G. S. Kino, and W. E. Moerner, "Exploring the chemical enhancement for surface-enhanced Raman scattering with Au bowtie nanoantennas," *The Journal of Chemical Physics*, vol. 124, p. 061101, Feb. 2006.

[93] E. C. Le Ru, E. Blackie, M. Meyer, and P. G. Etchegoin, "Surface Enhanced Raman Scattering Enhancement Factors: A Comprehensive Study," *The Journal of Physical Chemistry C*, vol. 111, pp. 13794–13803, Sept. 2007.

[94] C. E. Talley, J. B. Jackson, C. Oubre, N. K. Grady, C. W. Hollars, S. M. Lane, T. R. Huser, P. Nordlander, and N. J. Halas, "Surface-Enhanced Raman Scattering from Individual Au Nanoparticles and Nanoparticle Dimer Substrates," *Nano Letters*, vol. 5, pp. 1569–1574, Aug. 2005.

[95] E. J. Blackie, E. C. Le Ru, and P. G. Etchegoin, "Single-Molecule Surface-Enhanced Raman Spectroscopy of Nonresonant Molecules," *Journal of the American Chemical Society*, vol. 131, pp. 14466–14472, Oct. 2009.

[96] X. Huang, S. Xiao, D. Ye, J. Huangfu, Z. Wang, L. Ran, and L. Zhou, "Fractal plasmonic metamaterials for subwavelength imaging," *Optics Express*, vol. 18, p. 10377, May 2010.

[97] T. Ishi, J. Fujikata, K. Makita, T. Baba, and K. Ohashi, "Si Nano-Photodiode with a Surface Plasmon Antenna," *Japanese Journal of Applied Physics*, vol. 44, pp. L364–L366, Mar. 2005.

[98] M. T. Wenzel, T. Härtling, P. Olk, S. C. Kehr, S. Grafström, S. Winnerl, M. Helm, and L. M. Eng, "Gold nanoparticle tips for optical field confinement in infrared scattering near-field optical microscopy," *Optics Express*, vol. 16, p. 12302, Aug. 2008.

[99] H. J. Simon, D. E. Mitchell, and J. G. Watson, "Optical Second-Harmonic Generation with Surface Plasmons in Silver Films," *Physical Review Letters*, vol. 33, pp. 1531–1534, Dec. 1974.

[100] B. C. Yildiz, M. E. Tasgin, M. K. Abak, S. Coskun, H. E. Unalan, and A. Bek, "Enhanced second harmonic generation from coupled asymmetric plasmonic metal nanostructures," *Journal of Optics (United Kingdom)*, vol. 17, no. 12, 2015.

[101] X. Y. Xiong, L. J. Jiang, W. E. Sha, and Y. H. Lo, "Enhanced second harmonic generation in a plasmonic particle-in-cavity nanoantenna," *2016 IEEE Antennas and Propagation Society International Symposium, APSURSI 2016 - Proceedings*, pp. 245–246, 2016.

[102] Y. Pu, R. Grange, C.-L. Hsieh, and D. Psaltis, "Enhanced Second Harmonic Generation in Plasmonic Nanocavities," in *Conference on Lasers and Electro-Optics 2010*, vol. 1, (Washington, D.C.), p. QFC5, OSA, 2010.

[103] S. Shen, L. Meng, Y. Zhang, J. Han, Z. Ma, S. Hu, Y. He, J. Li, B. Ren, T. M. Shih, Z. Wang, Z. Yang, and Z. Tian, "Plasmon-Enhanced Second-Harmonic Generation Nanorulers with Ultrahigh Sensitivities," *Nano Letters*, vol. 15, no. 10, pp. 6716–6721, 2015.

[104] A. U. Chowdhury, S. Zhang, and G. J. Simpson, "Powders Analysis by Second Harmonic Generation Microscopy," *Analytical Chemistry*, vol. 88, pp. 3853–3863, Apr. 2016.

[105] R. J. Tran, K. L. Sly, and J. C. Conboy, "Applications of Surface Second Harmonic Generation in Biological Sensing," *Annual Review of Analytical Chemistry*, vol. 10, pp. 387–414, June 2017.

[106] J. R. Gott, "Effect of molecular structure on optical second-harmonic generation from organic crystals," *Journal of Physics B: Atomic and Molecular Physics*, vol. 4, pp. 116–123, Jan. 1971.

[107] D. Wanapun, U. S. Kestur, D. J. Kissick, G. J. Simpson, and L. S. Taylor, "Selective Detection and Quantitation of Organic Molecule Crystallization by Second Harmonic Generation Microscopy," *Analytical Chemistry*, vol. 82, pp. 5425–5432, July 2010.

[108] C. Kai, C. Durak, J. R. Heflin, H. D. Robinson, Kai Chen, Cemil Durak, , J. R. Heflin, and H. D. Robinson*, "Plasmon-enhanced second-harmonic generation from ionic self-assembled multilayer films," *Nano Letters*, vol. 7, no. 2, pp. 254–258, 2007.

[109] Z. Wang, Z. Dong, H. Zhu, L. Jin, M.-H. Chiu, L.-J. Li, Q.-H. Xu, G. Eda, S. A. Maier, A. T. S. Wee, C.-W. Qiu, and J. K. W. Yang, "Selectively Plasmon-Enhanced Second-Harmonic Generation from Monolayer Tungsten Diselenide on Flexible Substrates," *ACS Nano*, vol. 12, pp. 1859–1867, Feb. 2018.

[110] L. Ghirardini, A. L. Baudrion, M. Monticelli, D. Petti, P. Biagioni, L. Duò, G. Pellegrini, P. M. Adam, M. Finazzi, and M. Celebrano, "Plasmon-Enhanced Second Harmonic Sensing," *Journal of Physical Chemistry C*, vol. 122, no. 21, pp. 11475–11481, 2018.

[111] S. Chen, F. Zeuner, M. Weismann, B. Reineke, G. Li, V. K. Valev, K. W. Cheah, N. C. Panoiu, T. Zentgraf, and S. Zhang, "Giant Nonlinear Optical Activity of Achiral Origin in Planar Metasurfaces with Quadratic and Cubic Nonlinearities," *Advanced Materials*, vol. 28, pp. 2992–2999, Apr. 2016.

[112] A. G. Mark, J. G. Gibbs, T.-C. Lee, and P. Fischer, "Hybrid nanocolloids with programmed three-dimensional shape and material composition," *Nature Materials*, vol. 12, pp. 802–807, June 2013.

[113] X. Shen, C. Song, J. Wang, D. Shi, Z. Wang, N. Liu, and B. Ding, "Rolling Up Gold Nanoparticle-Dressed DNA Origami into Three-Dimensional Plasmonic Chiral Nanostructures," *Journal of the American Chemical Society*, vol. 134, pp. 146–149, Jan. 2012.

[114] S. Knoppe, A. Dass, and T. Bürgi, "Strong non-linear effects in the chiroptical properties of the ligand-exchanged Au38 and Au40 clusters," *Nanoscale*, vol. 4, no. 14, p. 4211, 2012.

[115] S. Knoppe, I. Dolamic, A. Dass, and T. Bürgi, "Separation of Enantiomers and CD Spectra of Au40(SCH2CH2Ph)24: Spectroscopic Evidence for Intrinsic Chirality," *Angewandte Chemie International Edition*, vol. 51, pp. 7589–7591, July 2012.

[116] M. Farrag, "Enantioselective silver nanoclusters: Preparation, characterization and photoluminescence spectroscopy," *Materials Chemistry and Physics*, vol. 180, pp. 349–356, 2016.

[117] W. Ma, H. Kuang, L. Xu, L. Ding, C. Xu, L. Wang, and N. A. Kotov, "Attomolar DNA detection with chiral nanorod assemblies," *Nature Communications*, vol. 4, p. 2689, Oct. 2013.

[118] H. Zhang and A. O. Govorov, "Giant circular dichroism of a molecule in a region of strong plasmon resonances between two neighboring gold nanocrystals," *Physical Review B*, vol. 87, p. 075410, Feb. 2013.

[119] R.-Y. R. Y. Wang, P. Wang, Y. Liu, W. Zhao, D. Zhai, X. Hong, Y. Ji, X. Wu, F. Wang, D. Zhang, W. Zhang, R. Liu, and X. Zhang, "Experimental Observation of Giant Chiroptical Amplification of Small Chiral Molecules by Gold Nanosphere Clusters," *The Journal of Physical Chemistry C*, vol. 118, pp. 9690–9695, May 2014.

[120] M. C. di Gregorio, A. Ben Moshe, E. Tirosh, L. Galantini, and G. Markovich, "Chiroptical Study of Plasmon–Molecule Interaction: The Case of Interaction of Glutathione with Silver Nanocubes," *The Journal of Physical Chemistry C*, vol. 119, pp. 17111–17116, July 2015.

[121] B. M. Maoz, Y. Chaikin, A. B. Tesler, O. Bar Elli, Z. Fan, A. O. Govorov, and G. Markovich, "Amplification of chiroptical activity of chiral biomolecules by surface plasmons," *Nano Letters*, vol. 13, no. 3, pp. 1203–1209, 2013.

[122] E. Hendry, T. Carpy, J. Johnston, M. Popland, R. V. Mikhaylovskiy, a. J. Lapthorn, S. M. Kelly, L. D. Barron, N. Gadegaard, and M. Kadodwala, "Ultrasensitive detection and characterization of biomolecules using superchiral fields.," *Nature nanotechnology*, vol. 5, no. 11, pp. 783–787, 2010.

[123] M. Schäferling, D. Dregely, M. Hentschel, and H. Giessen, "Tailoring enhanced optical chirality: Design principles for chiral plasmonic nanostructures," *Physical Review X*, vol. 2, p. 031010, Aug. 2012.

[124] A. S. Karimullah, C. Jack, R. Tullius, V. M. Rotello, G. Cooke, N. Gadegaard, L. D. Barron, and M. Kadodwala, "Disposable Plasmonics: Plastic Templated Plasmonic Metamaterials with Tunable Chirality," *Advanced Materials*, vol. 27, pp. 5610–5616, Oct. 2015.

[125] R. Tullius, A. S. S. Karimullah, M. Rodier, B. Fitzpatrick, N. Gadegaard, L. D. D. Barron, V. M. M. Rotello, G. Cooke, A. Lapthorn, and M. Kadodwala, ""Superchiral" Spectroscopy: Detection of Protein Higher Order Hierarchical Structure with Chiral Plasmonic Nanostructures," *Journal of the American Chemical Society*, vol. 137, pp. 8380–8383, July 2015.

[126] M. Schäferling, X. Yin, and H. Giessen, "Formation of chiral fields in a symmetric environment," *Optics Express*, vol. 20, p. 26326, Nov. 2012.

[127] T. J. Davis and E. Hendry, "Superchiral electromagnetic fields created by surface plasmons in nonchiral metallic nanostructures," *Physical Review B*, vol. 87, p. 085405, Feb. 2013.

[128] V. K. Valev, J. J. Baumberg, B. De Clercq, N. Braz, X. Zheng, E. J. Osley, S. Vandendriessche, M. Hojeij, C. Blejean, J. Mertens, C. G. Biris, V. Volskiy, M. Ameloot, Y. Ekinci, G. a. E. Vandenbosch, P. a. Warburton, V. V. Moshchalkov, N. C. Panoiu, and T. Verbiest, "Nonlinear Superchiral Meta-Surfaces: Tuning Chirality and Disentangling Non-Reciprocity at the Nanoscale," *Advanced Materials*, vol. 26, pp. 4074–4081, June 2014.

[129] V. G. Veselago, "The Electrodynamics of Substances with Simultaneously Negative Values of ϵ and μ," *Soviet Physics Uspekhi*, vol. 10, pp. 509–514, Apr. 1968.

[130] J. B. Pendry, "Negative Refraction Makes a Perfect Lens," *Physical Review Letters*, vol. 85, pp. 3966–3969, Oct. 2000.

[131] P. Moitra, B. A. Slovick, W. Li, I. I. Kravchencko, D. P. Briggs, S. Krishnamurthy, and J. Valentine, "Large-Scale All-Dielectric Metamaterial Perfect Reflectors," *ACS Photonics*, vol. 2, pp. 692–698, June 2015.

[132] L. Cong, N. Xu, W. Zhang, and R. Singh, "Polarization Control in Terahertz Metasurfaces with the Lowest Order Rotational Symmetry," *Advanced Optical Materials*, vol. 3, no. 9, pp. 1176–1183, 2015.

[133] N. Meinzer, W. L. Barnes, and I. R. Hooper, "Plasmonic meta-atoms and metasurfaces," *Nature Photonics*, vol. 8, pp. 889–898, Nov. 2014.

[134] K. Yao and Y. Liu, "Plasmonic metamaterials," *Nanotechnology Reviews*, vol. 3, no. 2, pp. 177–210, 2014.

[135] X. Zheng, V. K. Valev, N. Verellen, Y. Jeyaram, A. V. Silhanek, V. Metlushko, M. Ameloot, G. A. E. Vandenbosch, and V. V. Moshchalkov, "Volumetric method of moments and conceptual multilevel building blocks for nanotopologies," *IEEE Photonics Journal*, vol. 4, no. 1, pp. 267–282, 2012.

[136] X. Zheng, N. Verellen, V. Volskiy, V. K. Valev, J. J. Baumberg, G. a. E. Vandenbosch, and V. V. Moshchalkov, "Interacting plasmonic nanostructures beyond the quasi-static limit: a "circuit" model," *Optics Express*, vol. 21, p. 31105, Dec. 2013.

[137] X. Zheng, N. Verellen, D. Vercruysse, V. Volskiy, P. Van Dorpe, G. A. E. Vandenbosch, and V. Moshchalkov, "On the Use of Group Theory in Understanding the Optical Response of a Nanoantenna," *IEEE Transactions on Antennas and Propagation*, vol. 63, pp. 1589–1602, Apr. 2015.

[138] O. Katzenelson, J. Edelstein, and D. Avnir, "Quantitative chirality of helicenes," *Tetrahedron Asymmetry*, 2000.

[139] M. Khorasaninejad, W. T. Chen, A. Y. Zhu, J. Oh, R. C. Devlin, D. Rousso, and F. Capasso, "Multispectral Chiral Imaging with a Metalens," *Nano Letters*, vol. 16, pp. 4595–4600, July 2016.

[140] S. Zu, Y. Bao, and Z. Fang, "Planar Plasmonic Chiral Nanostructures," *Nanoscale*, vol. 8, no. 7, pp. 3900–3905, 2016.

[141] V. K. Valev, N. Smisdom, A. V. Silhanek, B. De Clercq, W. Gillijns, M. Ameloot, V. V. Moshchalkov, and T. Verbiest, "Plasmonic Ratchet Wheels: Switching Circular Dichroism by Arranging Chiral Nanostructures," *Nano Letters*, vol. 9, pp. 3945–3948, Nov. 2009.

[142] X. Zheng, V. K. Valev, N. Verellen, V. Volskiy, and P. V. Dorpe, "Volumetric Method of Moments (V-MoM) in Modelling Nanotopologies : A Review," *Forum Electromag. Res. Methods Appl. Technol. (FERMAT)*, vol. 4, no. 4, pp. 1–21, 2014.

[143] W. Li, Z. J. Coppens, L. V. Besteiro, W. Wang, A. O. Govorov, and J. Valentine, "Circularly polarized light detection with hot electrons in chiral plasmonic metamaterials," *Nature Communications*, vol. 6, p. 8379, Sept. 2015.

[144] S. Lee, Z. Wang, C. Feng, J. Jiao, A. Khan, and L. Li, "Circular dichroism in planar extrinsic chirality metamaterial at oblique incident beam," *Optics Communications*, vol. 309, pp. 201–204, Nov. 2013.

[145] M. Decker, M. W. Klein, M. Wegener, and S. Linden, "Circular dichroism of planar chiral magnetic metamaterials," *Optics Letters*, vol. 32, no. 7, pp. 856–858, 2007.

[146] S. Droulias and V. Yannopapas, "Broad-Band Giant Circular Dichroism in Metamaterials of Twisted Chains of Metallic Nanoparticles," *The Journal of Physical Chemistry C*, vol. 117, pp. 1130–1135, Jan. 2013.

[147] E. Plum, V. a. Fedotov, and N. I. Zheludev, "Extrinsic electromagnetic chirality in metamaterials," *Journal of Optics A: Pure and Applied Optics*, vol. 11, p. 074009, July 2009.

[148] W. Kuhn, "The physical significance of optical rotatory power," *Transactions of the Faraday Society*, vol. 26, p. 293, 1930.

[149] Z. Fan and A. O. Govorov, "Plasmonic Circular Dichroism of Chiral Metal Nanoparticle Assemblies," *Nano Letters*, vol. 10, pp. 2580–2587, July 2010.

[150] B. Auguié, J. L. Alonso-Gómez, A. Guerrero-Martínez, and L. M. Liz-Marzán, "Fingers Crossed: Optical Activity of a Chiral Dimer of Plasmonic Nanorods," *The Journal of Physical Chemistry Letters*, vol. 2, pp. 846–851, Apr. 2011.

[151] M. Hentschel, V. E. Ferry, and A. P. Alivisatos, "Optical Rotation Reversal in the Optical Response of Chiral Plasmonic Nanosystems: The Role of Plasmon Hybridization," *ACS Photonics*, vol. 2, pp. 1253–1259, Sept. 2015.

[152] L. N. Aksyutov, "Temperature dependence of the optical constants of tungsten and gold," *Journal of Applied Spectroscopy*, vol. 26, pp. 656–660, May 1977.

[153] A. Papakostas, A. Potts, D. M. Bagnall, S. L. Prosvirnin, H. J. Coles, and N. I. Zheludev, "Optical Manifestations of Planar Chirality," *Physical Review Letters*, vol. 90, p. 107404, Mar. 2003.

[154] M. Kuwata-Gonokami, N. Saito, Y. Ino, M. Kauranen, K. Jefimovs, T. Vallius, J. Turunen, and Y. Svirko, "Giant optical activity in quasi-two-dimensional planar nanostructures," *Physical Review Letters*, vol. 95, pp. 1–4, Nov. 2005.

[155] E. Plum, V. A. Fedotov, A. S. Schwanecke, N. I. Zheludev, and Y. Chen, "Giant optical gyrotropy due to electromagnetic coupling," *Applied Physics Letters*, vol. 90, p. 223113, May 2007.

[156] J. K. Gansel, J. K. Gansel, M. Thiel, M. S. Rill, M. Decker, K. Bade, V. Saile, G. V. Freymann, S. Linden, M. Wegener, G. von Freymann, S. Linden, and M. Wegener, "Gold Helix Photonic Metamaterial as Broadband Circular Polarizer," *Science*, vol. 325, pp. 1513–1515, Sept. 2009.

[157] P. Fischer and F. Hache, "Nonlinear optical spectroscopy of chiral molecules," *Chirality*, vol. 17, no. 8, pp. 421–437, 2005.

[158] J. J. Maki and A. Persoons, "One-electron second-order optical activity of a helix," *The Journal of Chemical Physics*, vol. 104, no. 23, p. 9340, 1996.

[159] W. Kauzmann, *Quantum chemistry: An introduction*, vol. 70. New York: Academic Press, June 1957.

[160] R. Kolkowski, L. Petti, M. Rippa, C. Lafargue, and J. Zyss, "Octupolar Plasmonic Meta-Molecules for Nonlinear Chiral Watermarking at Subwavelength Scale," *ACS Photonics*, vol. 2, pp. 899–906, July 2015.

[161] X. Romain, F. Baida, and P. Boyer, "Spectrally tunable linear polarization rotation using stacked metallic metamaterials," *Journal of Optics*, vol. 19, pp. 1–17, Aug. 2017.

[162] M. Ren, E. Plum, J. Xu, and N. I. Zheludev, "Giant nonlinear optical activity in a plasmonic metamaterial," *Nature Communications*, vol. 3, p. 833, May 2012.

[163] E. Mamonov, T. Murzina, I. Kolmychek, A. Maydykovsky, V. Valev, A. Silhanek, T. Verbiest, V. Moshchalkov, and O. Aktsipetrov, "Chirality in nonlinear-optical response of planar G-shaped nanostructures," *Optics Express*, vol. 20, p. 8518, Apr. 2012.

[164] J. G. Gibbs, A. G. Mark, T.-C. Lee, S. Eslami, D. Schamel, and P. Fischer, "Nanohelices by shadow growth," *Nanoscale*, vol. 6, p. 9457, Apr. 2014.

[165] F. Hache, H. Mesnil, and M. C. Schanne-Klein, "Application of classical models of chirality to surface second harmonic generation," *Journal of Chemical Physics*, vol. 115, no. 14, pp. 6707–6715, 2001.

[166] R. Kuroda, T. Harada, and Y. Shindo, "A solid-state dedicated circular dichroism spectrophotometer: Development and application," *Review of Scientific Instruments*, vol. 72, no. 10, pp. 3802–3810, 2001.

[167] I. Tinoco, "Two-photon circular dichroism," *The Journal of Chemical Physics*, vol. 62, pp. 1006–1009, Feb. 1975.

[168] L. De Boni, C. Toro, and F. E. Hernández, "Synchronized double L-scan technique for the simultaneous measurement of polarization-dependent two-photon absorption in chiral molecules," *Optics Letters*, vol. 33, p. 2958, Dec. 2008.

[169] C. Toro, L. De Boni, N. Lin, F. Santoro, A. Rizzo, and F. E. Hernandez, "Two-Photon Absorption Circular Dichroism: A New Twist in Nonlinear Spectroscopy," *Chemistry - A European Journal*, vol. 16, pp. 3504–3509, Mar. 2010.

[170] K. Clays and A. Persoons, "Hyper-Rayleigh scattering in solution," *Physical Review Letters*, vol. 66, no. 23, pp. 2980–2983, 1991.

[171] K. Clays and A. Persoons, "Hyper-Rayleigh scattering in solution," *Review of Scientific Instruments*, vol. 63, pp. 3285–3289, June 1992.

[172] T. Verbiest, K. Clays, C. Samyn, J. Wolff, D. Reinhoudt, and A. Persoons, "Investigations of the Hyperpolarizability in Organic Molecules from Dipolar to Octopolar Systems," *Journal of the American Chemical Society*, vol. 116, pp. 9320–9323, Oct. 1994.

[173] G. K. Larsen, Y. He, J. Wang, and Y. Zhao, "Scalable fabrication of composite Ti/Ag Plasmonic helices: Controlling morphology and optical activity by tailoring material properties," *Advanced Optical Materials*, vol. 2, no. 3, pp. 245–249, 2014.

[174] D. M. Brunette, P. Tengvall, M. Textor, and P. Thomsen, *Titanium in Medicine*. Engineering Materials, Berlin, Heidelberg: Springer Berlin Heidelberg, 2001.

[175] P. B. Johnson and R. W. Christy, "Optical constants of the noble metals," *Physical Review B*, vol. 6, no. 12, pp. 4370–4379, 1972.

[176] E. C. Hao, G. C. Schatz, R. C. Johnson, and J. T. Hupp, "Hyper-Rayleigh scattering from silver nanoparticles," *Journal of Chemical Physics*, vol. 117, pp. 5963–5966, Oct. 2002.

Appendix A

Reducing $\chi^{(2)}$ with Symmetry

A.1 4-fold Rotational Symmetry

For a rotation of $\theta = \frac{\pi}{2}$, the transformation matrix is given by

$$R(\theta = \frac{\pi}{2})_{i,j} = \begin{bmatrix} 0 & -1 & 0 \\ 1 & 0 & 0 \\ 0 & 0 & 1 \end{bmatrix} \tag{A.1}$$

We apply the rotation to χ_{ijk} given in equation 3.15, as in equation 3.25, giving

$$\chi'_{ijk} = \begin{bmatrix} -\chi_{yyy} & -\chi_{yxx} & -\chi_{yzz} & -\chi_{yxz} & -\chi_{yzx} & \chi_{yzy} & \chi_{yyz} & \chi_{yyx} & \chi_{yxy} \\ \chi_{xyy} & \chi_{xxx} & \chi_{xzz} & \chi_{xxz} & \chi_{xzx} & -\chi_{xzy} & -\chi_{xyz} & -\chi_{xyx} & -\chi_{xxy} \\ \chi_{zyy} & \chi_{zxx} & \chi_{zzz} & \chi_{zxz} & \chi_{zzx} & -\chi_{zzy} & -\chi_{zyz} & -\chi_{zyx} & -\chi_{zxy} \end{bmatrix} \tag{A.2}$$

By enforcing the symmetry $\chi'_{ijk} = \chi_{ijk}$, we find that 7 independent components remain, leaving

$$\chi^{(2)}_{ijk} = \begin{bmatrix} 0 & 0 & 0 & \chi_{xyz} & \chi_{xzy} & \chi_{xzx} & \chi_{xxz} & 0 & 0 \\ 0 & 0 & 0 & \chi_{yyz} & \chi_{yzy} & \chi_{yzx} & \chi_{yxz} & 0 & 0 \\ \chi_{zxx} & \chi_{zyy} & \chi_{zzz} & 0 & 0 & 0 & 0 & \chi_{zxy} & \chi_{zyx} \end{bmatrix} \tag{A.3}$$

with dependencies given by

$$\begin{aligned} &\chi_{xyz} = -\chi_{yxz}, \chi_{xzy} = -\chi_{yzx}, \chi_{xzx} = \chi_{yzy} \\ &\chi_{xxz} = \chi_{yyz}, \chi_{zxx} = \chi_{zyy}, \chi_{zxy} = -\chi_{zyx} \\ &\chi_{zzz} \end{aligned} \tag{A.4}$$

Applying permutation symmetry leaves the reduced tensor as

$$d_{il} = \begin{pmatrix} 0 & 0 & 0 & \chi_{xyz} & \chi_{xzx} & 0 \\ 0 & 0 & 0 & \chi_{yzy} & \chi_{yzx} & 0 \\ \chi_{zxx} & \chi_{zyy} & \chi_{zzz} & 0 & 0 & 0 \end{pmatrix} \tag{A.5}$$

with dependencies $\chi_{xyz} = -\chi_{yzx}$, $\chi_{yzy} = \chi_{xzx}$, and $\chi_{zxx} = \chi_{zyy}$.

A.2 2-fold Rotational Symmetry

In the case of 2-fold rotational symmetry around the z axis, the appropriate rotation matrix is given by equation 3.24 as

$$R(\theta = \pi)_{i,j} = \begin{bmatrix} -1 & 0 & 0 \\ 0 & -1 & 0 \\ 0 & 0 & 1 \end{bmatrix} \tag{A.6}$$

This corresponds to the coordinate substitution $x \to -x$, $y \to -y$, $z \to z$. Again, applying rotation to χ_{ijk} and enforcing the symmetry $\chi'_{ijk} = \chi_{ijk}$ leaves the reduced tensor

$$\chi^{(2)}_{ijk} = \begin{bmatrix} 0 & 0 & 0 & \chi_{xyz} & \chi_{xzy} & \chi_{xzx} & \chi_{xxz} & 0 & 0 \\ 0 & 0 & 0 & \chi_{yyz} & \chi_{yzy} & \chi_{yzx} & \chi_{yxz} & 0 & 0 \\ \chi_{zxx} & \chi_{zyy} & \chi_{zzz} & 0 & 0 & 0 & 0 & \chi_{zxy} & \chi_{zyx} \end{bmatrix} \tag{A.7}$$

with all remaining components left independent [56].

A.3 3-fold Rotational Symmetry

The case of 3-fold rotational symmetry is more complex, since for a rotation of $\theta = \frac{2}{3}\pi$ radians the rotation matrix is given by

$$R(\theta = \frac{2}{3}\pi)_{i,j} = \begin{bmatrix} -\frac{1}{2} & -\frac{\sqrt{3}}{2} & 0 \\ \frac{\sqrt{3}}{2} & -\frac{1}{2} & 0 \\ 0 & 0 & 1 \end{bmatrix} \tag{A.8}$$

As before, we can rotate χ_{ijk} and equate to the initial tensor, giving

$$\chi'_{ijk} = R(\theta_z)_{i\alpha} R(\theta_z)_{j\beta} R(\theta_z)_{k\gamma} \chi^{(2)}_{\alpha\beta\gamma} = \chi_{ijk} \tag{A.9}$$

This leaves the reduced tensor as

$$\chi^{(2)}_{ijk} = \begin{bmatrix} \chi_{xxx} & \chi_{xyy} & 0 & \chi_{xyz} & \chi_{xzy} & \chi_{xzx} & \chi_{xxz} & \chi_{xxy} & \chi_{xyx} \\ \chi_{yxx} & \chi_{yyy} & 0 & \chi_{yyz} & \chi_{yzy} & \chi_{yzx} & \chi_{yxz} & \chi_{yxy} & \chi_{yyx} \\ \chi_{zxx} & \chi_{zyy} & \chi_{zzz} & 0 & 0 & 0 & 0 & \chi_{zxy} & \chi_{zyx} \end{bmatrix} \tag{A.10}$$

with the dependencies

$$\begin{aligned} &\chi_{xxx} = -\chi_{xyy} = -\chi_{yyz} = -\chi_{yxy} \\ &\chi_{xyz} = -\chi_{yxz}, \chi_{xzy} = -\chi_{yzx} \\ &\chi_{xzx} = \chi_{yzy}, \chi_{xxz} = \chi_{yyz} \\ &\chi_{yyy} = -\chi_{yxx} = -\chi_{xxy} = -\chi_{xyx} \\ &\chi_{zxx} = \chi_{zyy}, \chi_{zxy} = -\chi_{zyx} \\ &\chi_{zzz} \end{aligned} \tag{A.11}$$

Under permutation symmetry, this reduces to

$$d_{il} = \begin{pmatrix} \chi_{xxx} & \chi_{xyy} & 0 & \chi_{xyz} & \chi_{xzx} & \chi_{xyx} \\ \chi_{yxx} & \chi_{yyy} & 0 & \chi_{yzy} & \chi_{yzx} & \chi_{yxy} \\ \chi_{zxx} & \chi_{zyy} & \chi_{zzz} & 0 & 0 & 0 \end{pmatrix} \tag{A.12}$$

Appendix B

Equipment Details

B.1 Laser Specifications

The laser system used in sections 6 and 7 is a commercial Spectra-Physics Mai-Tai HP Ti:Sapphire pulsed laser. At 800 nm wavelength, the laser operates at a repetition rate $f_p = 80\,\text{MHz}$ with a full width half maximum pulse duration of $t_p = 100\,\text{fs}$. A maximum average power $P_{max} = 2.9\,\text{W}$ is obtainable at this wavelength, giving a peak pulse power:

$$P_{peak} = \frac{P_{max}}{t_p f_p} = 362.5\,\text{kW} \tag{B.1}$$

In practice, operating at maximum power would almost always result in severe sample damage, due to continuous heating effects. However, for our nonlinear optics experiments, high peak pulse power is desirable, as the nonlinear emission is strongly dependent on the electric field intensity (section 3). Ideally, the average power should be reduced significantly, while still allowing for high peak pulse power. This is realised with the use of an optical chopper wheel, operating with a duty cycle $D = 1.7\%$. This provides a "cool-down" period, without altering the laser peak pulse power. The maximum average power after the chopper is thus given by

$$P_{avg} = P_{peak} f_p D t_p = 49\,\text{mW} \tag{B.2}$$

In our experiments, a pair of linear polarisers are placed *before* the optical chopper to allow for free control over the peak pulse power in addition to the fixed reduction in average power from the chopper. The laser powers stated in sections 6 and 7 are the average power following both of these reductions. Since the optical chopper operates with a fixed duty cycle, the peak power is obtained from the measured average power incident on the sample following:

$$P_{peak} = \frac{P_{avg}}{0.017(t_p f_p)} \tag{B.3}$$

Appendix C

Additional Data: Chiral Crosses

C.1 Calculating chiral geometric difference

To quantify a simple measure of the geometric chirality of a structure, we use the maximum possible overlap of a pair of mirrored structures. An achiral structure can completely overlap with its mirror image after undergoing only rotation and translation. Therefore, a structure with high "chiral geometric difference" will have a low maximum overlapping area (or volume) with its mirror image under only rotation and translation. Here, we define our chiral geometric difference as $1 - (2A_{Overlap})/A_{Total}$, where $A_{Overlap}$ is the area of maximal overlap that can be achieved between left- and right-handed shapes, and A_{Total} is the total area of both shapes. As can be seen in Figure 5.1b (in the main text), we use the negative of this value for the chiral geometric difference of the opposite enantiomer. Since the overlap cannot be negative, this is done solely for comparison to experimental data.

We calculate $A_{Overlap}$ by rotating and translating the two mirror-image shapes relative to each other, and optimising these parameters to maximise the overlapping area. Examples of this overlap are given in Figure C.1.

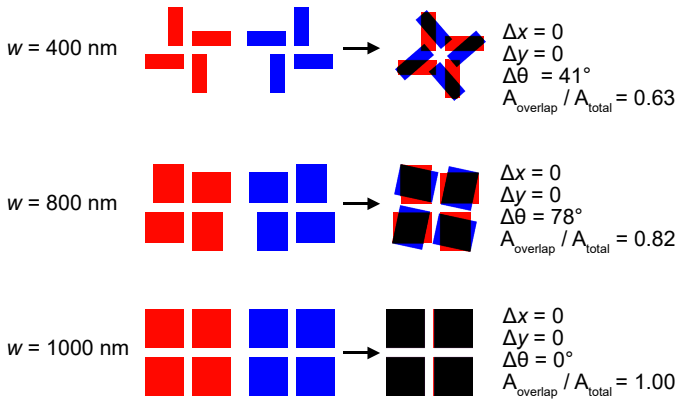

Figure C.1: *Examples of the overlap used to define our chiral geometric difference. Red and blue show the right- and left- handed crosses respectively. A_{Total} is the sum of the red and blue areas. $A_{Overlap}$ is the maximum overlapping area, shown in black. Δx, Δy and $\Delta\theta$ give the parameters for translation (x, y) and rotation respectively, obtained by maximising $A_{Overlap}$. In the achiral case ($w = 1000\,\mathrm{nm}$), complete overlap is possible because the structure is achiral.*

C.2 Scattering Spectra

For additional characterisation of the chiral cross samples (section 5), linear scattering spectra were both simulated and experimentally obtained. In simulations, no significant circular dichroism was observed. In the experimental data, no circular dichroism could be observed above experimental noise.

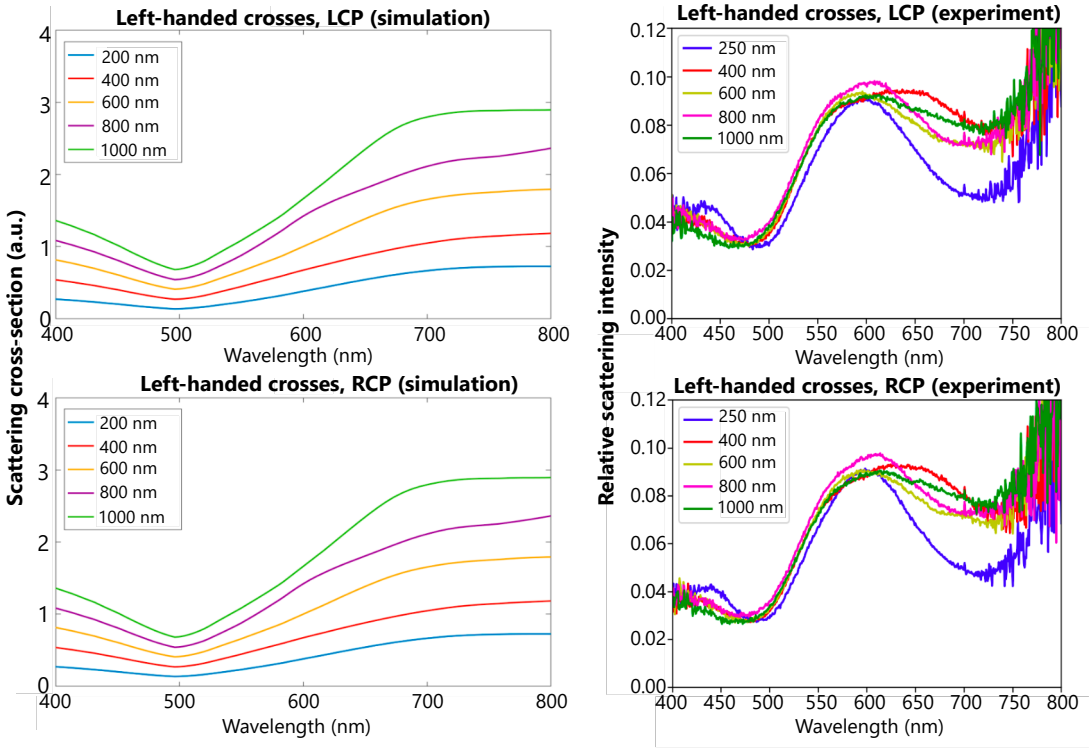

Figure C.2: *(Left) Numerically-obtained linear scattering cross sections for left-handed chiral cross structures under LCP (top) and RCP (bottom) illumination, with varying arm width (legend). (Right) Experimentally obtained linear scattering spectra for the same structures.*

Appendix D

Additional Data: Au Nanohelices

D.1 SHG-OR

D.1.1 74 nm separated helices

Figures D.1 and D.2 were obtained following the same procedures described in section 6. The structures here were designed to be identical to those in section 6, but with a larger centre-to-centre inclusion separation of 74 nm. All geometric parameters are given in the figures.

Notably, neither the data for p-polarised or s-polarised illumination closely match the data shown in section 6. This strongly suggests that the effective susceptibility tensor component values of the metamaterial are strongly dependent on the inclusion separation, even for only slightly different separations well below the operating wavelength. Optical rotation is still observed in both cases, however neither figures D.1 nor D.2 show rotation solely attributable to chirality, or clearly dominated by anisotropy.

D.1.2 1.5× scaled helices

Figures D.3 and D.4 were obtained following the same procedures described in section 6. The structures here are designed to be $\approx 1.5\times$ scaled copies of those in section 6. In practice, this is difficult to achieve. Notably, the wire thickness is the same as in section 6, and while the height is indeed 1.5× scaled, the helical pitch and inclusion separation are closer to 1.3×. Nevertheless, this data demonstrates the effect of changing the geometry of the nanohelix structures themselves. All geometric parameters are given in the figures.

Interestingly, figure D.4 shows behaviour qualitatively very similar to that in figure 6.3. These larger helices exhibit the same anisotropy-dominated optical rotation for p-polarised incident light, however the behaviour under s-polarised illumination is dramatically different to section 6. The similarity in behaviour under p-polarised illumination suggests that the effective susceptibility tensor values are less sensitive to changes in the individual inclusion dimensions than the arrangement and separation of the inclusions.

In both figures D.1 and D.3, the rotation of s-polarised incident light cannot be solely attributed to the structural chirality, due to both strong angular variations, and a lack of inversion between enantiomorphs. This demonstrates the "Goldilocks" nature of the

effect observed in section 6, whereby the interaction of particular susceptibility tensor component values allows the direct measurement of intrinsic structural chirality, under particular experimental conditions.

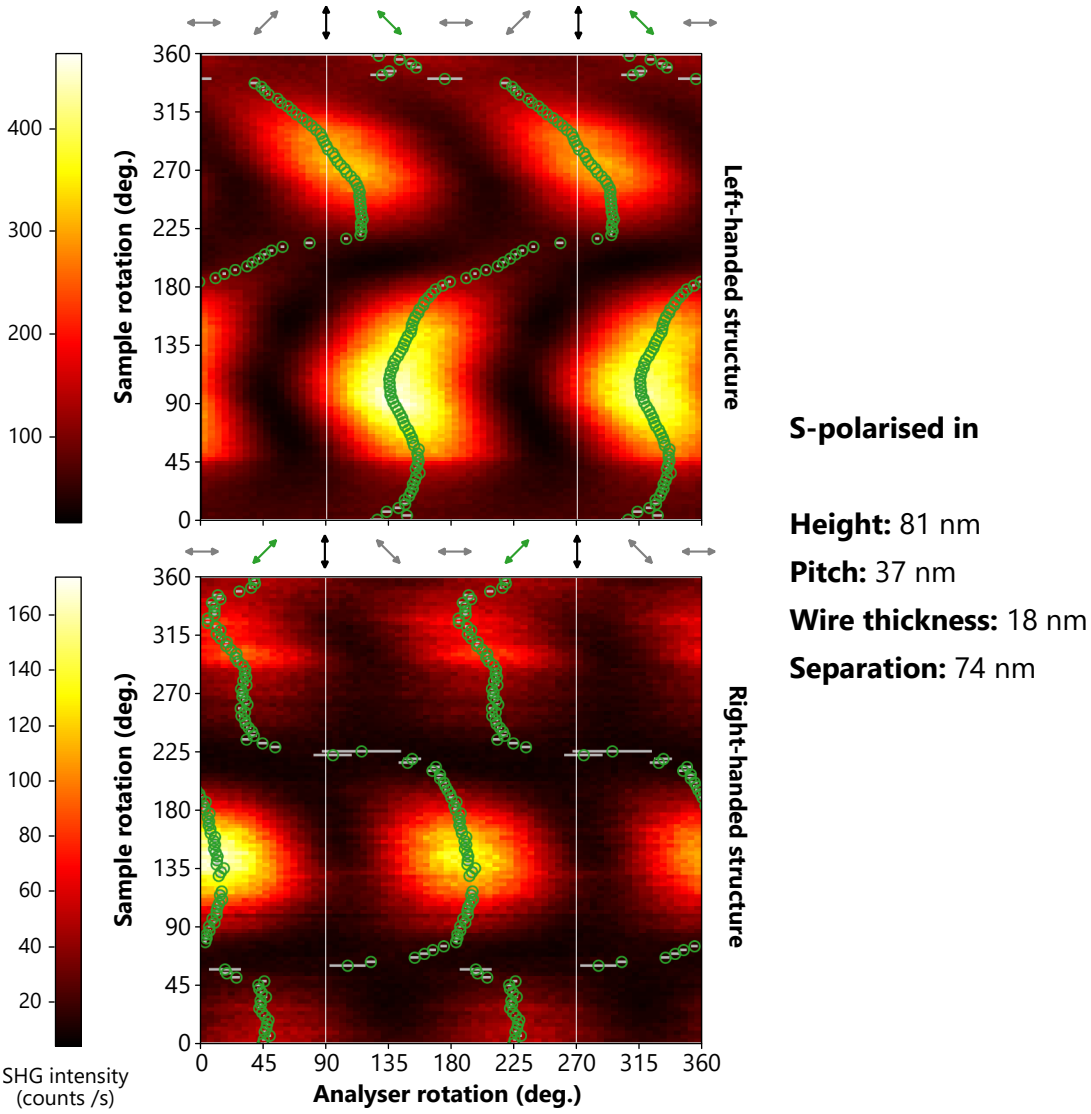

Figure D.1: *SHG optical rotation heatmaps for helical metamaterial, with* 74 nm *inclusion separation, for S-polarised incident light.*

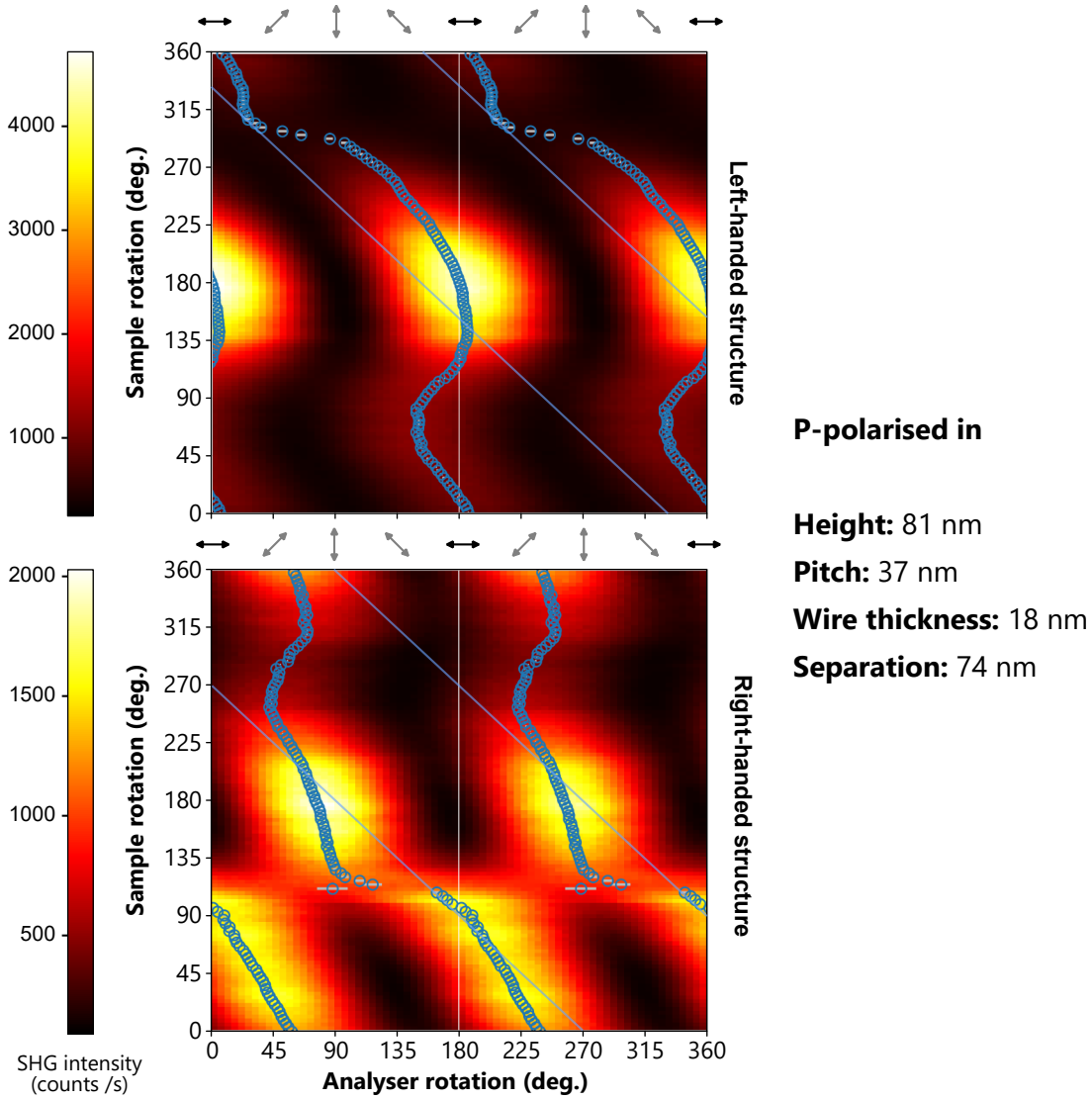

Figure D.2: *SHG optical rotation heatmaps for helical metamaterial, with* 74 nm *inclusion separation, for P-polarised incident light.*

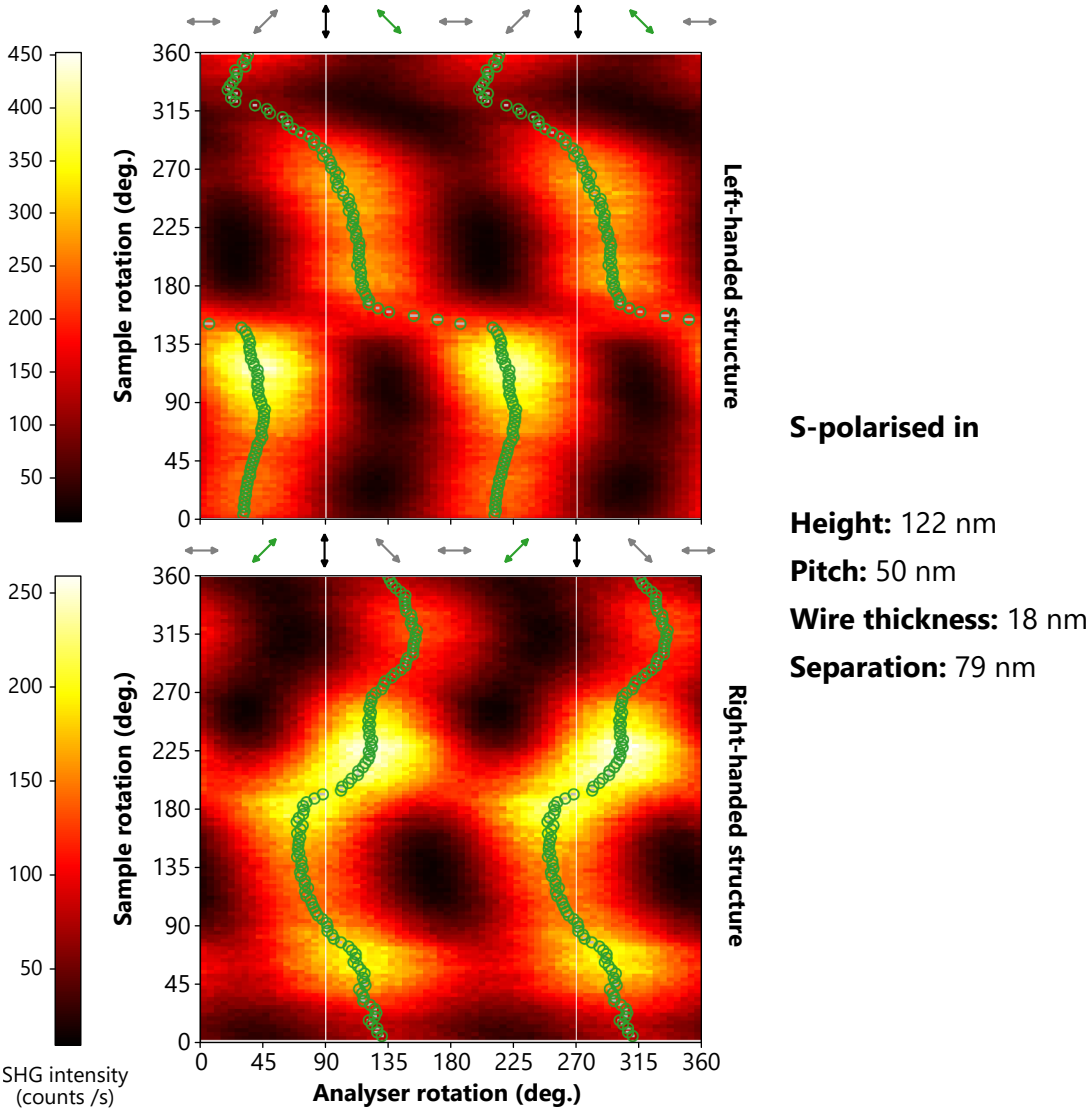

Figure D.3: *SHG optical rotation heatmaps for helical metamaterial, with* 122 nm *height,* 50 nm *pitch,* 18 nm *wire thickness, and* 79 nm *inclusion separation, for S-polarised incident light.*

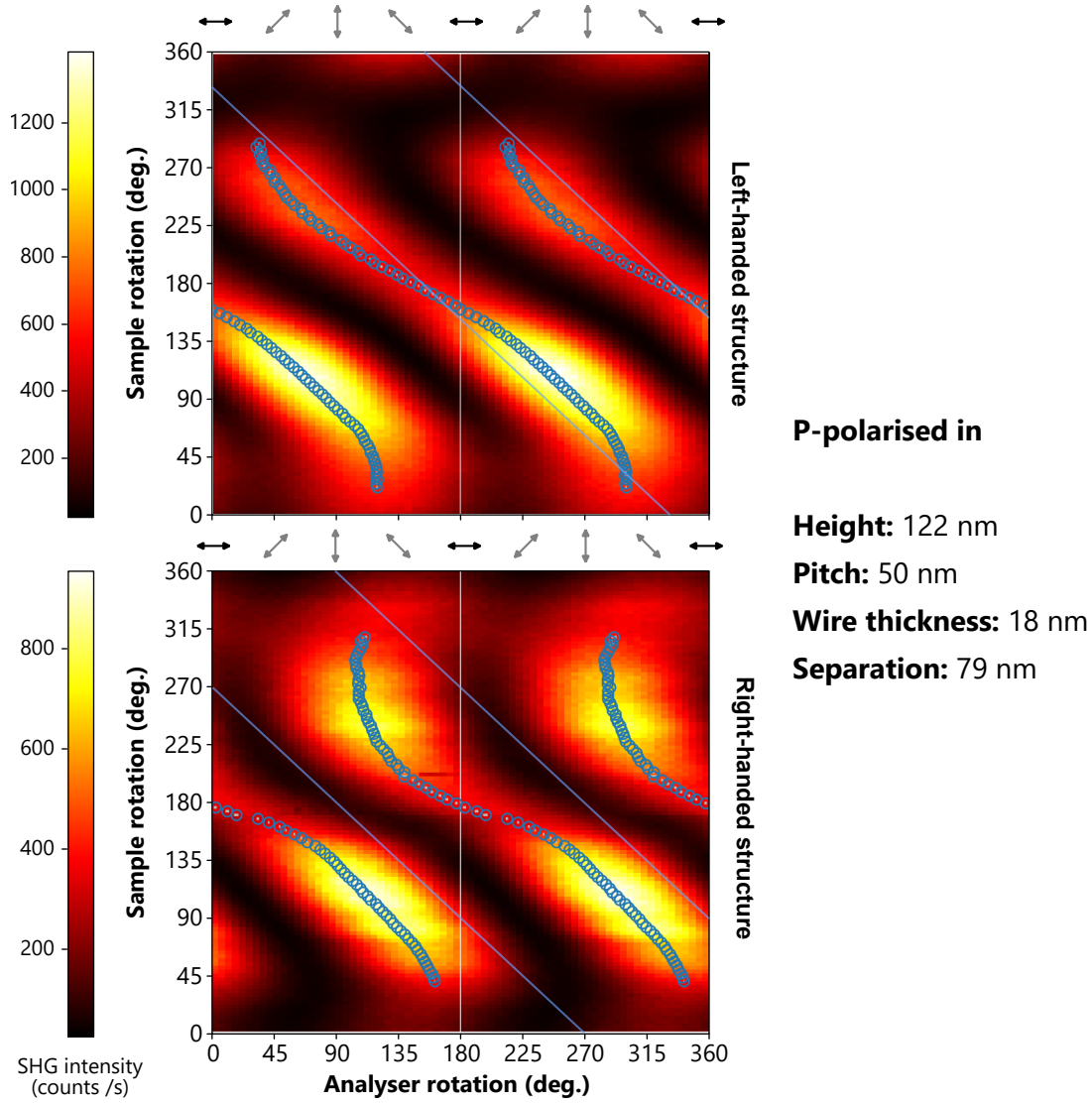

Figure D.4: *SHG optical rotation heatmaps for helical metamaterial, with* 122 nm *height,* 50 nm *pitch,* 18 nm *wire thickness, and* 79 nm *inclusion separation, for P-polarised incident light.*

Appendix E

Automated Data Acquisition and Analysis

Significant time during this project has been spent developing Python libraries to automate the acquisition and analysis of data taken from a range of experimental setups. This section briefly discusses the purpose of the most significant libraries developed, and where to find the publicly available source code.

E.1 Automated Data Acquisition

Diffraction CID experiments undertaken by C. Kuppe (reference [5]) made use of automated lab hardware from a range of manufacturers, each using their own software platforms for automation. Moreover, we found early on that errors in one piece of hardware could result in difficult to recover errors in other parts of the experimental setup. With this in mind, I developed a Python library to alleviate these two main issues.

The library defined a common class for all lab hardware, requiring certain functions like standard and emergency shutdown procedures. When opening communication with a device, the system attaches that device to an object responsible for tracking the status of all active devices. Communication cannot be opened to a device without this. In the event of a repeated, irrecoverable exception in communication, all devices are automatically shut down in the safest way possible. Additionally, when the experiment is finished, communication with all devices is automatically safely closed, without any required user input. All behaviour can, however, be overridden by the lab user if needed. Parts of this library were used in the acquisition of chiroptical microscopy measurements from section 6, and may be used in SHG measurements in the future.

The developed code was recently merged into a fork of the "LabDo" module, by J. Stirling. The fork can be found at `https://gitlab.com/jtc42/LabDo`. The specific implementation of this library used by C. Kuppe in all diffraction CID measurements can be found at `https://gitlab.com/jtc42/LabDo-CD-Spectrometer`.

E.2 Automated Data Analysis

Due to the large number of degrees of freedom during SHG chiroptical measurements, as found in references [4, 8], any individual heatmap required the processing and analysis of many thousands of data points. For this reason, another Python 3 library was developed to automate this analysis as much as reasonably possible. By using metadata embedded by LabView acquisition code developed by D. C. Hooper, all previously unsorted and unfiltered data can be pulled into the library, and plots for common types of experiment can be automatically generated. This included heatmaps for SHG-CID measurements, as well as SHG optical rotation heatmaps (and curve fitting data) such as those in section 6. The developed code can be found at `https://gitlab.com/jtc42/mpnp-shg-analysis`.